Copyright

by

Dharmaraj Indurthy

2006

Secondary Beam Monitors for the NuMI Facility at FNAL

by

Dharmaraj Indurthy, B.S.

Thesis

Presented to the Faculty of the Graduate School of

The University of Texas at Austin

in Partial Fulfillment

of the Requirements

for the Degree of

Master of Science in Applied Physics

The University of Texas at Austin

August 2006

Secondary Beam Monitors for the NuMI Facility at FNAL

Approved by
Supervising Committee:

_____

_____

To my parents and my supervisor, whose patient support has made all the difference.

Secondary Beam Monitors for the NuMI Facility at FNAL

Dharmaraj Indurthy, MSApplPhy
The University of Texas at Austin, 2006

Supervisor: Sacha Kopp

The Neutrinos at the Main Injector (NuMI) beam principally supplies high energy neutrinos to the Main Injector Neutrino Oscillation Search (MINOS) experiment, which is investigating neutrino oscillations. The NuMI beamline accepts 120 GeV protons from the Fermilab Main Injector and steers them toward a graphite target to produce a secondary meson beam that decays to neutrinos and muons. Due to the constraints placed on beam quality, ionization chamber arrays are developed to measure the primary beam and tertiary charged particles to monitor beam quality, beam direction, and the operational integrity of the upstream beamline components. This thesis describes the research and development of these beam monitors and their demonstrated utility for MINOS and NuMI.

Contents

Abstract **v**

Chapter 1 Introduction to Beam Monitoring **1**

1.1 The NuMI Beamline 1

1.1.1 Primary Beam Instrumentation 4

1.1.2 The NuMI Target & Horns 5

1.2 NuMI Beam Monitoring System 11

1.2.1 Hadron Monitor 14

1.2.2 Muon Monitors 15

1.3 Ionization chambers 16

1.3.1 Physics of Ionization Chambers 16

1.3.2 Chamber Construction 19

1.3.3 Cleaning 24

1.3.4 The Hadron Monitor 25

1.3.5 The Muon Monitors 30

1.4 Chamber Numbering Conventions 34

Chapter 2 Beam Monitor Installation **37**

2.1 Hadron Monitor Installation 37

2.1.1 Design Drawings 38

2.1.2 As-Installed Drawings 39
2.2 Muon Monitor Installation 49
2.3 Gas System 53

Chapter 3 Calibration of the Secondary Beam Monitors 56
3.1 Introduction 56
3.2 Calibration 57
3.2.1 Source 58
3.2.2 Electronics 60
3.2.3 Gas System 63
3.3 Calibration Test Stands 68
3.3.1 Hadron Monitor 68
3.3.2 Muon Monitor 80
3.4 Calibration Analysis 80
3.4.1 Hadron Monitor 80
3.4.2 Muon Monitor 83

Chapter 4 Neutron Studies 97
4.1 Introduction 97
4.2 Experimental Setup 98
4.2.1 Ionization Chambers 98
4.2.2 Gas System 100
4.2.3 Electronics and Data Aquisition 102
4.3 Neutron Source 103
4.4 Neutron Source Placement and Flux Estimation 104
4.5 Expected Rates 107
4.5.1 Neutron Interactions 107

4.5.2 Properties of the Recoil 108
4.5.3 Ionization by Recoils 111
4.5.4 Gamma Rate 111
4.6 Plateau Measurements 115
4.6.1 Helium Results 116
4.6.2 Argon Results 119
4.7 Conclusions 130

Chapter 5 In-Beam Performance **131**
5.1 Introduction 131
5.2 Chamber Performance 134
5.3 Signal Response to Environmental changes 139
5.4 Long Term Beam Stability 139
5.5 Target Failure And Recovery 151

Bibliography **164**

Vita **169**

Chapter 1

Introduction to Beam Monitoring

1.1 The NuMI Beamline

The Neutrinos at the Main Injector (NuMI) facility [1] is an accelerator-based neutrino beam of 2-20GeV muon-neutrinos currently used for the MINOS experiment [2]. Additional experiments are foreseen [3, 4] Fig. 1.1 describes the NuMI beamline in the context of MINOS. The neutrino beam is produced from the interactions of a 120 GeV/c proton beam supplied by the Main Injector (MI) on a 1m long graphite target. The resulting neutrino beam proceeds toward the near detector 1000m downstream and the far detector 735km away at the Soudan Undergound Laboratory in Soudan, MN.

Fig. 1.2 shows the salient components of the NuMI beamline in detail. After the proton beam is extracted from the Main Injector, the proton beam is steered 360m to the NuMI target. The subsequent mesons, mostly pions (π^+, π^-) and kaons (K^+,K^-,K^0), are focused by two magnets (horns), and

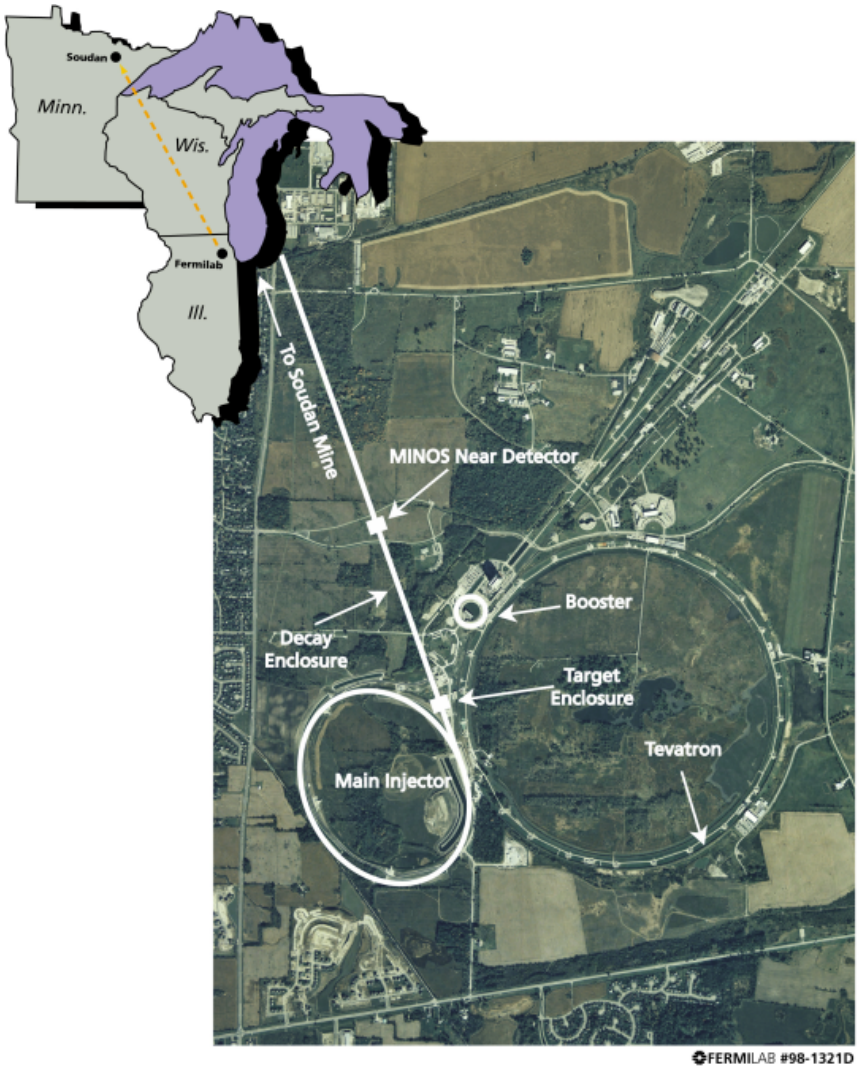

Figure 1.1: Overview of the MINOS experiment. Protons from the main injector are strike the NuMI target to produce a neutrino beam that is sent to the MINOS near-detector and directed toward the Soudan Mine in Soudan, MN.

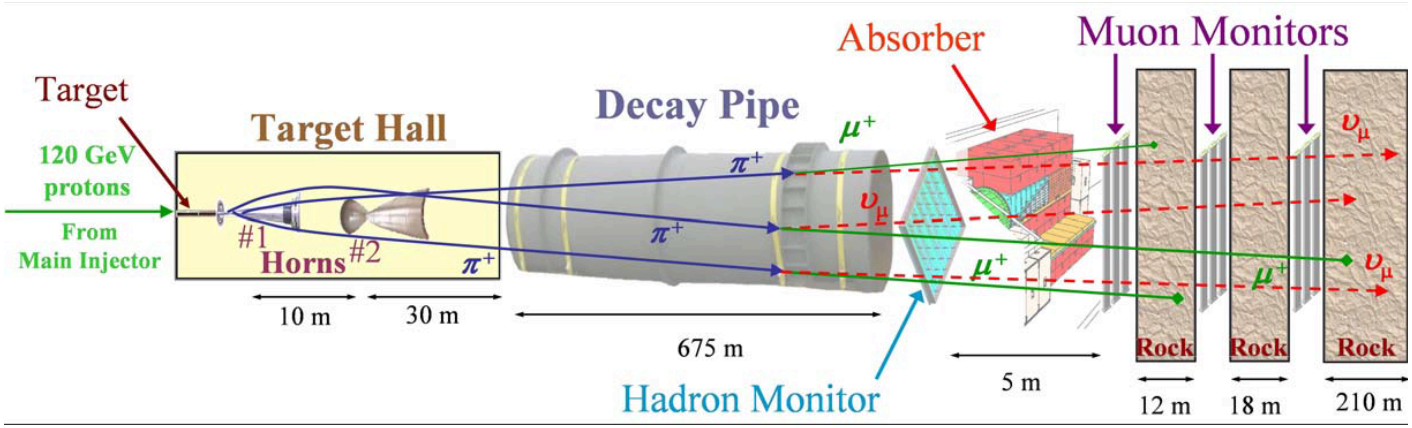

Figure 1.2: Overview of the NuMI beamline. Protons are steered from the MI to the NuMI target via magnets in the NuMI primary beamline. The resulting mesons are focused by two horns. The hadron monitor measures the remnant hadrons. The muon monitors measure the muon beam. The neutrino beam proceeds toward the MINOS detectors.

this secondary beam is directed toward a 675m long evacuated decay pipe.

In the ensuing decay region, the mesons in the secondary beam decay to muon and ν_μ pairs to produce the neutrino beam. The hadron monitor sits between the end of the decay pipe and a beam dump called the absorber. It measures the intensity and direction of the remnant hadron beam. The absorber consists of an aluminum-steel core surrounded by a layer of steel blocks and an outer layer of concrete blocks. It absorbs the energy of the hadrons in the beam, and permits the muons and neutrinos to proceed.

The tertiary beam proceeds through another 220m of dolomite rock. Three muon detectors are installed in three locations, one immediately upstream of the rock and the other two in excavated alcoves 10m and 30m downstream. The alcoves provide information on the charged components of the tertiary beam. Because the muons and neutrinos come from the same decay, understanding the muon beam provides information about neutrino beam quality.

The MINOS near detector sits 300m downstream of the end of the decay pipe. It is a 940 Ton detector that measures neutrino interactions through its iron and scintillator planes. The beam eventually reaches the far detector in Soudan. This detector is similar in construction to the near detector, albeit 5.4 kTon in mass. It measures the neutrino beam for comparison with the near detector results. Oscillations are evidenced by the energy dependent disappearance of neutrinos [5].

1.1.1 Primary Beam Instrumentation

The primary beamline uses dipole and quadrupole magnets to guide the proton beam toward the target. Trim magnets along the transfer line can be used to

adjust the beam position locally or to translate the beam accross the target.

Two beam current toroids are installed in the transfer line, one immediately after extraction, and one upstream of the target. The toroids transform the pickup currents induced by the beam to provide an accurate measure of beam intensity.

The Beam Position Monitors (BPMs) are devices that measure transverse beam position. Two electrodes act as capacitive pickups. The difference in the induced charge of each pickup divided by the sum provides a measure of the beam position. The BPMs can be oriented either horizontally or vertically. They also provide a measure of beam intensity which is simply the sum of the induced charge on the electrodes [7]. Thirteen horizontal BPMs and 11 vertical BPMs are installed in the NuMI beamline.

Ten Profile Monitors (PMs) are installed in the NuMI beamline. Each PM provides a horizontal and vertical beam position and beam width. Two sets of titanium foils are segmented into thin strips with .5mm or 1mm spacings. The foils are mounted orthogonally, one horizontal, one vertical, and provide spatial profiles via signals from the secondary emission of electrons. By summing the strip signals, one can also measure beam intensity [8].

1.1.2 The NuMI Target & Horns

The NuMI target is a composed of 47 20mm long graphite segments machined into fins of cross-sectional dimensions 6.4mm $\times$ 21.4mm. A diagram is shown in Fig 1.3. In series, the fins and cooling lines form a narrow snout that extends from the target canister. The target canister section houses feedthroughs for cooling water lines, gas, pumps, and other instrumentation.

An airtight aluminum casing houses the target. Beryllium windows are

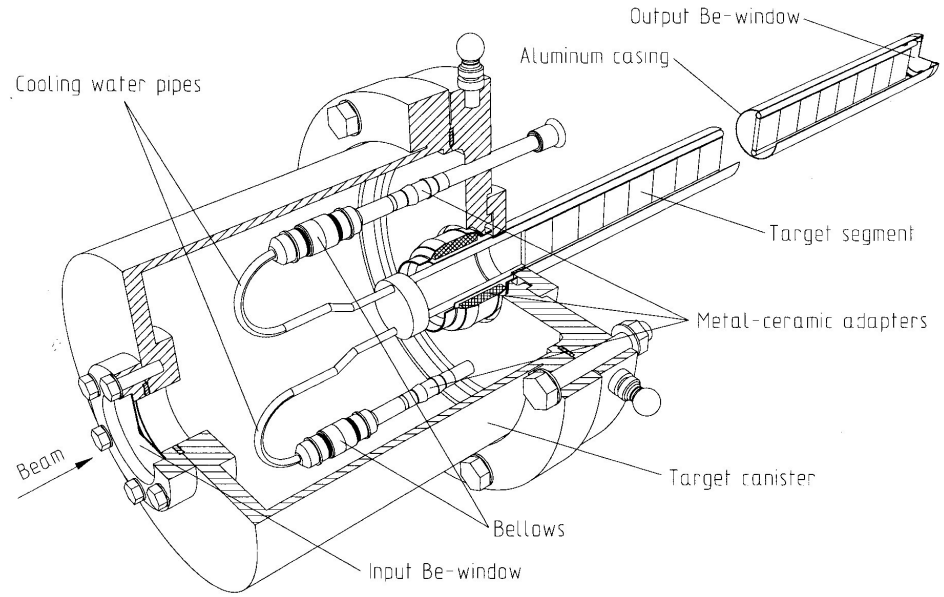

Figure 1.3: Diagram of the NuMI target. The beam passes through a total of 47 graphite fins, each 20 mm along the beam direction and transversely 6.4×15 mm^2 in size. The fins are supported on stainless steel tubes which also serve for water-cooling. The entire structure is housed in a stainless steel vessel which can be evacuated or filled with Helium gas.

mounted at the upstream and downstream ends of the casing for the proton beam entrance and exit. The fins and the cooling tubes are separated from the the target casing by ceramic spacers to electrically isolate the target material.

During running, the target cannister is filled with pressurized helium. This allows for heat transfer from the aluminum casing to the cooling lines, and it suppresses a known water leak in the cooling lines.

The 1m length of the target corresponds to 2.05 interaction lengths. The high intensities of beam merit the temperature-resilient graphite construction. Its low energy deposition and strength has been shown to be sufficient to

survive the stresses of high intensity beam heating [9].

A 1.5m long graphite baffle collimater, shown in Figure 1.4 is located 68 cm upstream of the target. Its function is to prevent stray beam from damaging the components in the target cannister or the horns. Its 11mm diameter aperture has been shown to protect the horns for for all energy beams. It is mounted together with the target on the positioning module, so their relative positions are fixed [11].

NuMI has two horns that focus the secondary pion beam and significantly increase the flux of neutrinos at the detectors. These horns are transmission-line magnets that produce toroidal magnetic fields. Diagrams are shown in Figure 1.5. Current travels along the contoured shape of the aluminum inner conductor (closest to beam axis), and returns along the outer conductor. A no-field region exists between the inner conductor and the horn axis. The field strength falls off inversely with radius. The inner conductor is parabolically shaped, so that the length of field region seen by the beam increases by the square of the distance from the horn axis. This causes focusing of off-axis particles. The second horn focuses mainly overfocused particles by horn 1 and some of the particles that passed through the horn 1 neck.

The NuMI target and horns can be configured to produce different energy spectrums of neutrinos [6]. The horns are stationary, but the target is mounted on a remote-positioning module. It can be moved longitudinally over a 2.5m distance. At larger distances, the horns produce a higher energy neutrino beam. This is because the particles entering the field region of the horns tend to proceeed at smaller angles off the target, that is at higher energies. The horns focus higher energy mesons to produce higher energy neutrinos. A variable energy beam is useful to explore a larger region of parameter space and to understand the systematics of the NuMI beam and MINOS detectors.

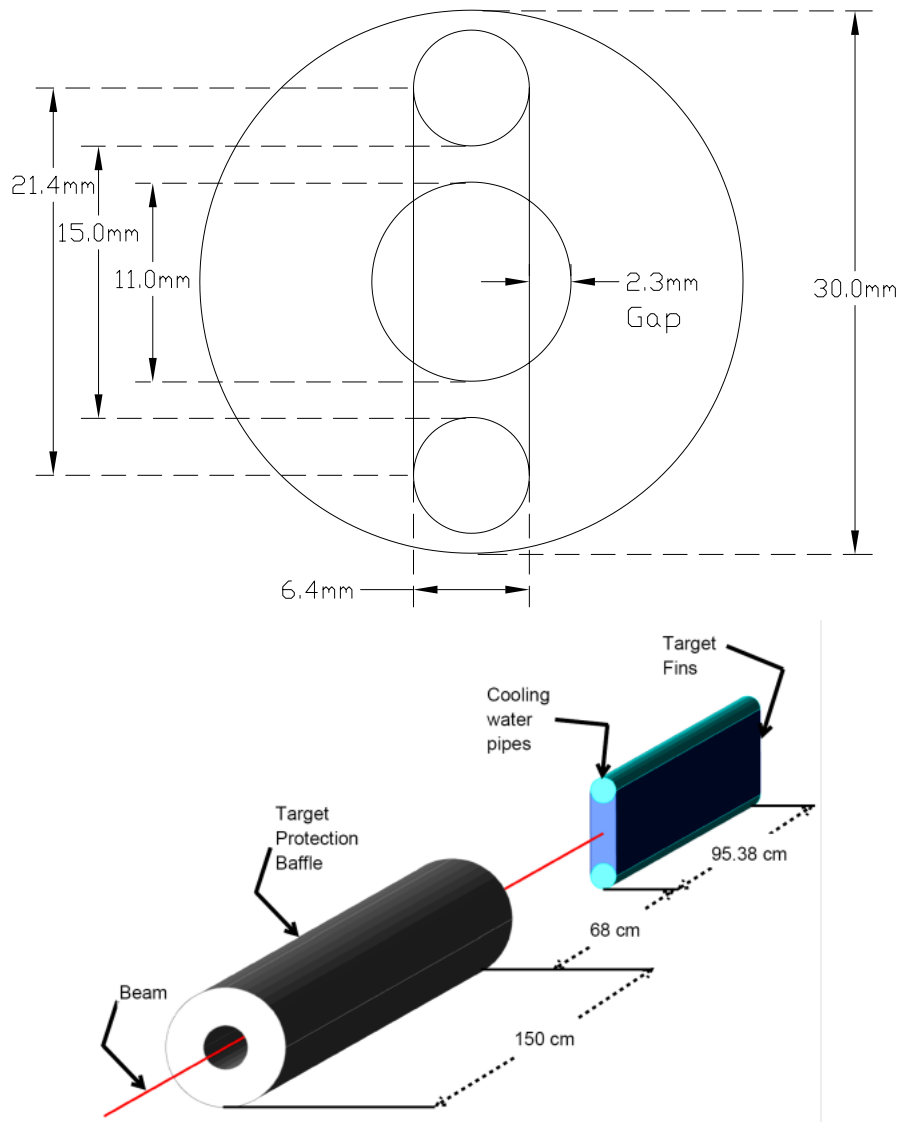

Figure 1.4: Shown is a diagram of the target baffle system. Beams eye view of the target and baffle (Top). View of the target-baffle system from upstream beam-right (Bottom). A 2.3mm gap between the target and baffle can permit most of the proton beam to proceed to the hadron monitor without interacting in the target.

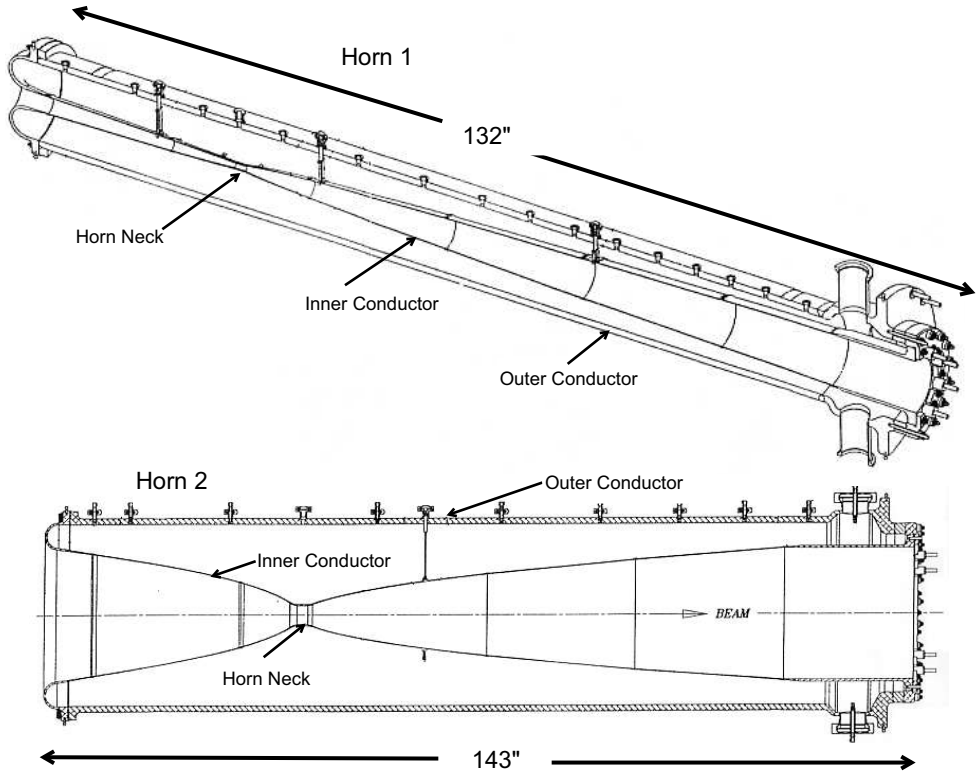

Figure 1.5: Cross-sectional side view of the NuMI horns. The horns consist of an empty no-field region about the axis surrounded by a parabolically countoured inner conductor.

Three positions have been established and are shown in Fig. 1.6. In the Low Energy (LE) position, the target snout actually extends into horn 1. The target is retracted 100cm for the Medium Energy (ME) position, and 250 cm for the High Energy (HE) position. A fourth configuration was established due to target issues, in which the target is retracted 10cm from the LE position. This is called the LE10 position, and it has been the operating condition for the NuMI for most of its tenure. In the LE10 position, the horn current is reduced to 185 kA. The intention is to duplicate the energy spectrum of the

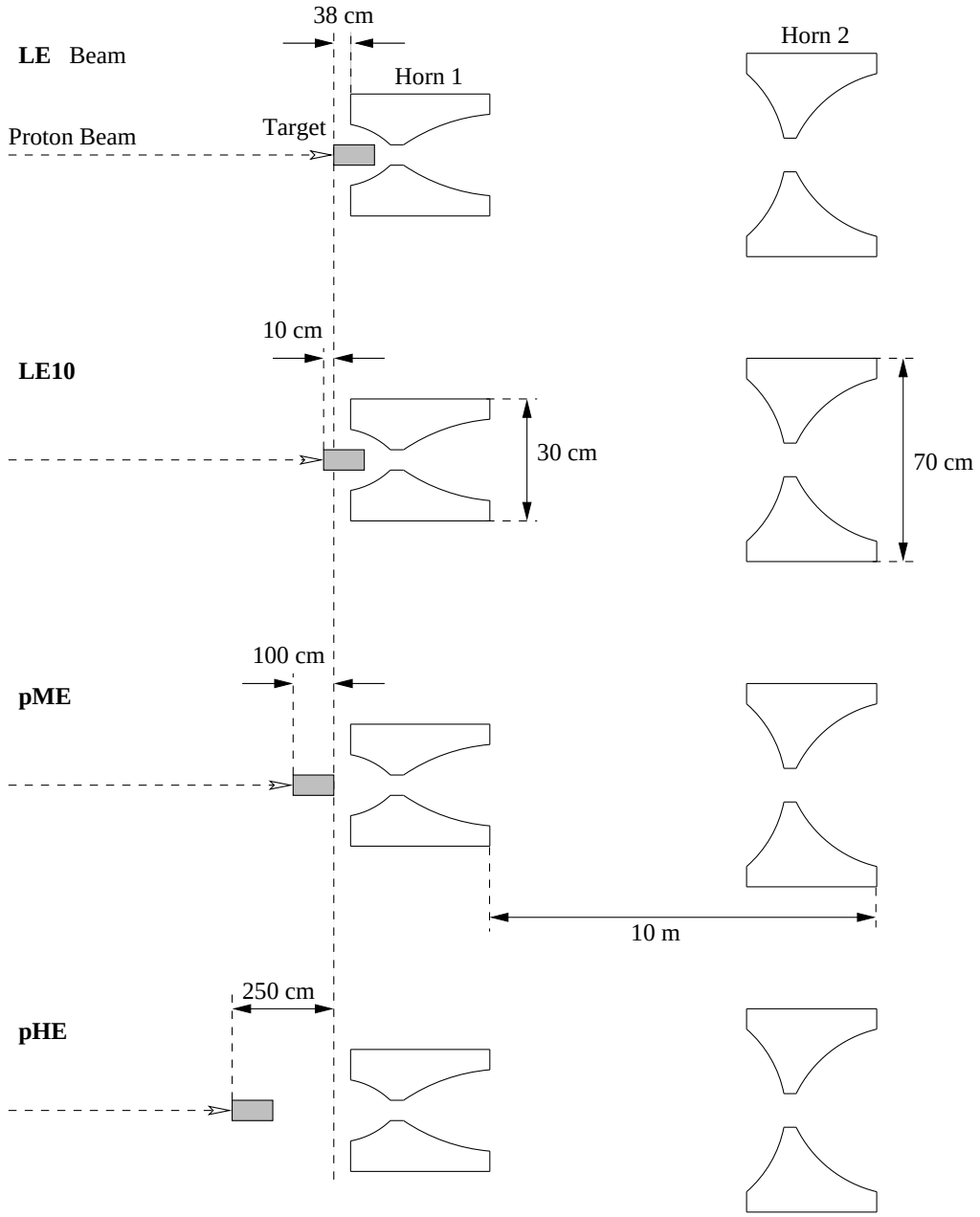

Figure 1.6: Target horn configurations for three established kinds of neutrino beam energy spectrums [6]. Figure courtesy [10].

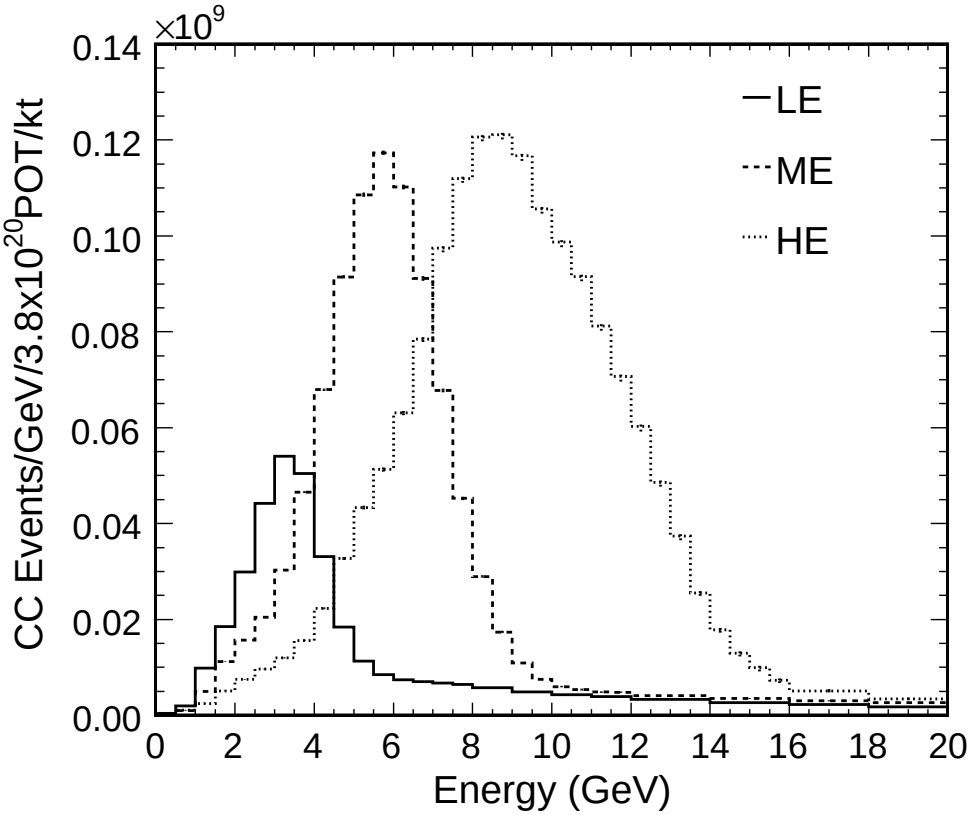

Figure 1.7: The neutrino interaction rates in the near detector for the LE, ME, and HE beam configurations illustrated in Fig. 1.6.

LE beam. The LE10 beam has the same peak energy, but with a few percent less flux. Interaction rates for the HE, ME, and LE beam configurations are given in Fig. 1.7.

1.2 NuMI Beam Monitoring System

It is necessary to know the flux and energy composition of the neutrino beam to extract measurements of the oscillation parameters. The MINOS near detector

Fluences @ the Beam Monitors	LE	pME	pHE
Hadron Monitor (10^7/cm^2/10^{12}ppp)	6.8	6.8	6.8
Alcove 1 (10^5/cm^2/10^{12}ppp)	6.5	10.0	9.0
Alcove 2 (10^5/cm^2/10^{12}ppp)	0.9	5.0	7.2
Alcove 3 (10^5/cm^2/10^{12}ppp)	0.35	0.5	2.3

Table 1.1: Maximum particle fluences expectated to be seen by the beam monitors for three target-horn configurations. The fluences are determined from Monte Carlo simulations as described in [12, 13]

measures these properties 1000m downstream of the target. The Far Detector is located another 735.4 km away. The experimental precision of MINOS is limited by the ability to extrapolate near detector measurements to the far detector. Monte Carlo simulations indicate that changes in the beamline like target-horn alignment, optics performance, target integrity, and beam position can significantly change the near-far extrapolation. While the near detector can detect such changes in principle, the low interaction rate prevents fast diagnosis. It can take weeks to accumulate enough date to diagnose a problem in the target or the optics. A better approach is to observe the secondary and tertiary beams, and use that information to monitor the neutrino beam.

NuMI has a beam monitoring system composed of 4 arrays of ionization chambers, one hadron monitor and three muon monitors. These monitors obtain intensity information of the hadron beam and the tertiary beam, and they provide transverse profiles. As shown in Table 1.1, the monitors see fluences between 10^6 and 10^9 charged particles/pulse/cm^2. Such large fluxes can measured to sufficient precision to monitor the hadron and muon beam every spill. The hadron monitor sees substantially larger doses than the muon monitors, and this motivates a more robust design. The monitors are used to align the remnant hadron beam at the end of the decay pipe, and they provides

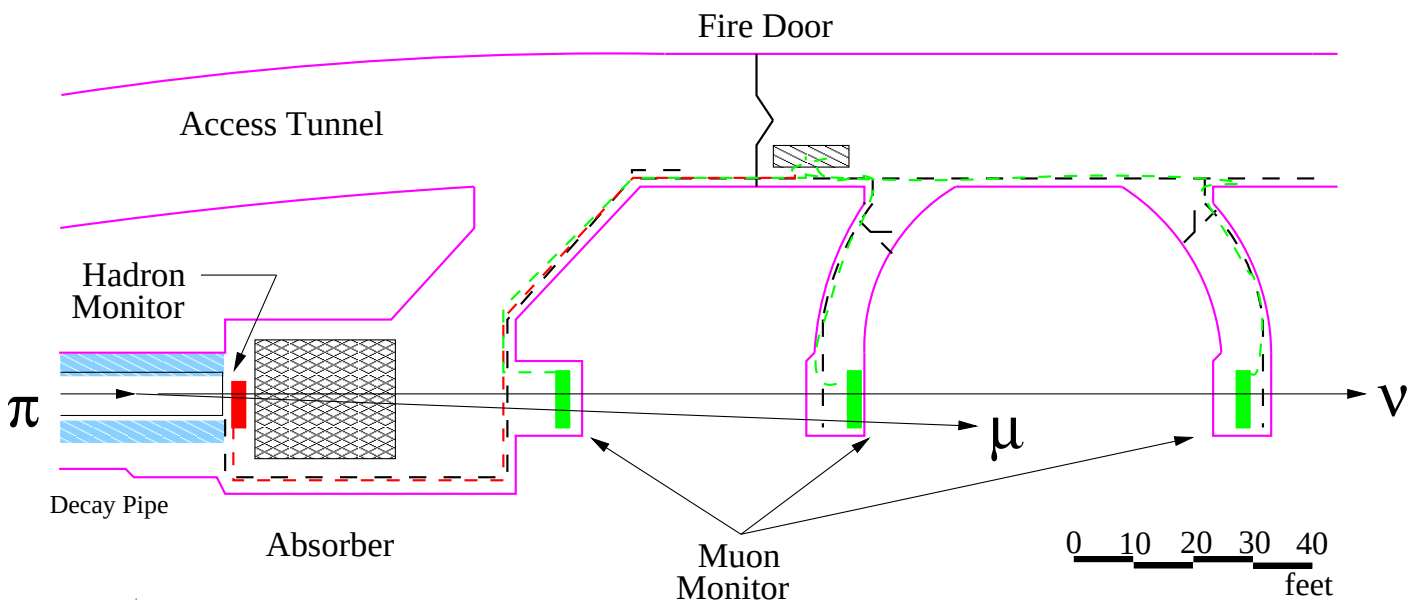

Figure 1.8: Diagram of the absorber hall and alcoves in the NuMI Beamline: The hadron monitor is inserted prior to the absorber to observe the remnant hadron beam, and the muon monitors are placed in three alcoves further downstream.

checks on short and long-term stability of the beamline as well as information about the neutrino beam quality.

1.2.1 Hadron Monitor

The hadron monitor provides a transverse profile of the charged particle intensity between the decay pipe and the absorber. This information is used primarily to monitor the integrity of the target and baffle. The beam at the hadron monitor is composed mostly of non-interacting protons and hadrons from the target [12]. Therefore, it is largly immune to the effects of the horns.

The hadron monitor is used to align the proton beam. The beam direction is known to 1" transversely over a 725m lever arm from the target, which yields a 40μrad ascertainment of the beam angle. Also, the target-baffle system and the horns were surveyed using beam-induced hadron monitor signals and BPM or profile monitor position measurements [10]. The RMS and the beam intensity provide a measure of beam quality that can be used to diagnose target failures as described in Chapter 5.

The hadron monitor sees charged particle fluxes of up to $10^9/\text{cm}^2/\text{spill}$ during high intensity normal operation. Radiation dose rates are expected to be up to 1.3×10^9 rad/year, primarily from uninteracted protons from the primary beam [12, 19]. Such high dose rates prohibit the use of organic materials. Residual radiation levels can reach 100mrem/hr, and the aluminum body of the detector may be activated to several rem/hr. These high radiation levels make repair imposible and provide challenges for replacement and disposal of a failed device.

The temperature in the hadron monitor region is expected to range between 95°F and 105°F. The temperature differential across the monitor may

be as much as 10°F. The ambient pressure will be at atmospheric pressure, and may modulate with temporal variations and the activity of the fans [12]. The variations in temperature and pressure can modify chamber response, so the hadron monitor area is instrumented to track these quantities.

1.2.2 Muon Monitors

The three muon monitors measure the spatial profile of muons in excavated alcoves downstream of the absorber. Each muon monitor has a different threshold energy for muon detection, since charged particles range out in the intervening dolomite rock between the alcoves. This provides a coarse measure of the muon beam energy spectrum. One can also extract a measure of neutrino beam intensity and direction from the muon monitor profiles. The relative intensities can be used to diagnose horn malfunctions and to verify the neutrino production expectations in the near detector. The monitor is intended to measure the beam angle to 100μrad off the target, which corresponds to about 3". This sets constraints on the precision of the calibration as described in Chapter 3.

In the LE configuration charged particle fluxes of up to 2×10^7 /cm^2/spill in the center pixel and radiation levels of up to 14 MRad/year. The HE beam configuration produces fluxes up to 3.5×10^7/cm^2/spill and up to 25 MRad/year, though NuMI only operated in the HE configuration for a period of two weeks over its year of running. The radiation levels and fluxes are more concentrated at beam center, so the dose is nonuniform over the surface of the detector [19, 13]. Though the radiation levels are substantially lower than those for the hadron monitor, we use radiation hard components as in the case of the hadron monitor. The radiation levels are sufficiently low to allow

exchange and repair of the detectors during beam downtime.

1.3 Ionization chambers

The hadron and muon monitors are array of ionization chambers with helium gas in an airtight vessel. The chambers consist of parallel plate electrodes with a bias voltage applied across the gap. Incident particles ionize the chamber gas. The ionized particles drift to the electrodes. The amount of charge collected is ideally proportional to the incident particle flux.

1.3.1 Physics of Ionization Chambers

Figure1.9 illustrates the characteristic behavior of an ionization chamber. At low applied bias, charges drift slowly to the electrodes and are apt to recombine in the gas or attach to impurities. There is a stable region, the plateau, over which all of the ionized charge is collected. At high field, the ionized particles gain enough energy between collisions in the gas to ionize gas molecules, producing amplification of the initial ionized charge, or gain. In this region, charge collection efficiency varies dramatically with the applied bias. The signal response is also sensitive to environmental conditions such as temperature and pressure. Therefore, it is not the ideal operating condition.

Ionization chambers can come in different geometries. The parallel plate geometry, shown in Fig. 1.10, allows for a uniform electric field which prevents premature amplification by localized regions of high field. Parallel plates also allow for small electrode separation. This is useful to prevent losses in charge collection due to screening effects [30, 31]. At high incident intensities, electromagnetic screening can decrease the effective field experienced by ionized

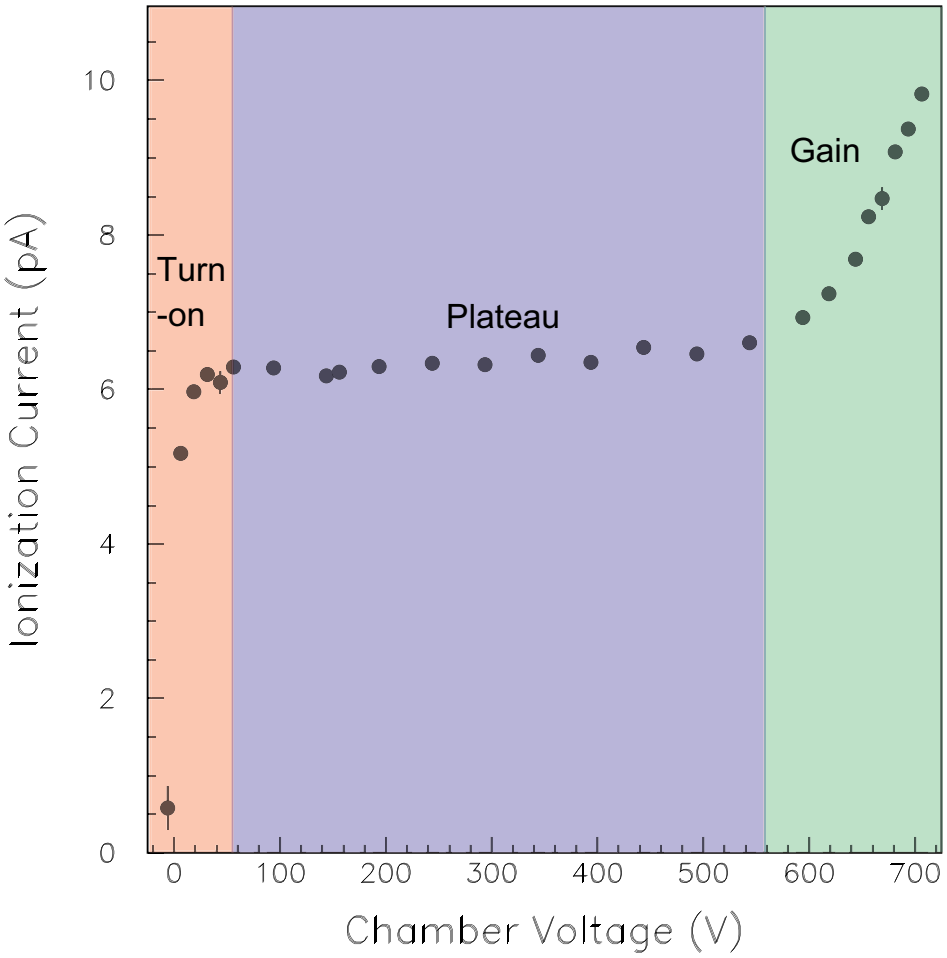

Figure 1.9: Plateau curve from a 5mm gap parallel plate ionization chamber irradiated by a PuBe radionuclide source. At low applied bias voltage, ionized charge can recombine before it is collected. At high applied bias, ionized charge can reionize the gas, causing amplified signals.

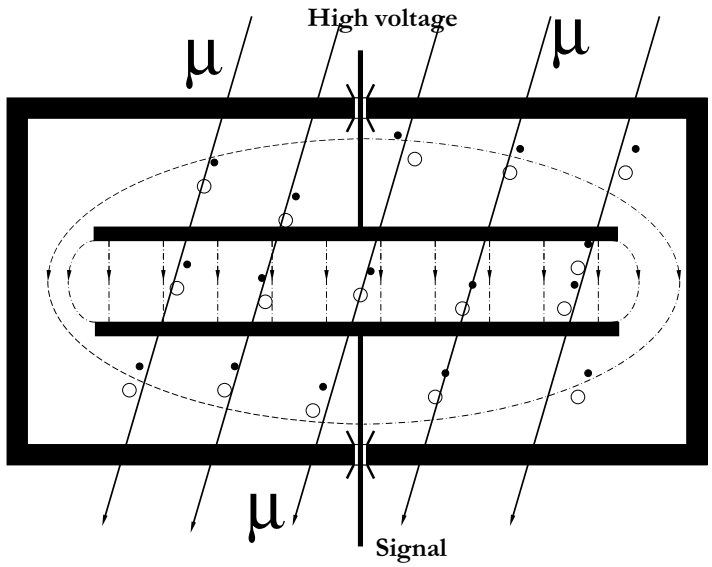

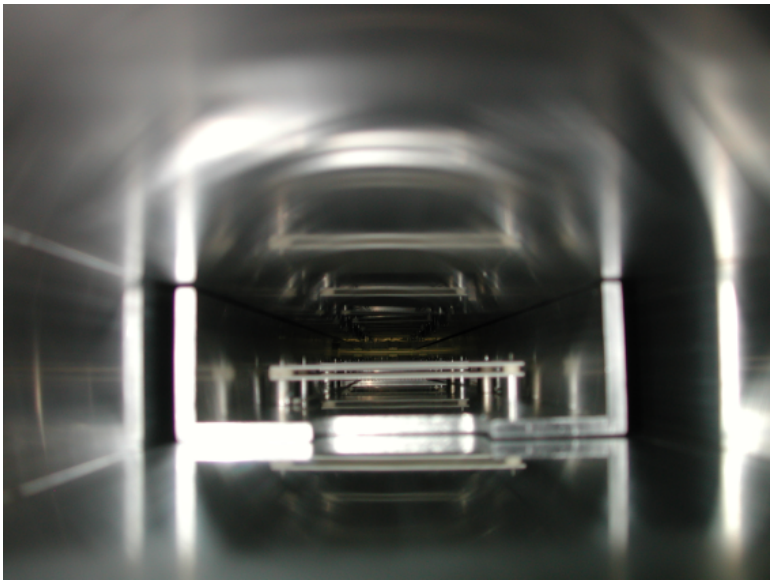

Figure 1.10: Diagram of an ion chamber (top) [10]. Muons ionize the gas, and the ions collect on the electrodes under the influence of the bias. Stray field in the large external volume can also collect on unshielded signal lines. Also shown is a chamber in a muon monitor tube (bottom).

particles. Helium gas was chosen as the filling gas, since it has the highest ionization potential and low density, resulting in the least charge build-up within the chamber volume. The gas is high purity (.99995%) to minimize electron attachment of ionized particles to impurities and to maximize chamber lifetime. The gas is exhausted into the air, so the monitors operate at about atmospheric pressure.

1.3.2 Chamber Construction

The plates used in the beam monitors are shown in Figs. 1.11 and 1.12. One plate serves as a high-voltage pad, to which a positive bias is applied. The other plate has a 1cm guard ring surrounding a 3" $\times$ 3" interior sense pad. The signal from a chamber is the ion charge collected on the sense pad only. The guard ring ensures uniform field over the sensitive region. Significant variations in the electrode spacing would result in variation of the electric field across the ionization chamber. Such variations are undesirable, as portions of the chamber might be in amplification mode when most of the chamber is operated at the upper end of the voltage plateau (see Figure 1.9). Alternatively, lower electric fields in portions of the chamber result in larger charge loss due to space charge build-up from the beam.

The plates are made of 4"$\times$ 4" Al_2O_3 ceramic wafers with .0005" thick platinum-silver electrodes [15]. Ceramic tends to be radiation resistant, and the stiffness and flatness of the plates permits milimeter gaps between the electrodes. This helps maintain good charge collection efficiency at high beam intensity. The plates are separated by precision washers of 1mm and 3mm thicknesses for the hadron monitor and muon monitors, respectively. Electrical connections are made by soldering to the solder pads around the mounting

Figure 1.11: High voltage ceramic plate (left) and signal plate (right) for the ion chambers in the hadron and muon monitors. In the signal plate, a .5 mm guard ring is electrically isolated from the 3"×3" sense pad area. This is to eliminate the effects of fringe fields.

holes.

The small electrode spacing in the hadron monitor motivates more uniform plates to be used than in the muon monitor chambers. The flatness of each hadron monitor plate was determined by supporting the plate on a granite table and measuring elevations of twenty-five points on the surface with a dial indicator. The Hadron Monitor plates were chosen amongst those which have a flatness of better than 12 μm. The RMS flatness of the plates for use in the muon monitors were allowed to vary by as much as 25 μm. The thickness of the washers was gauged by measuring a 100 washer sample with a caliper. The washers were found to be accurate to 12 μm. Fig. 1.13 shows the measurements of the spread in the hadron monitor and muon monitor plates, and Fig. 1.14 shows a histogram of the thicknesses of a sampling of hadron monitor and muon monitor washers. Figure 1.15 shows the breakdown voltage in Helium gas for each of the 300 chambers in the muon system after assembly.

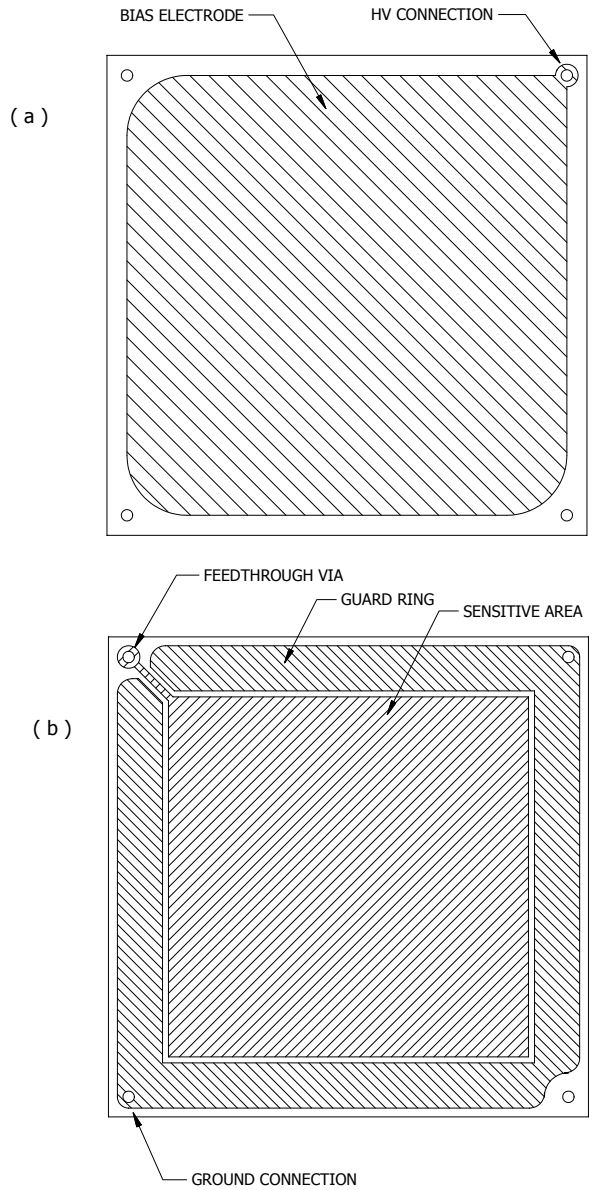

Figure 1.12: Drawing of the high voltage plate (top) and signal collection plate (bottom) and for the ion chambers in the hadron and muon monitors. The top left mounting hole of the signal board reads out the signal from the interior sense pad. The top right hole of the HV board delivers voltage to the HV pad.

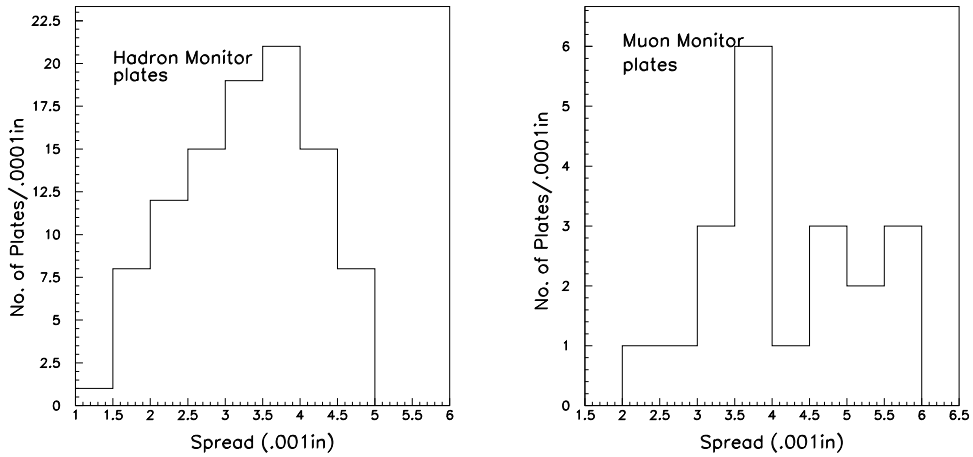

Figure 1.13: Shown are the spread in the hadron monitor plates, the spread in a sample of muon monitor plates. The 'spread' is defined as the largest 2-point difference among the 25-point elevation measurement for a give ceramic plate.

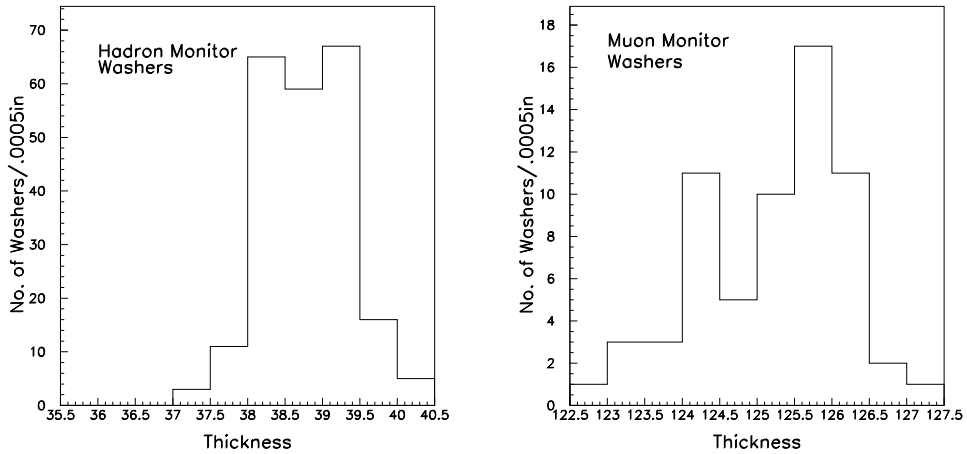

Figure 1.14: Shown are histograms of the thickness measurements of the hadron monitor washers and the muon monitor washers.

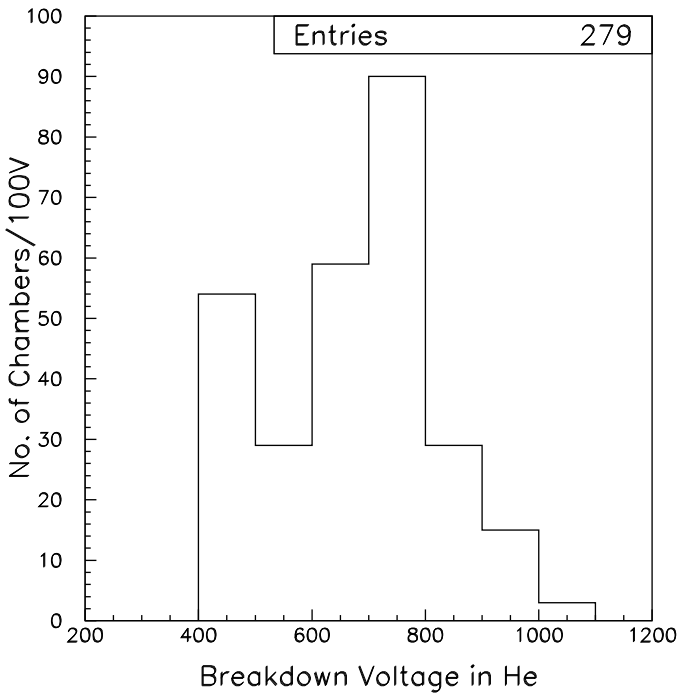

Figure 1.15: Histogram of the breakdown voltages for all of the muon chambers. The breakdown voltage is determined by applying a bias to the HV line at the endplate feedthrough and determining when the current draw exceeds 10μA.

All chambers can reach 400 V applied bias.

In the interest of suppressing stray ionization collection, the conductor components of the chambers are insulated and shielded. Our ionization chambers are contained in a gas volume which is entirely susceptible to ionization by an incident beam. The active volume is some fraction of the total gas volume. Ionized particles outside of the active volume recombine unless they drift under the influence of stray fields. If this happens, charge may collect on the signal conductor and distort the chamber response. A diagram is shown

in Fig. 1.10, in which stray fields can cause spurrious charge to collect on the chamber lines. In bench tests, it was shown that insulating the signal conductors and adding a grounded cover suppressed stray ionization from collecting on the signal lines [14]. This effort is shown to be successful to better than a 5% change in signal over 300V in as shown in Figs. 5.1 and 5.2.

1.3.3 Cleaning

Care was taken to construct and maintain the chambers and their components in a clean environment. Particulates and oils can cause premature chamber degradation and short circuits. They also can compromise chamber performance by introducing impurities into the gas medium. Additionally, hydrocarbons on the walls of the ionization chambers increase "wall-effects," whereby neutrons in the beam line can interact with the chamber materials, sending highly-ionizing recoil nuclei into the chamber gas.

All of the chamber components except the chamber plates themselves were ultrasonically cleaned using a Branson ultrasonic cleaner[16]. The components were submerged in a water soluble aluminum cleaning solution and the cleaned for 20 minutes[17]. Finally, the chamber components underwent an isopropyl alcohol or methanol rinse to get rid of residual water that might oxidize the chamber components.

The muon monitor trays and tubes were scrubbed with a citrus biosolvent at least three times and then rinsed with alcohol[18]. Aluminum cleaner was applied to the body of the hadron monitor and scrubbed thoroughly. The hadron and muon monitor bodies were judged clean when rubbing the surface with an alcohol damp kimwipe revealed no oil residue.

Finally, the hadron monitor feedthroughs and the muon monitor alu-

minum gaskets were baked at 250°F for 60mins to ensure leaktight seals.

1.3.4 The Hadron Monitor

The Hadron Monitor, shown in Figure 1.16, is a o.835 $\times$ 0.835m vessel that encloses a 7 $\times$ 7 array of ionization chambers. The vessel baseplate and walls are 1/8" aluminum. A lid encloses the gas volume defined by the base plate and anterior walls by compressing a gasket made of lead-tin solder against the anterior wall flange. The posterior walls extend behind baseplate by 2" to cover the feedthroughs and interior cabling. A thin aluminum plate (not shown) covers the array of cables and feedthroughs. The 49 ion chambers are spaced by 4.5" center to center, leaving .5" gaps between them.

A cross-sectional diagram of a single chamber is shown in figure 1.17. Each chamber is mounted to the aluminum baseplate via two stainless steel threaded rods and two .092" diameter stainless steel rods. The signal pad is on top, and the HV pad is nearest the backplane. The unthreaded rods form the center conductors of ceramic feedthroughs that penetrate the baseplate [20]. A stainless steel threaded sleeve is welded to the outer jacket of the feedthrough. Together with an aluminum gasket,[1] it forms a leaktight seal against the aluminum baseplate. The threaded rods are mounted in aluminum posts that screw into the baseplate. These rods serve to ground the signal pad guard ring to the vessel. Solder is applied to two corners of the HV pad and to all four corners of the signal pad to fix their positions. It must be applied to the front side of the HV pad that faces the chamber gap and to the rear face of the signal pad. The ceramic washers fit around the solder blob to maintain consistent spacing. Finally, PEEK caps are placed over all of the threaded

[1] Alloy XXXX Aluminum, which is particularly soft and compressible. These gaskets were actually washers, and heat treated at XXX°C to remove any temper.

rods to shield the conductors from stray ionization.

The high radiation levels of the hadron monitor's intended environment motivate the use of radiation resistant material and a simple design. It is 26 kg in mass with an effective density of .39 g/cc. Aluminum is chosen as an alternative to stainless steel due to the shorter lived radioisotopes that are produced in the presence of high energy beam. Also, care was taken to minimize the material in the hadron monitor due concerns of handling and storage after being activated.

Cables run from each high voltage feedthrough to the beam-right wall of the hadron monitor vessel, as shown in Fig. 1.18. The HV lines can carry up to 300V during special studies, though they nominally operate at 130V. The cable in the vessel is a custom coaxial cable with two insulators, kapton and a ceramic tube. This redundant insulation was motivated by concern for voltage breakdown. Though the kapton is expected to survive in a high radiation environment, its breakdown will not result in a short due to the ceramic. A grounded aluminum sheath encloses the line to form a coaxial cable. Cables run in a criss-crossing pattern from the signal and high voltage feedthroughs to the beam-right wall of the hadron monitor. Outside of the more extreme radiation region, the custom cables transition to kapton cable with a ground braid. The electrical connection of the ground braid to the aluminum sheath is physically maintained by aluminum brackets mounted to the side wall (see Fig. 1.18).

The hadron monitor is intended to align the beam to 40μrad, so the hadron monitor's absolute position with respect to the beamline must be known to 1", and it is important that its position be fixed over the period of operation. Therefore, a support structure is developed, installed, and surveyed according to the procedure described in Section 2.1.

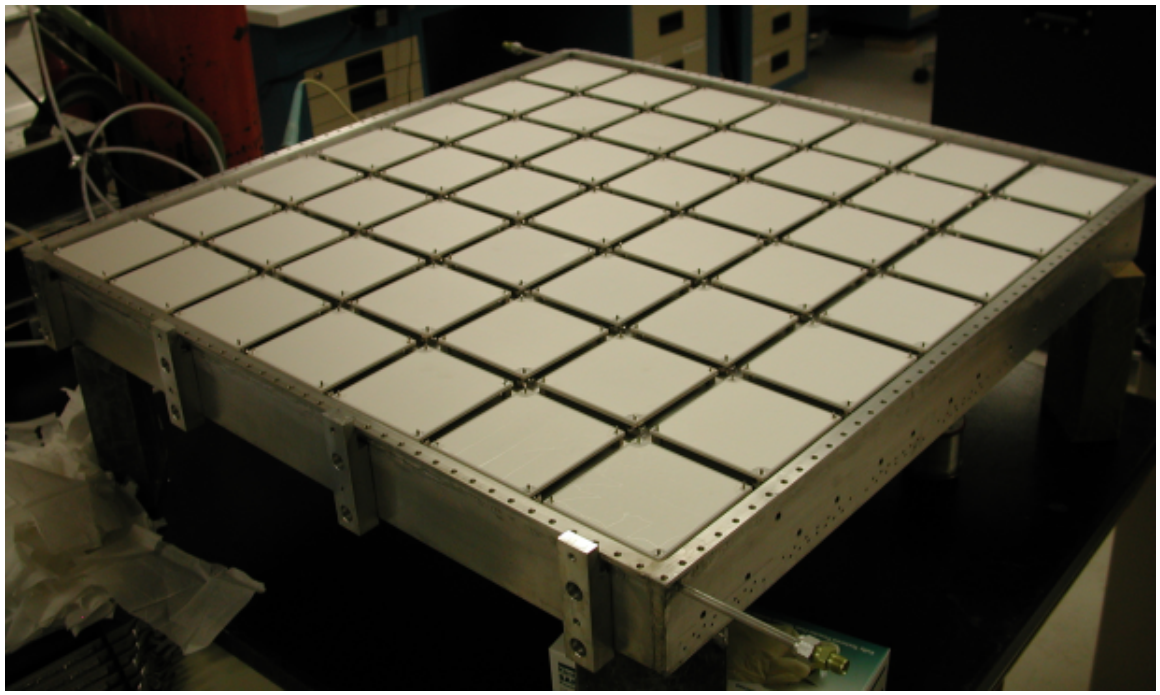

Figure 1.16: Hadron monitor ion chamber array.

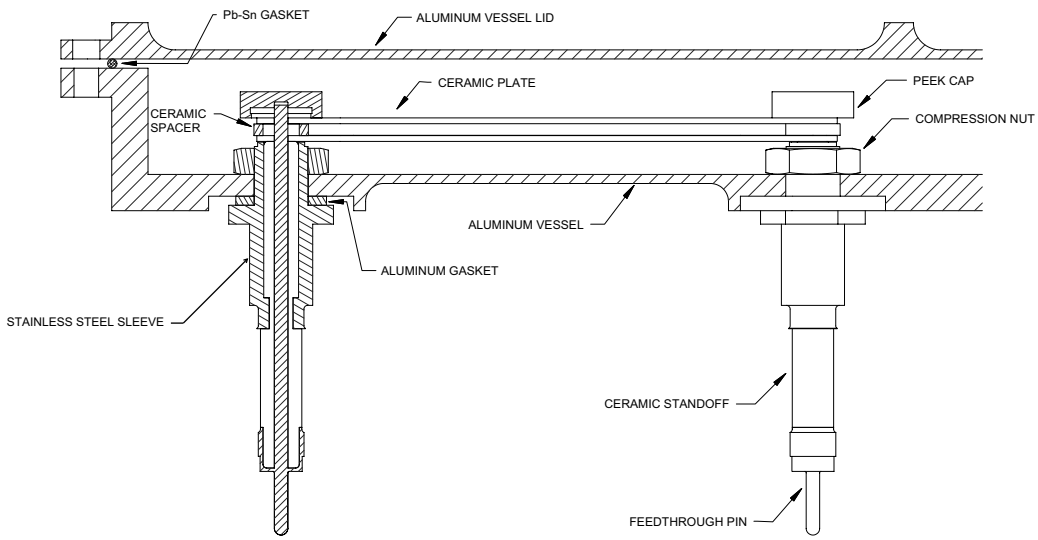

Figure 1.17: Crossectional view of an ion chamber in the hadron monitor.

Each pixel in the hadron monitor was relatively calibrated according to the procedure in Chapter 3. After installation in the NuMI beamline, each hadron monitor pixel was response-tested in situ by applying a 5 volt pulse from a signal generator to the high voltage line. If the chamber is operational, the pulse produces a charge on the signal line. In this way, the correspondence of signal channel and HV channel was verified. During calibration, all the hadron monitor channels were operational, but the in situ response-test after transport and installation of the device indicated that chamber 12 no longer worked.

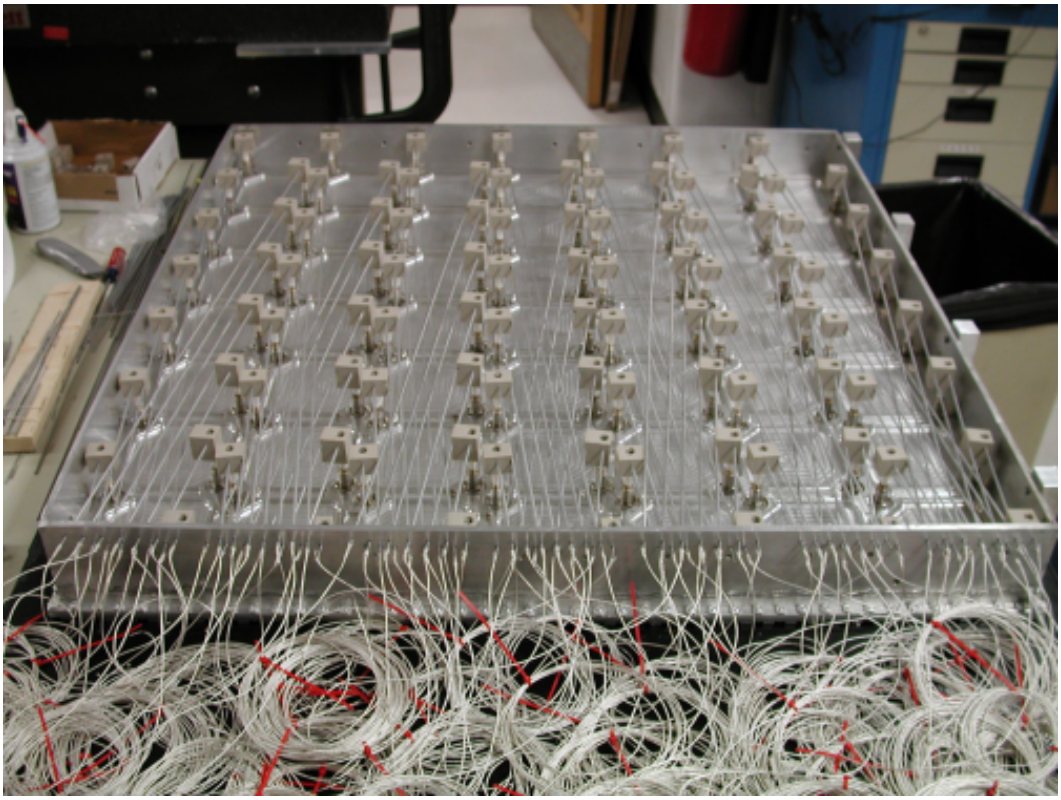

Figure 1.18: View of the hadron monitor cabling configuration. Cables run in a criss-crossing pattern from the signal and high voltage feedthroughs to the beam-right wall of the hadron monitor. The custom cables transition to kapton cable with a ground braid. The electrical connection of the ground braid to the aluminum sheath is maintained by aluminum brackets mounted to the side wall.

1.3.5 The Muon Monitors

The three muon monitors are each 9×9 arrays of ion chambers. Each monitor consists of 9 tubes mounted vertically, and each tube houses 9 ionization chambers. The ionization chambers are spaced by 10", therefore spanning a 2×2 m^2 area. The three alcoves require 27 tubes altogether. There are additionally 5 tubes constructed, three of which are spares and two are reserved as control devices to help characterize radiation affects.

The muon monitor chambers are assembled in Aluminum "tubes," as shown in Figure 1.19. In each tube, 9 ionization chambers are fixed to a 90" long, 2"×5" U-channel as shown in Fig. 1.19. The tray is 1/8" thick. A stainless steel endplate is bolted to one end of the channel.

Four standoffs screw into 1/4-28 tapped holes on the tray to mount a chamber as shown in Fig. 1.19. Two of the standoffs are aluminum, and two are PEEK plastic with stainless steel sheaths. Threaded rods screw into the standoffs and solder onto the high voltage and signal plates to secure the pads. The rods fixed in the PEEK standoffs are hollow, affording room for a signal or high voltage line which is soldered to the rod. The rods are in turn soldered to the signal or HV pads. The bottom plate is the HV pad, and the top plate is the signal pad.

Signal lines and high voltage lines of bare capton cable run from the hollow rods through the PEEK mounts to the channel base as shown in Fig. 1.20. A PEEK cap covers the rod. It is recessed to allow room for the solder blob. Upon exiting the PEEK standoff, the kapton is shielded by a ground braid soldered to the stainless steel cover of the PEEK mount. The coaxial kapton cable is routed along the tray beneath the intervening chambers toward the feedthrough endplate. Aluminum brackets interspersed between chambers

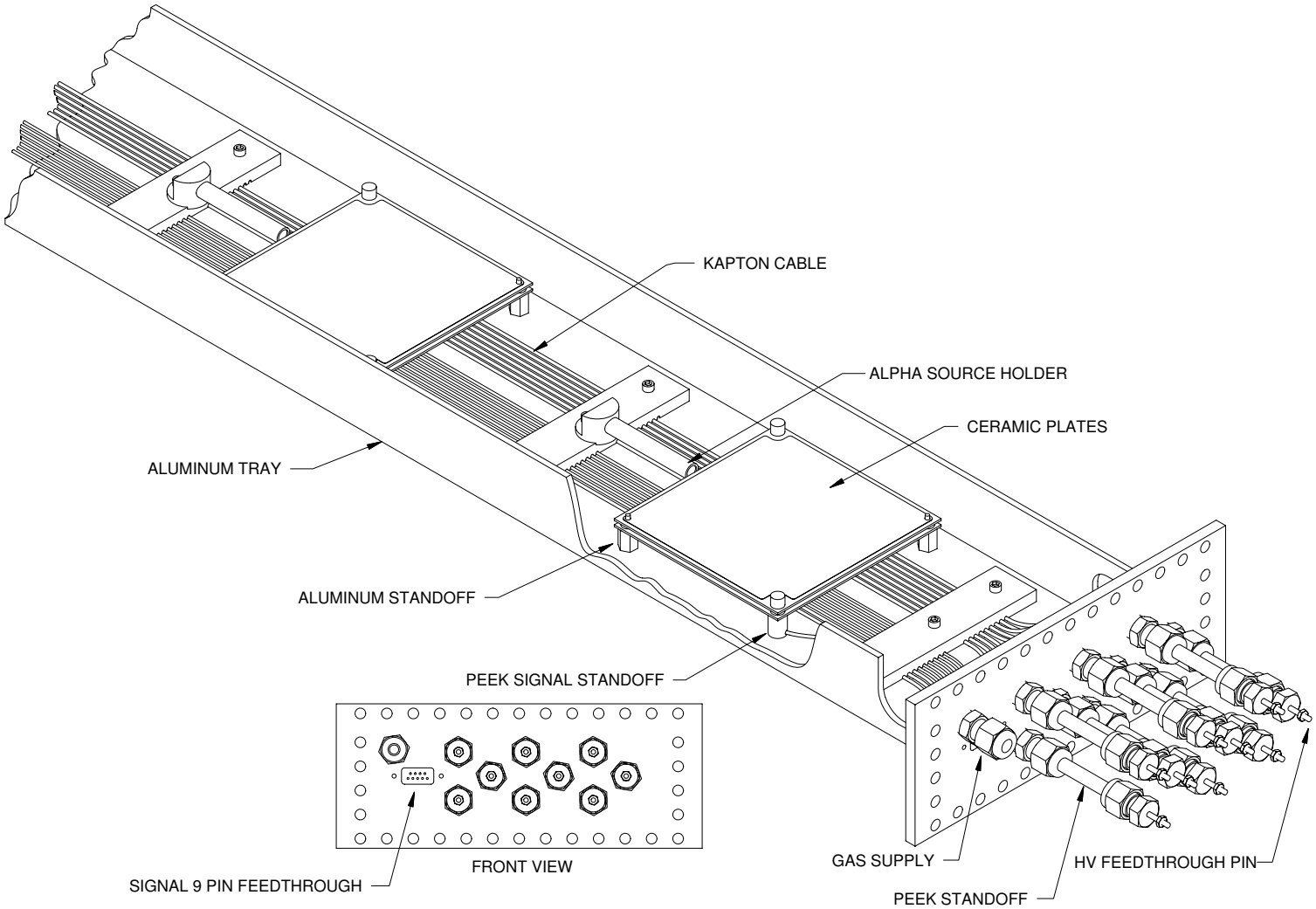

Figure 1.19: Diagram of a muon monitor tube [10]. Nine chambers are mounted to a 90" long channel. An endplate is fastened onto the channel.

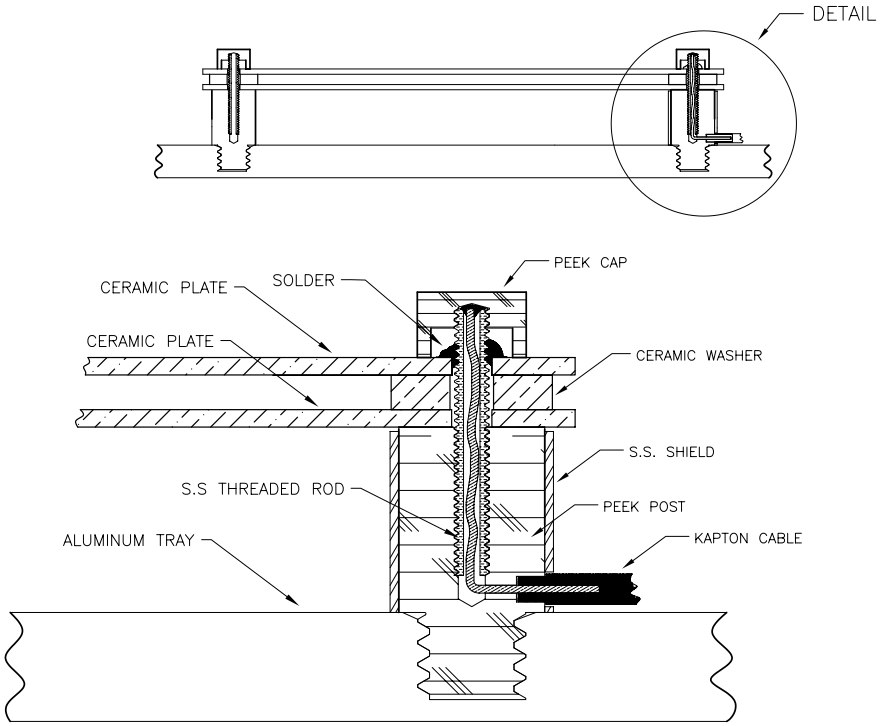

Figure 1.20: Close-up of a PEEK standoff mounted on the mumon monitor tray. Capton cable runs through the interior of the standoff and is soldered to the hollow threated rod. A PEEK cap covers the rod to prevent the accumulation of stray ionization.

fasten the cables to the tray.

Each high voltage line culminates in one of nine PEEK feedthroughs as shown in 1.19. The signal lines are routed to a 9-pin D connector made of PEEK plastic. The cable ground braid and insulator is stripped, and the inner conductor is soldered to gold-plated pins which are sandwiched into the D-connector halves which are in turn bolted together. The PEEK serves to allow for easy connection of the signal lines, and protects the exposed wire from accumulating stray charge.

Nine alpha sources are mounted on the aluminum brackets, and each illuminates a chamber gap. These sources provide a small current of a few pAs intended to be used to as a "heartbeat" to diagnose chamber malfunctions and as a calibration tool during normal NuMI operations. However, this calibration was not possible due to the tiny signals they produce. Moreover, chamber response to the alpha sources as a function of gas density is much different than chamber response to the muon beam: low energy alphas, entering from the side of the chamber, can, with higher gas density, range out before entering the sensitive gas volume. In contrast to ∼GeV particles from the beam which induce larger ionization currents with higher gas pressure, the alpha sources produce a smaller ion current which varies chamber-to-chamber depending upon the relative placement of the alpha source holder to the chamber.

The U-channel is fastened to an endplate. The HV cables are connected to feedthroughs, and the signal lines transition to a 9-pin connector. The electrical connections are insulated by PEEK plastic to minimize exposure of the signal lines to ionized gas, and the ground braid is grounded on both ends.

The tray and endplate slide into a 90" long 6×2 rectangular tube with 3/4" thick flanges welded on both ends. The non-feedthrough end of the channel has a cut out that fits around a welded aluminum plate with two 1/4-20 tapped holes. This plate is welded to the interior of one end of the tube. A large plate with 1/4-20 clearance holes is fixed over the channel and used to clamp the channel in place, as shown in Fig. 1.22. The connector endplate and a rear endplate are sealed against the flanges of the tube with compressed aluminum gaskets.

As in the case of the hadron monitor, each muon monitor is instrumented with pressure transducers and resistive temperature detectors (RTD). During the calibration process, as described in Chapter 3, it was shown that

chamber response varies with temperature and pressure. While the temperature and pressure of the muon monitors is expected to be uniform, comparing the relative rates between different alcoves requires pressure and temperature corrections to be applied. Characterization of chamber response to these environmental quantities is described in Chapter 5.

1.4 Chamber Numbering Conventions

Figure 1.21 shows the numbering scheme for indexing chambers in the hadron monitor. This numbering scheme was used during construction, calibration and for in-beam operations. Chambers increment from left to right, starting at top left (as viewed by the beam).

The chamber numbering convention for muon monitors runs from 1 through 9, starting with the feedthrough end of a muon tube. See Figure 1.22. The chamber numbering convention was used during construction and calibration of each muon tube. During the construction and calibration procedure, we numbered tubes consecutively from 1 to 32, in chronological order of fabrication.

Upon installation in the NuMI beam, a channel numbering convention was adopted to describe the entire array of 9×9 chambers within an alcove. The in-beam numbering follows yet a different convention, running from 1 to 81 within each alcove, as will be discussed in the next chapter.

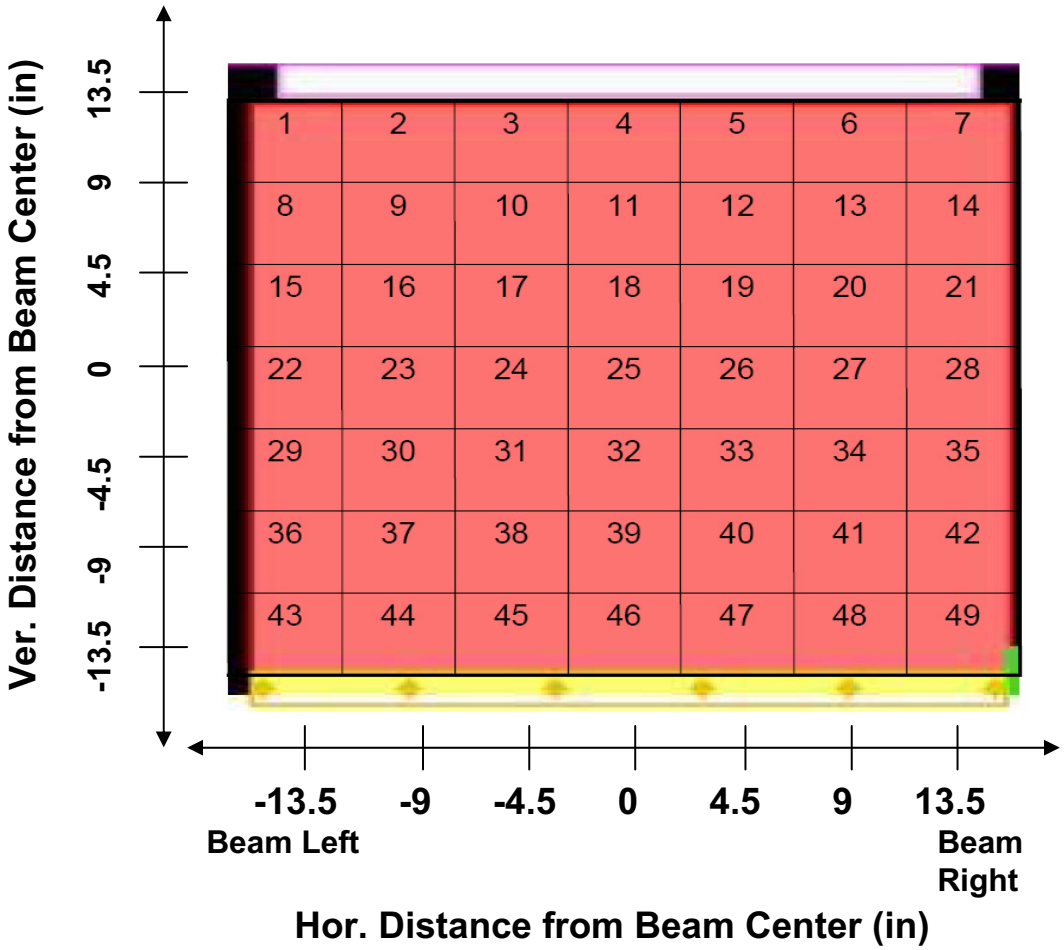

Figure 1.21: Beam's eye view of the hadron monitor. The chambers are numbered according to the scheme used for the calibration process.

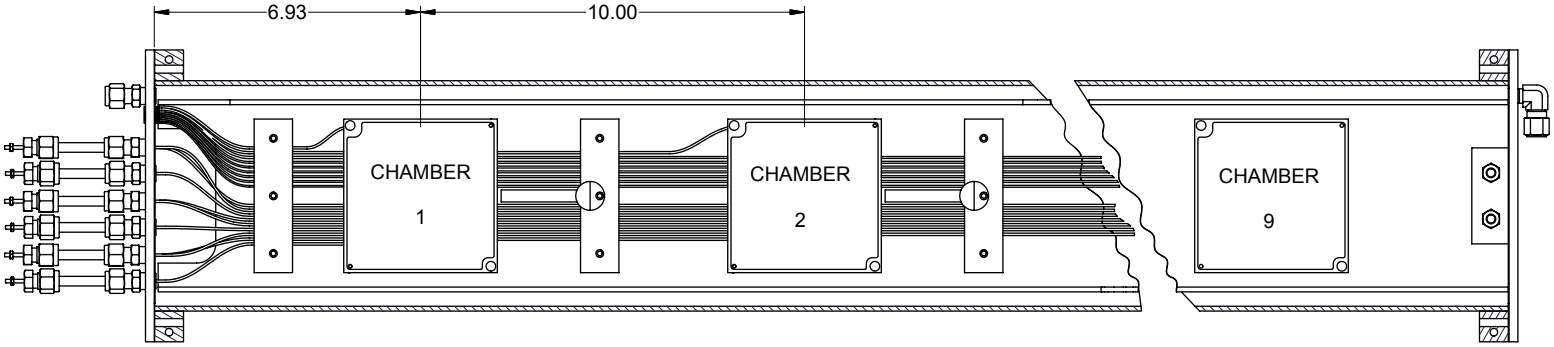

Figure 1.22: A single muon tube with indices corresponding to the calibration mapping of chambers.

Chapter 2

Beam Monitor Installation

2.1 Hadron Monitor Installation

The Hadron Monitor is located inside the NuMI absorber concrete stack. It sits in a small air gap in between the NuMI decay pipe and the absorber's Aluminum core.[1] This air gap is completely surrounded by a stack of concrete shielding blocks. Because of concern over radioactivation of air by the beam, the stack must be as hermetically sealed as possible. This prompts insertion and removal of the device to be accomplished through a narrow, 6" wide by 54" tall slot in the absorber concrete. During beam operation the slot is covered over with a 9" thick steel door.

The hadron monitor is inserted into its final position at beam center via a pair of Aluminum rails which constrain its location transverse to and along the beam axis. The hadron monitor is mounted so that it stands vertically. It is not tilted at the 3.6° declination angle of the beam, so it is only horizontally orthogonal to the beam. The hadron monitor rails were installed and measured

[1] An Aluminum box filled with Helium gas fills the volume between the absorber core and the hadron monitor.

while free access to the absorber interior was possible. Figure 2.1 shows the two aluminum rails mounted in the concrete blocks. Visible in this photo are the decay pipe, a portion of the concrete which surrounds the air volume between the decay pipe and absorber core, and some of the blue steel blocks which will support the core.

The rails constrain the position of the Hadron Monitor. The vertical position with respect to the beam is determined by the lower rail, on which the monitor slides on rollers. The horizontal location is fixed by pushing the monitor through the concrete slot until it reaches a hard 'stop' fixed to the lower rail. This hard stop, furthermore, constrains replacement monitors to come to the same position. The upper rail acts as a guide to prevent the monitor from tipping over.

2.1.1 Design Drawings

Figure 2.2 shows a view of the hadron monitor installed on its rails inside the concrete stack, looking upstream into the beam. Several locations of interest are the ideal beam center (labelled 'A'), the top surface of the lower rail, the location of the hard stop, and the lower surface of the upper rail. Dimensions in the figure are those for the ideal placement of the rail with respect to beam center. Variance from the ideal vertical location can be accomodated up to 2" because of adjustable feet on the hadron monitor.

Figure 2.3 shows the view of the installed hadron monitor as seen through the slot, *i.e.* looking from the East towards the West. Figure 2.4 shows the view from the top. The horizontal dashed line at the center of the figure is the beam axis, which we could indicate during installation using a laser.

2.1.2 As-Installed Drawings

Figure 2.5 shows the location of the rails after installation. To determine these positions, we relied on measurements from the surveyors as well as measurements we made using a tape measure. Thus, the accuracy of our final determinations is of order better than 1/4".

The surveyors located and labelled in the concrete several targets, numbered 100-120. Two of these, 109 and 117, are shown in Figure 2.5. We were given the vertical distance of these markers to the ideal beam center at the z location of the slot in the concrete. We then measured the vertical distance of our installed lower rail to these markers in order to determine the lower rail's vertical distance from beam center. This distance is given in the drawing as "Dimension A" and "Dimension B". From our measurements, these dimensions are the same to within 1/16" (hence the rail is level). We confirmed that the rail is level using a 4' bubble level.

We find that the rail is 21.62" below beam center, to be compared with 20.33" desired, so it is 1.3" low. The hadron monitor must be raised by this amount on its feet prior to insertion. We also find that the upper rail is 39.25" in height above the lower rail, to be compared with 38.90" desired. This difference may be accomodated by the upper rail, which is actually a pair of rails spaced apart from one another by 3/8". These two rails sandwich a fin which protrudes from the top of the hadron monitor. This scheme prevents the monitor from tipping, while not placing tight constraints on the rail's vertical location.

Figures 2.6 and 2.7 show that the lower rail may be installed at the incorrect position in the z direction, *i.e.* along the beam line. It is 14.56" from the decay pipe, as measured by taking a tape measure directly horizontal

from the rail to the edges of the decay pipe endcap. This is to be compared with ∼10.7" desired distance to the decay pipe. The value of 10.7" is derived from the drawings which indicate 6.26" desired distance from the top of the decay pipe to the rail, and factoring in the fact that the decay pipe top is approx 1.7meters higher than our rail together with the 3.5° tilt of the decay pipe. This is likely due to a slightly different stacking of the concrete than described in our possibly out of date drawings. The z location, fortunately, is not critical. Note from our tape measurements that, if the decay pipe endcap is truly perpendicular to the beam axis, then the hadron monitor rail is within 1/16" across 90" of being perpendicular to the beam.

Figure 2.7 shows the top view of the installed lower rail. Of note is the measurement of the distance from the hard stop to the beam center, which came out exactly to the desired 16.25". Thus the monitor should be properly centered on the beam in the left-right view when installed through the slot and butted against this marker. The beam center line was was provided by the surveyors' laser plumb, which is a laser mounted on a rotating gyroscopic head to define a line throughout the absorber cavern. This line was guaranteed vertical by virtue of the gyroscope and was made to hit the target on the decay pipe window visible in Figure 2.5, as well as the surveyors' chalk line on the floor indicating the beam position. The largest uncertainty on our beam centering in this direction is the accuracy of the laser plumb, which did wander by 1/4" over the course of a couple days.

Figure 2.1: Concrete Stack surrounding the NuMI decay pipe. Upper photo: In the foreground are the steel blue blocks onto which the absorber core will later be stacked. The Aluminum rails for the hadron monitor are already installed in the concrete surrounding the decay pipe. A 6" slot in the concrete, not visible from this direction, allows the lower rail to protrude into the passageway at the far left. This protruding rail allows installing the monitor in on its rollers, and this lower rail can extension can be removed to close up the slot during running. Lower photo: the rails are anchored at each end via brackets which bolt to the concrete. The anchors have adjustable feet which permit the rails to be raised/lowered and levelled. The lower rail has a hard stop against which the hadron monitor is butted, visible just right of beam center.

Figure 2.2 key	
Label	Description
A	Beam Center
B	W Wall
C	Top of Slot & E Wall
D	Top of Upper Rail
E	Bottom of Upper Rail
F	Top of Lower Rail & Hardstop-Roller Junction
G	Outer wall
H	Bottom of Lower Rail

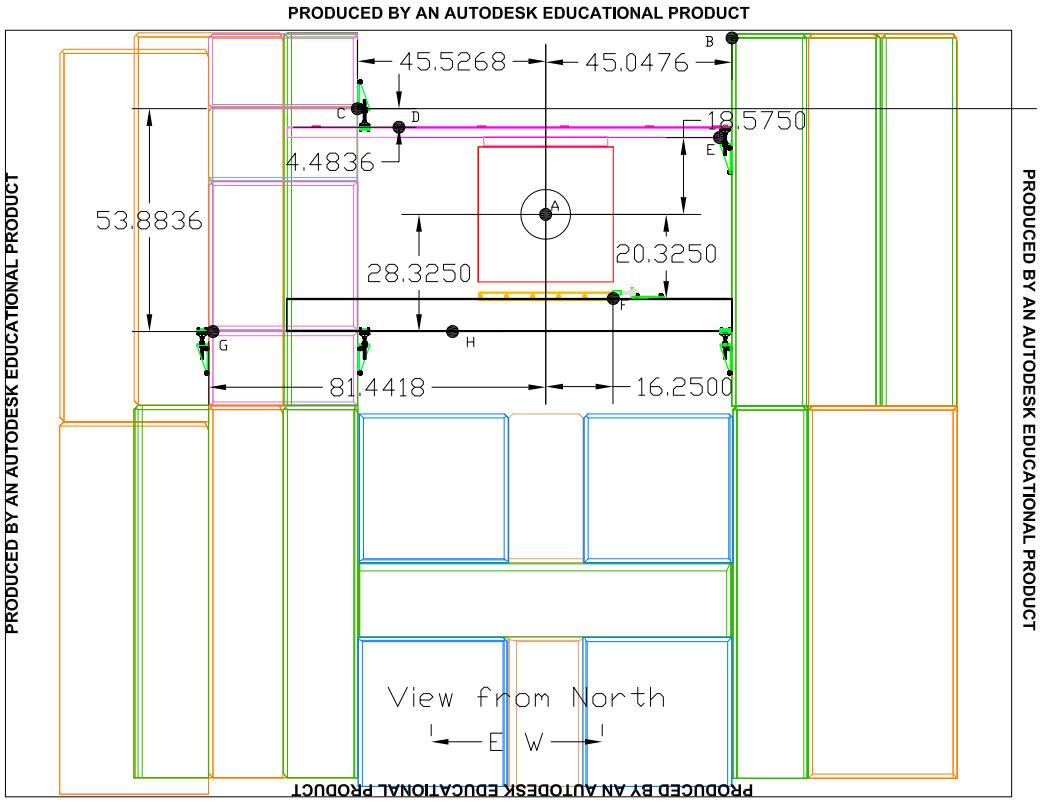

Figure 2.2: Construction drawings for installing the hadron monitor support structure. This is the view looking upstream at the monitor with the absorber core absent. This drawing is based on absorber drawings from C.James (3/04). All dimensions derived from the drawings.

Figure 2.3 key	
Label	Description
A	Top of Slot
B	Bottom of Slot & S Wall
C	S Edge of Top Face of Lower Rail
D	Bottom of Slot & N Wall

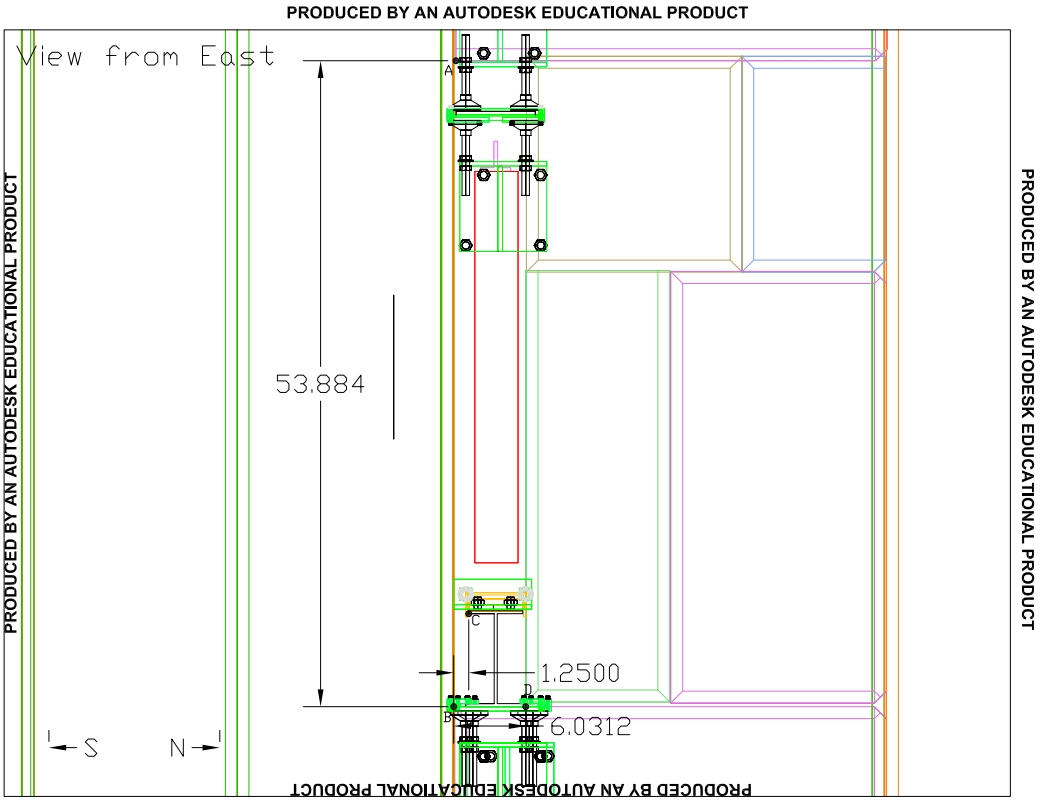

Figure 2.3: Construction drawings for installing the hadron monitor support structure. This is the view looking through the 6" slot on the east side of the concrete. This drawing is based on absorber drawings from C.James (3/04). All dimensions derived from the drawings.

Figure 2.4 key	
Label	Description
A	Beam Center
B	W Wall
C	Roller-Hardstop Junction

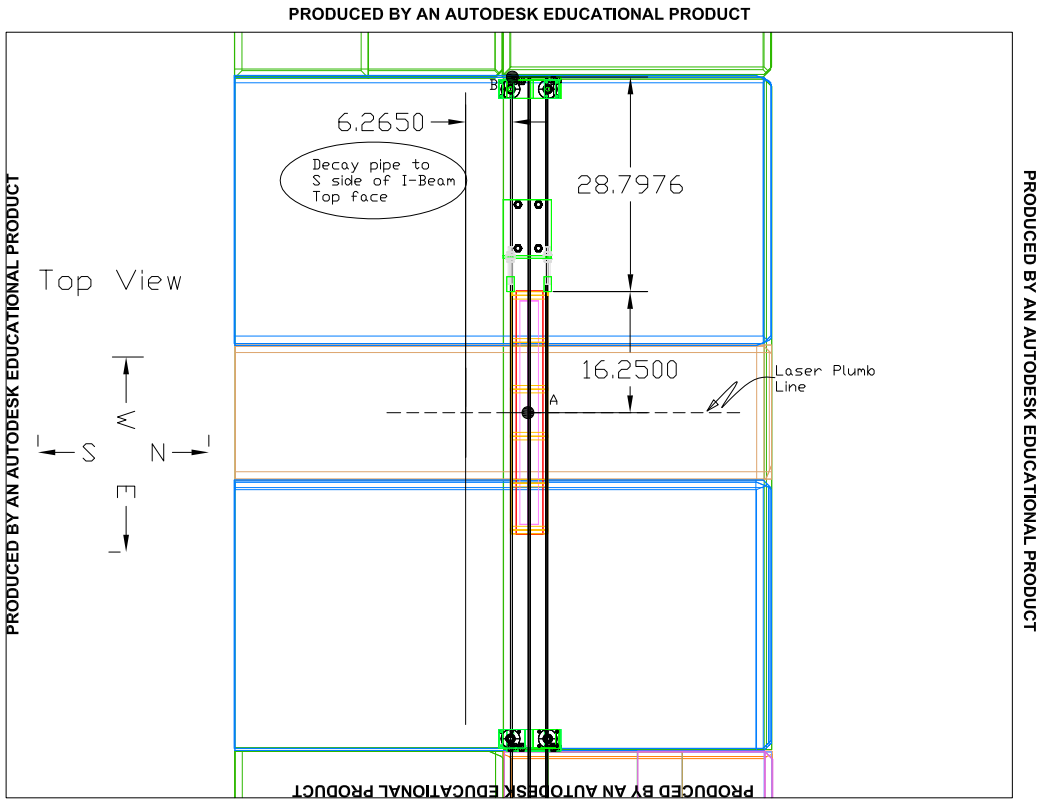

Figure 2.4: Construction drawings for installing the hadron monitor support structure. This is the view looking at the lower hadron monitor rail from above. This drawing is based on absorber drawings from C.James (3/04). All dimensions derived from the drawings.

Figure 2.5 key	
Label	Description
A	Beam Center @ HM Location
B	Top of Enclosure & E Wall
C	Top of Enclosure & W Wall
D	Bottom of Upper Rail
E	Bottom of Upper Rail
F	Top of Lower Rail
G	Top of Lower Rail and W Wall
H	Marker 109 given by Surveyors
I	Marker 117 given by Surveyors
Dim A	21.664 (Derived from surveyors measurement of the Height of beam center @ Marker 117 - Measured height of the top of the Lower Rail @ 117)
Dim B	21.575 (Derived from surveyors measurement of the Height of beam center @ Marker 109 - Measured height of the top of the Lower Rail @ 109)
Dim C	17.586 (Derived from Measurement of E to G - Dim A)

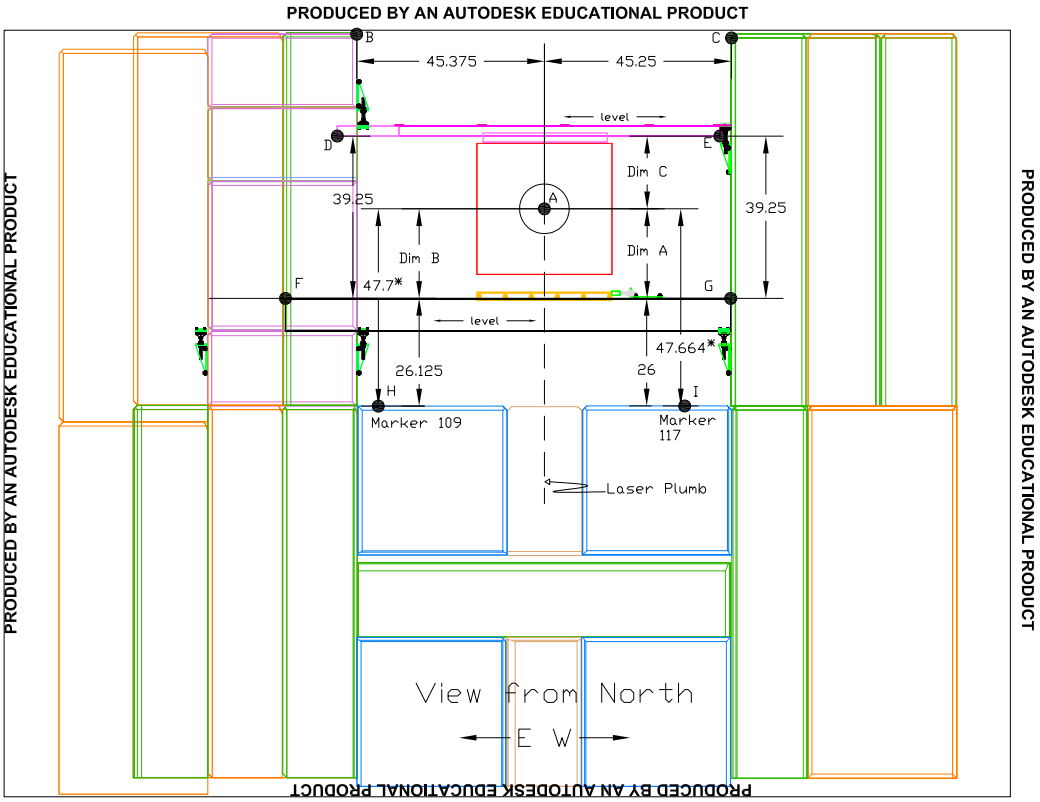

Figure 2.5: As-installed locations of the hadron monitor rails. All dimensions are direct tape measure measurements, with the exception of those indicated with a (*), which are provided by the surveyors. Dimensions A-C are derived from the above drawing (see Key).

Figure 2.6 key	
Label	Description
A	S Wall
B	Top Face of Lower Rail
C_t	Center of Top Rail
C_b	Center of Lower Rail

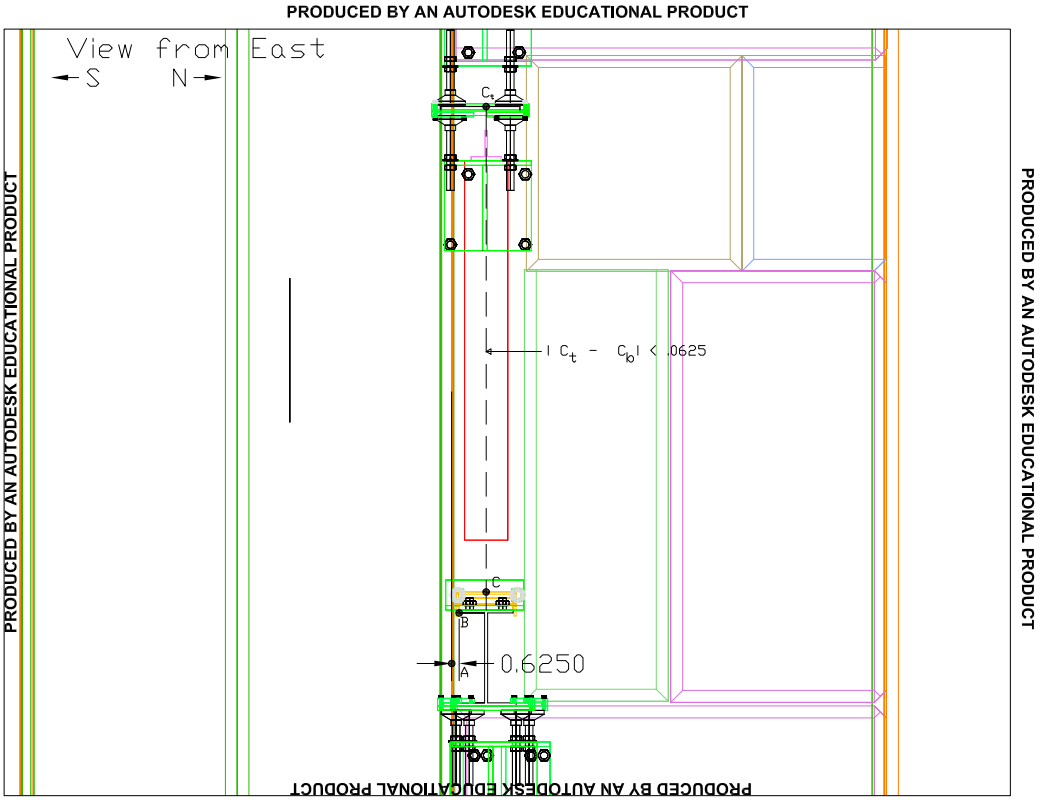

Figure 2.6: As-installed view of the hadron monitor through the 6” slot. All dimensions are measured with a tape measure.

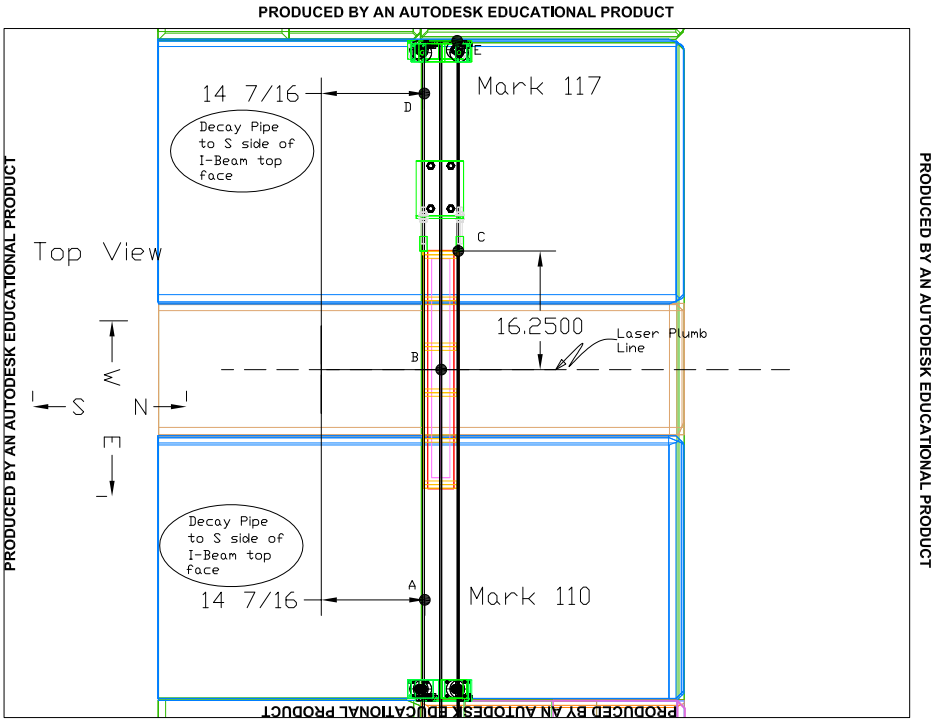

Figure 2.7: As-installed view of the hadron monitor lower rail, viewed from above. All dimensions are direct tape measure measurements.

Figure 2.7 key	
Label	Description
A	Top of Lower Rail @ Marker 110
B	Centerpoint
C	Roller-Hardstop Junction
D	Top of Lower Rail @ Marker 117

2.2 Muon Monitor Installation

Fig. 2.8 shows nine muon tubes installed on an aluminum support structure. Details on the design of the support structure are given in [21]. Mounting bars are bolted to tapped holes on the muon monitor tube flanges. The tube is then fastened to the support structure using clearance holes on both mounting bars. The connector endplates are on the low end to facilitate making electrical connections and repairing the muon tubes in place. A 1" diameter gas manifold on the top feeds helium gas into each tube and another identical manifold at the bottom funnels the gas into 30' long polyethylene tubing that is exhausted into the alcove.

A nine-conductor cable runs from the signal connector on each muon tube to a junction box with nine inputs. The signal lines are connected to the individual conductors of a 50-pair twisted flat cable. The 81 channels of an alcove station requires two such cables to be used. These twisted flat cables are then routed to the readout electronics. Electrical connections on the signals were potted to prevent the collection of stray ionization.

Each muon station was aligned with respect to survey markers in the alcoves. These markers are accurate to 6mm with respect to the system of markers used by the surveyers. The support structures were aligned using laser lines and levels, tape measures, right angles, and plumb bobs. Each tube was spaced horizontally by $10 \pm 1/8$ inches. They were aligned vertically so that the lower endplates were consistently level to about 1mm. The pitch, yaw, and roll were measured to be within 10mrad of 0. It should be noted that the muon monitor is established vertically, and is therefore not orthogonal to the beam which proceeds at a 3.6° declination angle.

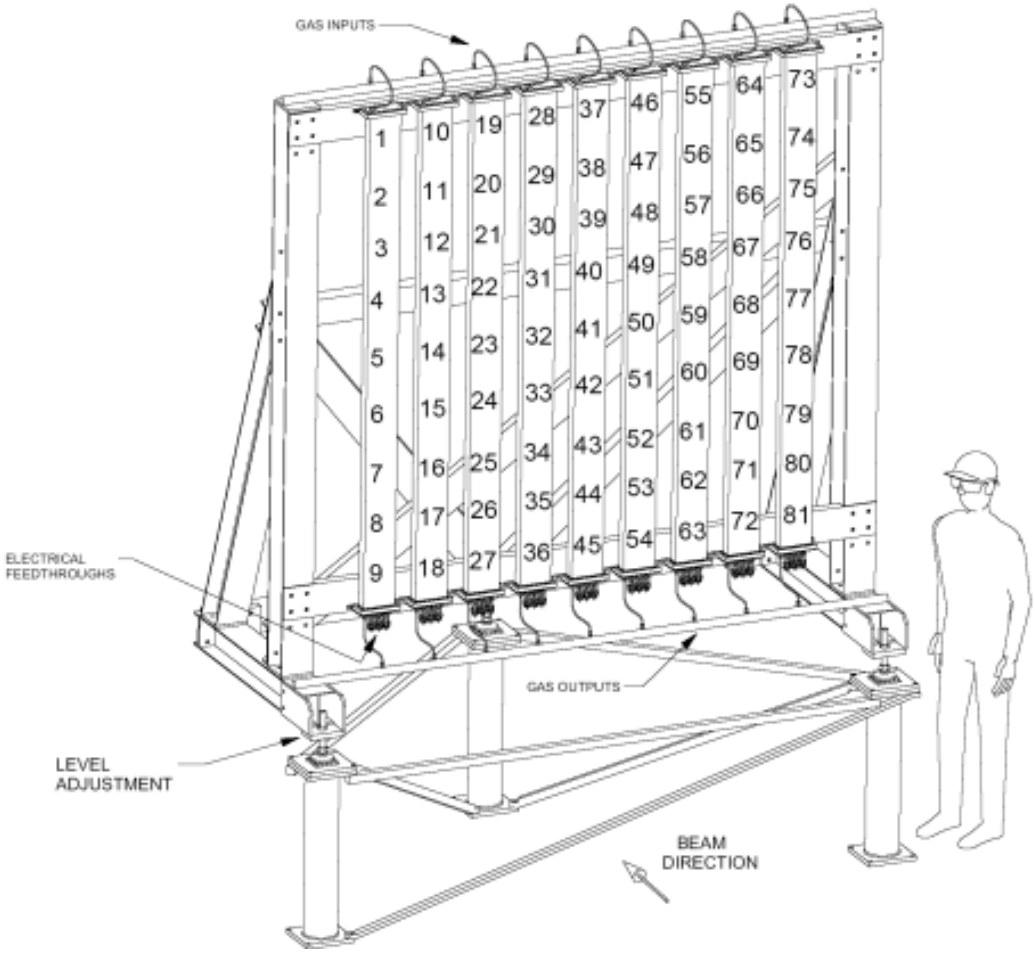

Figure 2.8: Diagram of the installed muon monitor and its support structure [10]. The nine tubes form a 9×9 ionization chamber array. Leveling mounts are used to align the muon monitor with respect to beam center.

Alcove	Tube Location*	Tube No.**
1	1	31
1	2	6
1	3	16
1	4	27
1	5	24
1	6	13
1	7	20
1	8	2
1	9	19
2	1	18
2	2	8
2	3	9
2	4	14
2	5	10
2	6	32
2	7	21
2	8	11
2	9	23
3	1	15
3	2	4
3	3	26
3	4	25
3	5	1
3	6	29
3	7	5
3	8	30
3	9	28

Table 2.1: Tube specification for each position in each Alcove during NuMI Running from Dec. 2004 to May 2006. *Tube location index from beam left to beam right. **Tube number corresponds to tube construction chronology.

Alcove	Tube Location*	Tube No.**
1	1	31
1	2	6
1	3	16
1	4	27
1	5	24
1	6	13
1	7	20
1	8	2
1	9	19
2	1	18
2	2	8
2	3	9
2	4	14
2	5	10
2	6	32
2	7	21
2	8	11
2	9	23
3	1	15
3	2	17
3	3	26
3	4	25
3	5	1
3	6	29
3	7	5
3	8	30
3	9	28

Table 2.2: Tube specification for each position in each Alcove during NuMI Running from May 2006 to present. *Tube location index from beam left to beam right. **Tube number corresponds to tube construction chronology.

2.3 Gas System

The hadron and muon monitors are under continuous flow of helium gas. The gas is high purity (>99.995%) in the interests of chamber performance and lifetime. A schematic of the gas system is shown in Fig. 2.9.

The gas is supplied by 8 helium cylinders that feed into a gas manifold. The cylinders provide a continuous supply that lasts three to four weeks. A dual-stage regulator maintains a constant output pressure of 60 psi [22]. The gas proceeds down a supply line (600') to the gas rack in the corridor adjacent to the alcoves and absorber hall. The gas line is then split to accomodate the 3 alcoves and the hadron monitor. The gas flow and pressure is measured on each of the four output lines, and analog outputs are connected to the readout electronics[23, 24]. Pressure transducers are also installed at the detectors, but those predictably failed early during operation due to radiation effects. The rack transducers are used to monitor the beam long-term. Also, an RTD is attached to each monitor to provide a temperature measurement[25]. Check valves at the racks and immediately downstream of each beam monitor ensure that the monitors do not become severly overpressured.

Tests of impurity level as a function of flow rate were performed using an Illinois Instruments Oxygen analyzer. The hadron monitor and alcove 1 were tested by installing the analyzer in series with the exhaust of each monitors gaslines. Fig 2.10 shows the results. The O2 level gradually diminishes as the flow rate increases for the muon monitor. The muon monitors operate at 10 L/hr, and the hadron monitor flow is set to 25 L/hr.

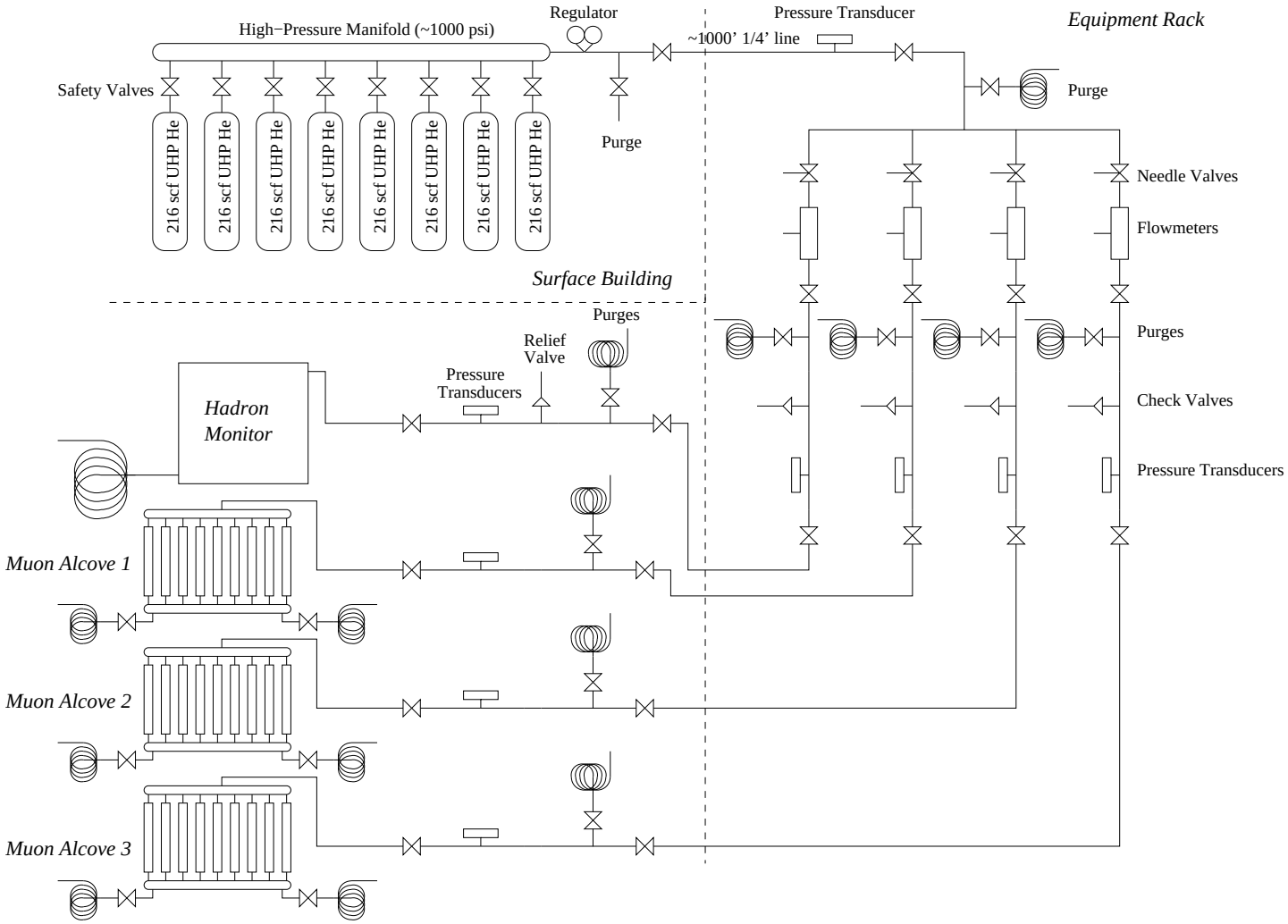

Figure 2.9: Schematic of the gas system for the beam monitoring system [10].

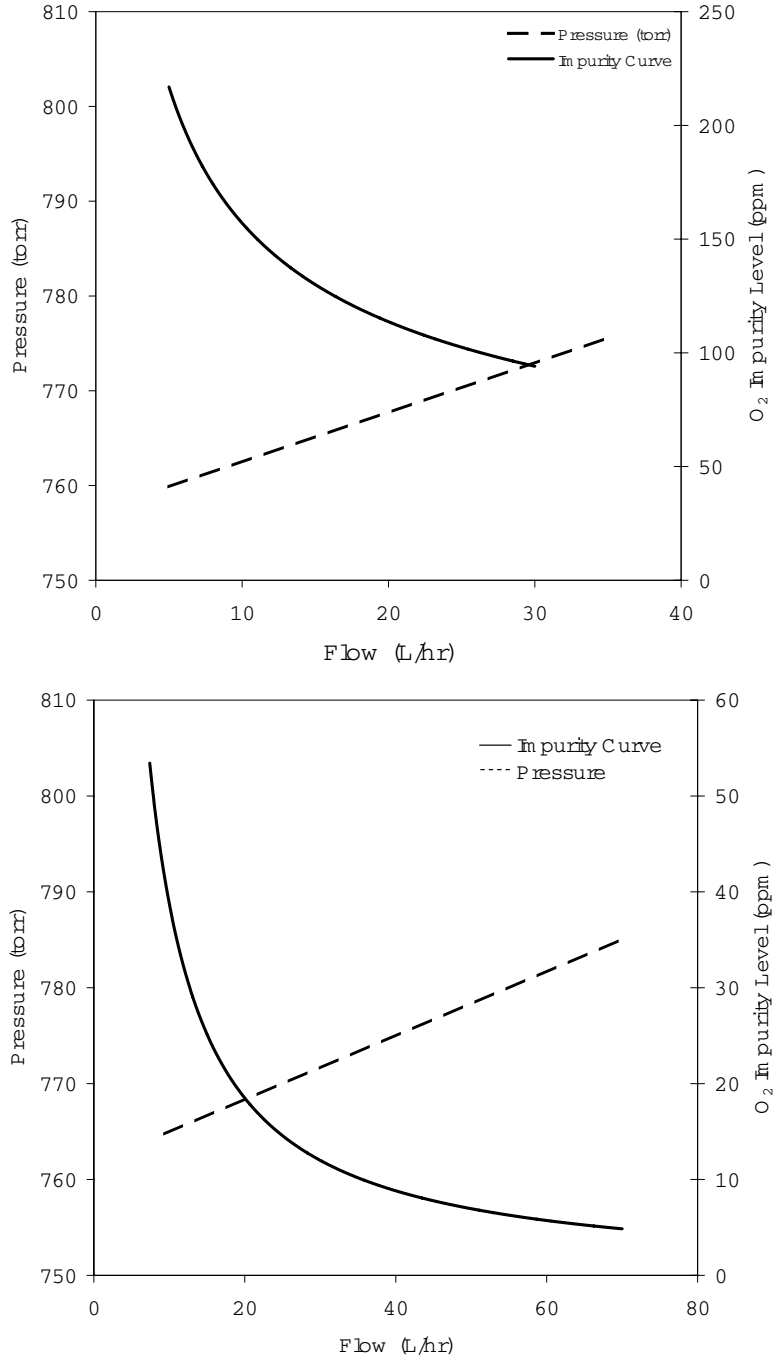

Figure 2.10: Impurity curves for the hadron monitor (top) and muon monitor (bottom) during tests where the gas flow rate was varied. As expected, impurity levels decrease with higher flows.

Chapter 3

Calibration of the Secondary Beam Monitors

3.1 Introduction

The purpose of the secondary beam monitors is to align the remnant hadron beam at the end of the decay pipe providing transverse spatial profiles of the hadron and muon beam downstream of the absorber, as well as providing relative measurements of secondary and tertiary beam intensities.

A 5% relative calibration of each chamber in the Hadron Monitor provides a beam centroid determination within 3cm, which corresponds to a 42 rad alignment of the beam [12]. The Muon Monitor requires a 1% relative calibration of its ion chambers. A 1% chamber-to-chamber calibration to of all three alcoves chambers is required to achieve a beam alignment of 100 μrads and to permit use of the relative pulse heights in each alcove as a coarse check of the beams energy spectrum [13].

This chapter will describe the procedure used to calibrate these detec-

tors, the relative scale factors derived, and checks performed to verify the integrity of the process. The central results are the relative scale factors in Tables 3.11 through 3.11.

3.2 Calibration

The relative calibration of each chamber in the muon and hadron monitors was achieved by mapping each chamber with a 1 Ci Am^{241} gamma source. The induced ionization current was compared from chamber to chamber after systematic effects such as source alignment with respect to each pixel or temporal variations such as gas pressure and temperature were factored out.

The hadron monitor could be tested within 8 hours, over which time systematic drifts or pressure changes in the gas were not significant. The 32 muon monitor tubes, having been constructed over a period of more than one year from Sep, 2003, to Dec, 2004, posed more significant challenges to calibrate: the 9 chambers within a tube could be calibrated within less than 8 hours, but the time between calibrations of consecutive tubes could be up to weeks.

The calibration apparatus had to control for systematic variations over such long periods. First, the gas system purged the chambers with pure gas and had instrumentation for measuring pressure, temperature, and impurity levels. Second, a control ion chamber, with its own internal calibration source, was mounted in series with the chambers being calibrated in the gas system; any temporal variations in the gas system would thus be observed in the control, or reference, chamber. Third, the electronics were re-calibrated for drift with each chamber to be calibrated.

3.2.1 Source

A 1 Ci ^{241}Am gamma source is used to irradiate each ion chamber in both the hadron monitor and muon monitors. ^{241}Am has a half-life of 433 years [26]. The source is housed in a steel capsule within a cylindrical lead pig for shielding. ^{241}Am emits an α particle to form an excited state of ^{237}Np which in turn emits a 60 keV γ as it deexcites. The α particles are captured in the steel capsule, and the gammas proceed through an aperture in the lead pig.

Beam scans were performed across a single muon monitor chamber to understand collimation of the source. As shown in Figure 3.1, a 1" diameter opening on the lead pig produces an uncollimated beam with a FWHM of about 8cm. Such a wide field of illumination is desirable, because in this case the source illuminates the entire 8×8 cm^2 sense pad of the ion chambers. The unfortunate trade-off is the increased sensitivity of our calibration results to accurate placement of the source near the ion chamber. A second scan was performed with a 1/4" collimator made of brass. In addition to producing less detectable signal in the muon monitor, the flat chamber response from 7 to 11cm for the collimated beam suggests that tightly-collimated source does not illuminate the entire sensitive area of the chamber. Since the chamber sense-pad is 7.6cm wide, the inferred width of the collimated beam is 1.8cm. Furthermore, the long tail of signal observed in the ion chamber even when the collimated source is placed 7 cm off-center suggests there is scattering of the low-energy gammas in the collimator brass. With these trade-offs in mind, we opted to use the wider 1" collimator opening, having to establish more stringent alignment of the source relative to the ion chambers for each of the calibrations.

Figure 3.2 shows the result of a fine-stepped scan of the 1 Ci source

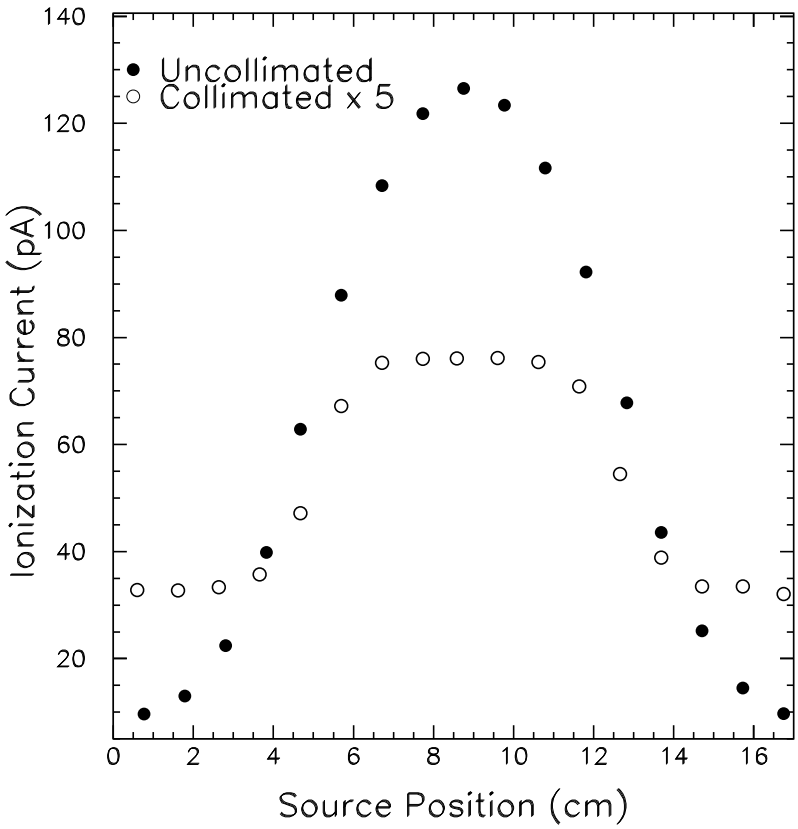

Figure 3.1: Beam scans with beam collimated to 1" and 1/4". Scan of the Am^{241} source across a chamber in a muon tube using identical source-chamber separation but two different collimator apertures. "Uncollimated" refers to a 1" diameter opening in the 1" thick source holder which fully exposes the 1" diameter source. "Collimated" refers to a plug inserted into this opening which has a 1/4" diameter aperture.

across two chambers in the Hadron Monitor. It is clear that the source illumination is never entirely contained within the ion chamber, since the ionization current never comes to a flat plateau. However, it may be seen that the current does not deviate by greater than one percent unless the source is misplaced from the chamber center by greater than 0.2 inches. The desire to calibrate our Hadron Monitor chambers to better than 1% over all thus suggested a design of a stand which aligns the source pig in front of each chamber to better than 1/8".

Figure 3.3 shows the result of a fine-stepped scan of the 1 Ci source across two chambers in the Muon Monitor tube 29. In the left graph, chamber 6 is scanned in the horizontal direction and the reference chamber is simultaneously read out to monitor stability. In the right graph, both chambers 1 and 9 are scanned vertically so as to check that the muon tube is level. A similar behaviour is observed as with the Hadron Monitor, namely that the source illumination is never completely contained in the ion chambers. However, it is similarly true that placing the source within 1/16" accuracy around the ion chamber center is sufficient to cause no worse than a 0.5% systematic uncertainty in the induced ionization current.

3.2.2 Electronics

Figure 3.4 shows a schematic of the readout of the chambers for the Muon and Hadron Monitor calibrations. The components of the electronics include:

- A Keithley 230 GPIB-controllable DC power supply provides a bias voltage to the ion chamber which is programmed to scan between -100 V and 100 V in 10 V increments with 10 mV precision[27].
- Eight Keithley model 480 and 485 picoammeters [27] were used to read

out the ionization current from the chambers being tested during the calibration scans. The picoammeters have resolution of order 0.1 pA, as is discussed below. Most produce an analog output voltage proportional to the measured ionization current, while two are GPIB-controllable and can be read back to the computer directly.

- A 16-bit Analog-to-Digital Converter converter 0-5 Volt input, Model TNG-1 by Mindtel, Inc.[28] which reads the analog outputs of the picoammeters. The least count of the ADC corresponds to approximately 0.08pA. The ADC is read into the computer over the serial bus.

- A custom NIM module with 8 channels of op amp circuits to invert the picoammeter outputs and scale them to 0-5 V before they are fed in to the ADC.

The eight picoammeters were individually calibrated by applying -10 to 10 mV across a resistor measured to be 100.04 MΩ . The voltage was supplied from the Keithley 230 supply, which has 10 μV precision when used in its $\pm$100 mV range. The results of the calibrations are shown in Figure 3.5. All picoammeters are shown to be linear with input current with residuals on the order of 0.1 pA. There is more variability in the slope of the picoammeters read out by the ADC due to variations in the resistors and operational amplifiers used in the NIM module for amplification of the picoammeter analog outputs.

Nominally, the picoammeters' digital display is significant to 1 pA, but we found that the analog voltage output provides measurement precision to 0.1 pA. The reason for the 1 pA display appears to be that the picoammeters experience drift of up to 0.07pA/hr. This drift is empirically found to be acceptably small over the $\sim$30 minutes of an ion chamber calibration in order to exploit the potential 0.1 pA resolution of the picoammeters: as shown in

Figure 4.6, a voltage bias curve taken of either a hadron or muon monitor chamber shows the characteristic rise to ionization current plateau by ∼10 V, and the plateau is steady to far better than 1 pA. Such voltage bias curves require approximately 30 minutes to acquire, which sets the scale for the duration over which the picoammeters are stable. As can be seen in Figure 3.7, however, over periods of several hours the picoammeter output does experience drift of order 2 pA: in this figure, bias voltage scans are made for a single muon ion chamber which is illuminated by only its 1 μCi α source. The ionization current on plateau should be constant, but varies by a couple picoamps over the 40 hour period.

To combat the effect of the picoammeter drift, we ramped the ion chamber bias voltages from -100 to $+100$ Volts for every ion chamber that we measured. In this way, a plateau value for the ionization current is measured for both the positive and negative voltage polarity. In principle, these values should be the same, and the extent to which they differ in absolute value is a measure of the drift in the picoammeter circuit. We define

$$I_{\text{plateau}} = \tfrac{1}{2}(I_+ - I_-)$$
$$I_{\text{offset}} = \tfrac{1}{2}(I_+ + I_-)$$

where I_+ is the average of the ionization currents measured for all bias voltages above 20 V and I_- is the average of the ionization currents measured for all bias voltages below -20 V (which as shown in Figure 4.6 has the opposite sign as I_+ due to the collection of electrons at the signal plate as opposed to the collection of ions in the case of I_+). The quantity I_{plateau} is a measure of the plateau ionization current that is less sensitive to picoammeter drift than just taking I_+ alone, while the quantity I_{offset} is a useful measure of the picoammeters' drift. Figure 3.8 shows the quantities I_{plateau} and I_{offset} as

a function of time during the 40 hours of repeated voltage bias curves from Figure 3.7. The quantity I_{plateau} is stable to ± 0.2 pA.

During the same 40 hour period, the offset and plateau ionization current were read out for a muon monitor chamber exposed to the 1 Ci source. This data is shown in Figure 3.9. Like the chamber reading out only the 1 μCi source, the offset drifts by about 2 pA and the plateau ionization current I_{plateau} is constant to ± 0.2 pA.

In Figure 3.10 we show a separate study of the repeatability of the ionization current measurement which tests both the stability of the electronics and also the repeatability of the placement of the 1 Ci source in front of a chamber. In this study, the 1 Ci source is moved back and forth between chambers 6 and 7 within a single muon tube. At each placement of the 1 Ci source, the plateau ion current I_{plateau} is read out of both chambers. The irradiated chamber reads approximately 124 pA, while the non-irradiated chamber sees the few picoamps from its internal calibration source. For both chambers, the repeatability of these measurements is approximately 0.25pA, irrespective of whether the signal is 5 pA or 124 pA.

3.2.3 Gas System

Ambient temperature is constantly recorded by the Applied Data Sciences Weather Logger which is sensitive to 1° F changes[29]. Pressures are monitored by an MKS 750B pressure transducer installed directly upstream of the detector[24]. It is sensitive to 0.1 torr variations.

A reference chamber is installed downstream of the Hadron/Muon Monitor in the same gasline as the detector. It serves as an additional monitor of temperature and pressure variations. It is a single, 3mm gap chamber in a

stainless steel vessel. It's gas volume is illuminated by 40 1μCi α sources to provide a standard signal. These sources are specifically lining the walls of the vessel, so there is about a .5" distance between the sources and the chamber gap. The reference chamber is shown to be sensitive to fluctuations in pressures, temperatures, and provides a measure of the accuracy of our corrections.

The muon monitors were calibrated over a period of approximately 1 year. During that time, pressures varied by as much as 10 torr, and temperatures varied up to 20 degrees. Since the measured plateau current of a given chamber varies with these quantities, it is desirable to correct for such variations via

$$I^{\text{corr}}_{\text{plateau}} = I^{\text{raw}}_{\text{plateau}} \times [1 + A(T - T_{\text{nominal}})] \times [1 + B(P - P_{\text{nominal}})]$$

where $I^{\text{raw}}_{\text{plateau}}$ ($I^{\text{corr}}_{\text{plateau}}$) refer to the raw (corrected) plateau ionization currents, P and T refer to absolute pressure in Torr and to temperature in °F, and $T_{\text{nominal}} = 75°\text{F}$ and $P_{\text{nominal}} = 790$ Torr refer to nominal pressure and temperature conditions.

We derive the constants A and B above from Figure 3.11 and Figure 3.12. These show the ionization current of an individual muon chamber and the reference chamber as a function of pressure or temperature in N_2 and He gases. Pressure was varied by adjusting a metering valve downstream of the reference chamber while maintaining constant flow. Ionization currents were read out from the reference chamber and the chamber irradiated by the 1 Ci source. In nitrogen, the ion chambers and reference chamber show opposite trends. As the density of the gas increases with pressure, there are two competing effects at work: there is greater ionization in the chamber gap, but there is also a greater probability of radiation interacting before it enters the

gap. For the irradiated chamber, the former effect dominates. For the reference chamber, more alpha's range out with increased nitrogen density before reaching the chamber volume, therefore producing less ionization in the chamber gap. In Helium, the reference chamber actually shows both these effects as the pressure is increased beyond 770 Torr.

Temperature scans were also performed, and these are illustrated in Figure 3.12. During these scans, the ambient temperature was varied by 6-10 °F adiabatically over a period of 24 hours. The reference chamber again shows an opposite trend to that of the irradiated chamber, as lower temperature gas causes alpha's to range out before entering the chamber gap.

The derived pressure and temperature constants A and B are summarized in Table 3.1.

As a test of these temperature and pressure corrections, we studied the ionization current from the reference over the course of the 400 days of calibrations. Figures 3.13 and 3.14 show the ionization current measurements of the reference chamber obtained during the 400 days muon chamber calibrations. Shown are the temperature and pressure during thistime, as well as the signal from the reference chamber, before and after corrections. As shown in Figure 3.14, the calibrations leave a spread of only 0.6 pA out of a signal of 100 pA. Thus the reference chamber can be calibrated to better than 1%. Furthermore, because the reference chamber is five times more sensitive to pressure and temperature variations than the actual Muon and Hadron Monitor ion chambers, we conclude that the gas monitoring system satisfactorily controls for such variations.

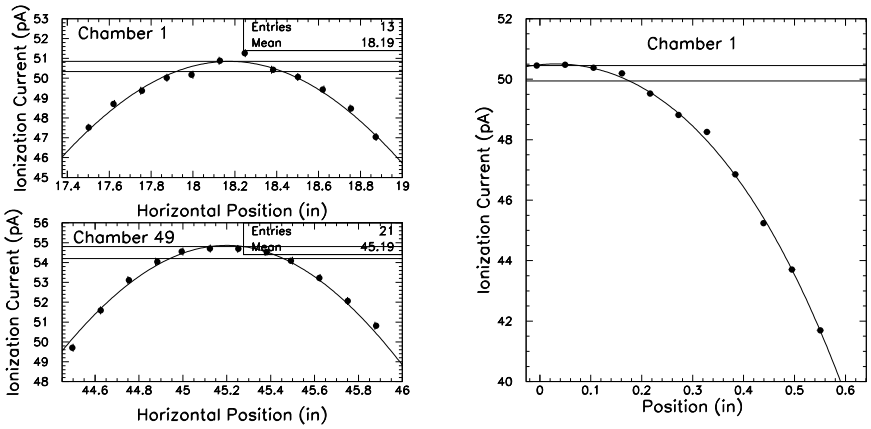

Figure 3.2: A fine scan of chamber 1 in the hadron monitor in the horizontal (left) and vertical (right) directions. The curves are polynomial fits to the data. The horizontal lines are drawn at the maximum ion current and at a value 1% below this maximum, indicating that the source must be placed within ±0.2" to maintain a constant illumination at the 1% level.

Pressure Scans	He		N_2	
	Nominal Signal (pA)	Slope (%/torr)	Nominal Signal (pA)	Slope (%/torr)
Irradiated	34.5	0.10	125	0.09
Non-Irradiated	2-3	0.17	4-8	-0.055
Reference	95	0.15	101	-0.46
Temperature Scans	He_2		N_2	
	Nominal Signal (pA)	Slope (%/torr)	Nominal Signal (pA)	Slope (%/torr)
Irradiated	27.4	0.35	124.5	-0.076
Non-Irradiated	3-5	1.3	6-8	-.27
Reference	85.8	-0.230	108	0.67

Table 3.1: Variations of plateau height with pressure and temperature in He_2 and N_2 gas.

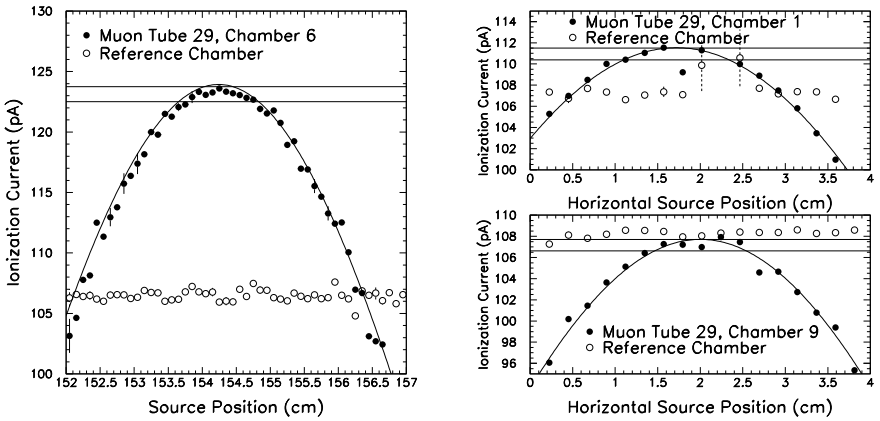

Figure 3.3: (left) Fine scan in the horizontal direction of chamber 6 of muon tube 29. (right) Fine scan in the vertical direction of chambers 1 and 9 of muon tube 29. The curves are polynomial fits to the data. The horizontal lines are drawn at the maximum ion current and at a value 1% below this maximum, indicating that the source must be placed within ±0.2" to maintain a constant illumination at the 1% level.

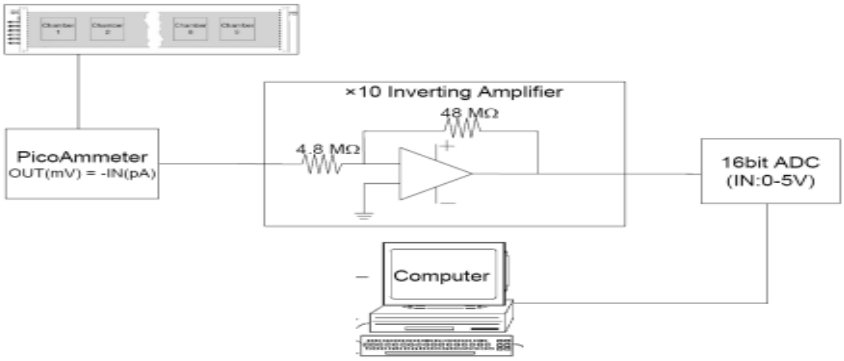

Figure 3.4: Schematic of the ionization chamber readout.

3.3 Calibration Test Stands

3.3.1 Hadron Monitor

Figure 3.15 shows the test stand with the hadron monitor sitting on a horizontal beam mounted to vertical I-beams. Leveling mounts allow for precise alignment of the horizontal beam. The vertical beams are bolted to a wall and aligned with bubble levelers. The radiation source is supported by a second horizontal I-beam mounted on the vertical bars. The source support rail can be be positioned to align the source with each row of pixels in the Hadron Monitor. A moveable cart allows for an abitrary lateral positioning of the source pig. A tape measure is inlaid between the rails and bolted to the source bar to provide a means for consistent source placement.

Transverse scans of the detector were performed to confirm alignment of the test stand and to map out chamber centers. The source was placed at the far end of the source bar, and signals were recorded from all 7 chambers as the source was moved in 1/2" increments across the detecter. Figure 3.16 shows

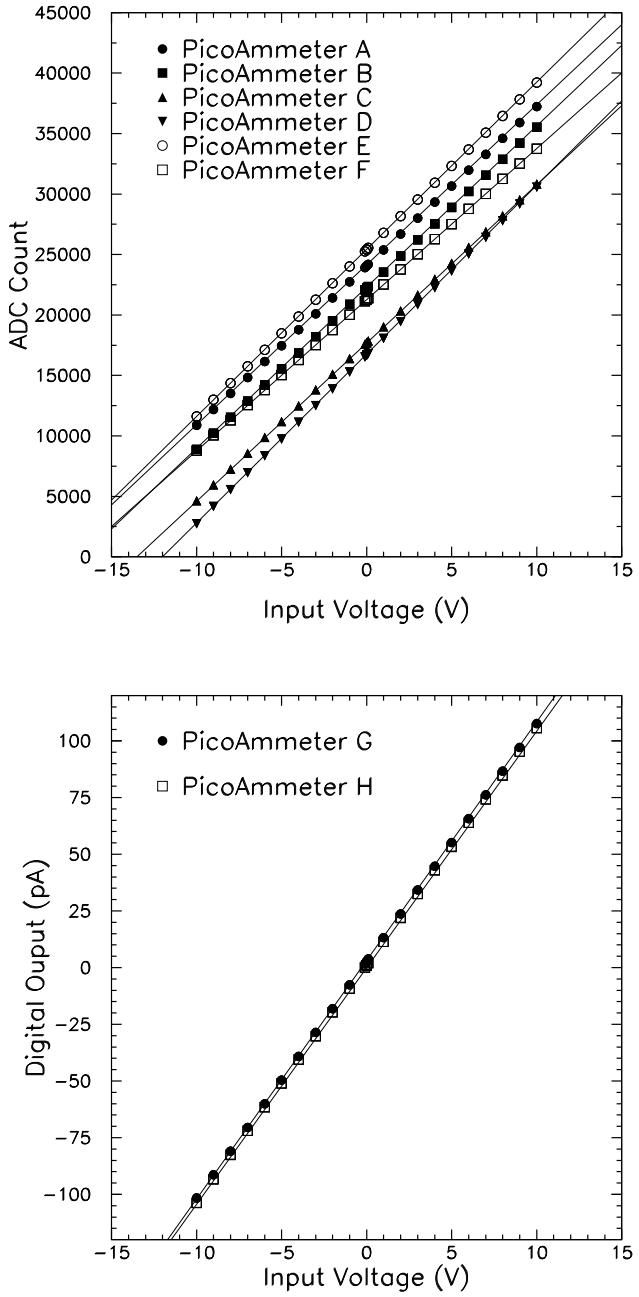

Figure 3.5: Calibration of the Keithley picoammeters. Six picoammeters were readout from their analog outputs through an ADC(top). Two picoammeters had digital outputs that were recorded directly (bottom).

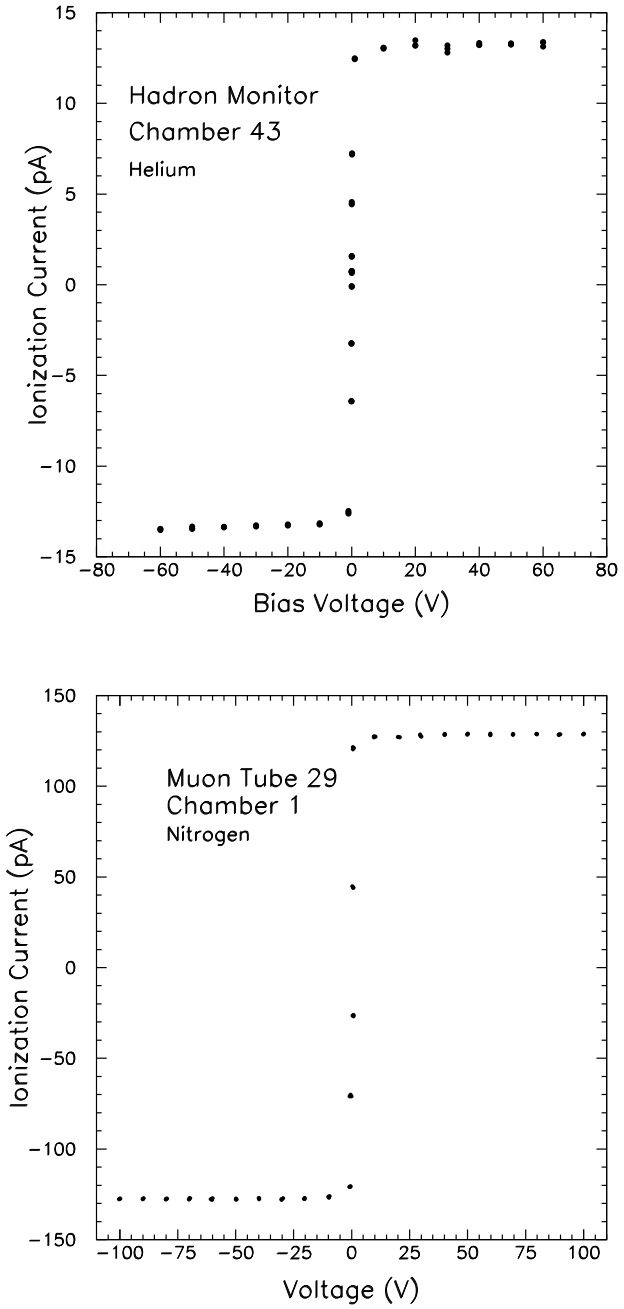

Figure 3.6: Voltage bias curves for a single ion chamber in the Hadron Monitor (top) and a Muon Monitor tube (bottom).

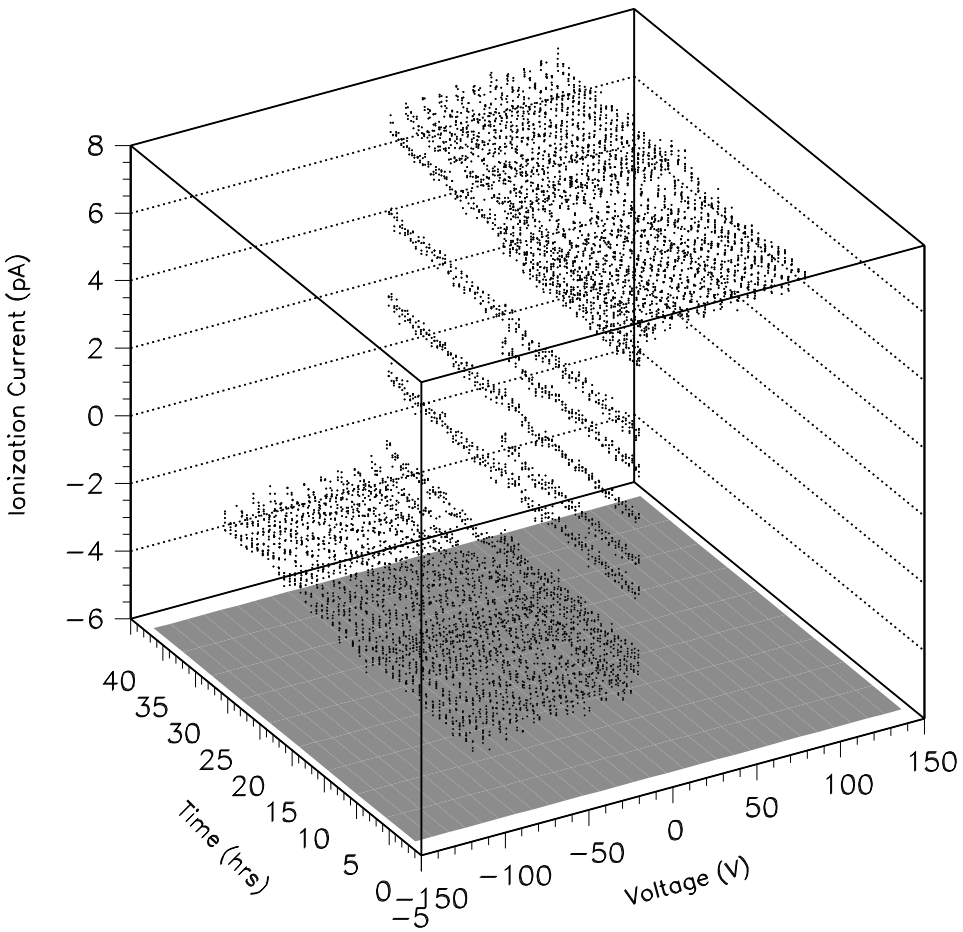

Figure 3.7: Repeated plateau curves obtained over a 40 hour period. The ionization current is read at several voltages from -100 V to 100 V, and the voltage sweep is subsequently repeated.

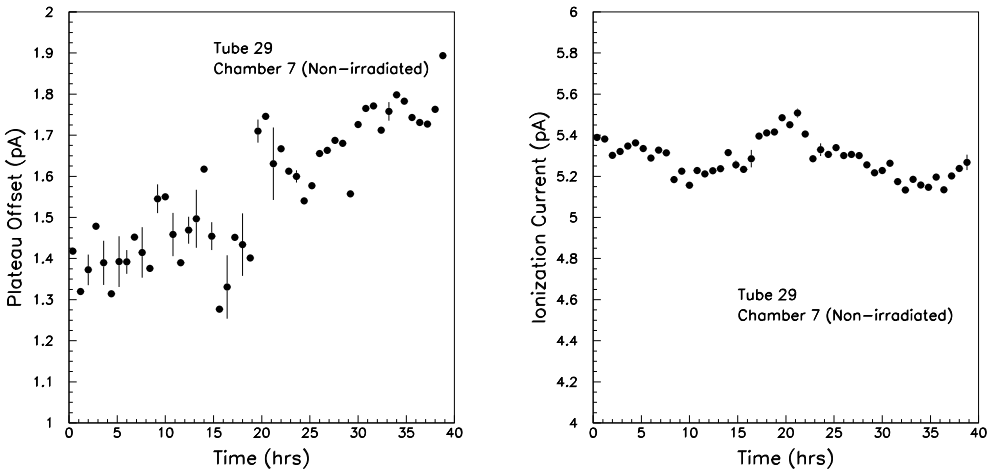

Figure 3.8: (left) Plateau curve DC offset I_{offset} over the duration of the repeatability study. (right) Derived plateau ionization current I_{plateau} over the duration of the repeatability study.

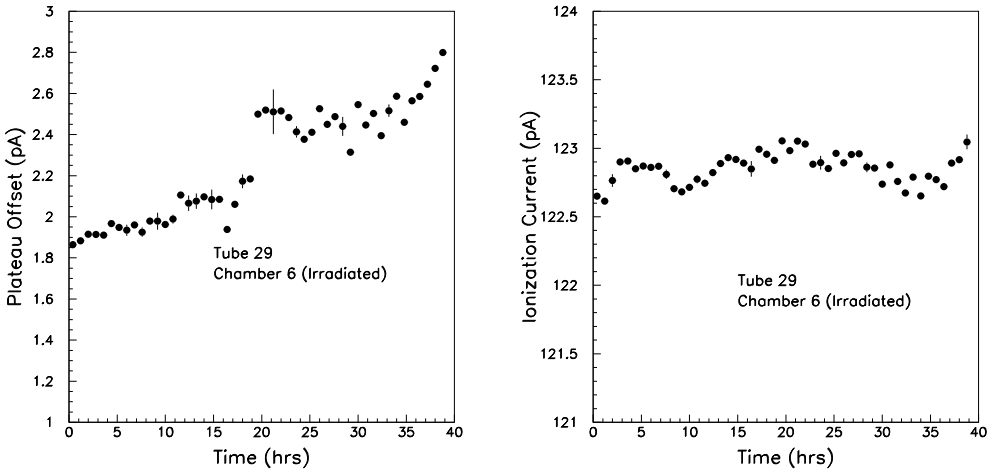

Figure 3.9: Offset and plateau ionization current for chamber 6 of a muon tube which is exposed to the 1 Ci source. The data come from the the same 40 hour period as the data for the un-irradiated chamber from Figure 3.8.

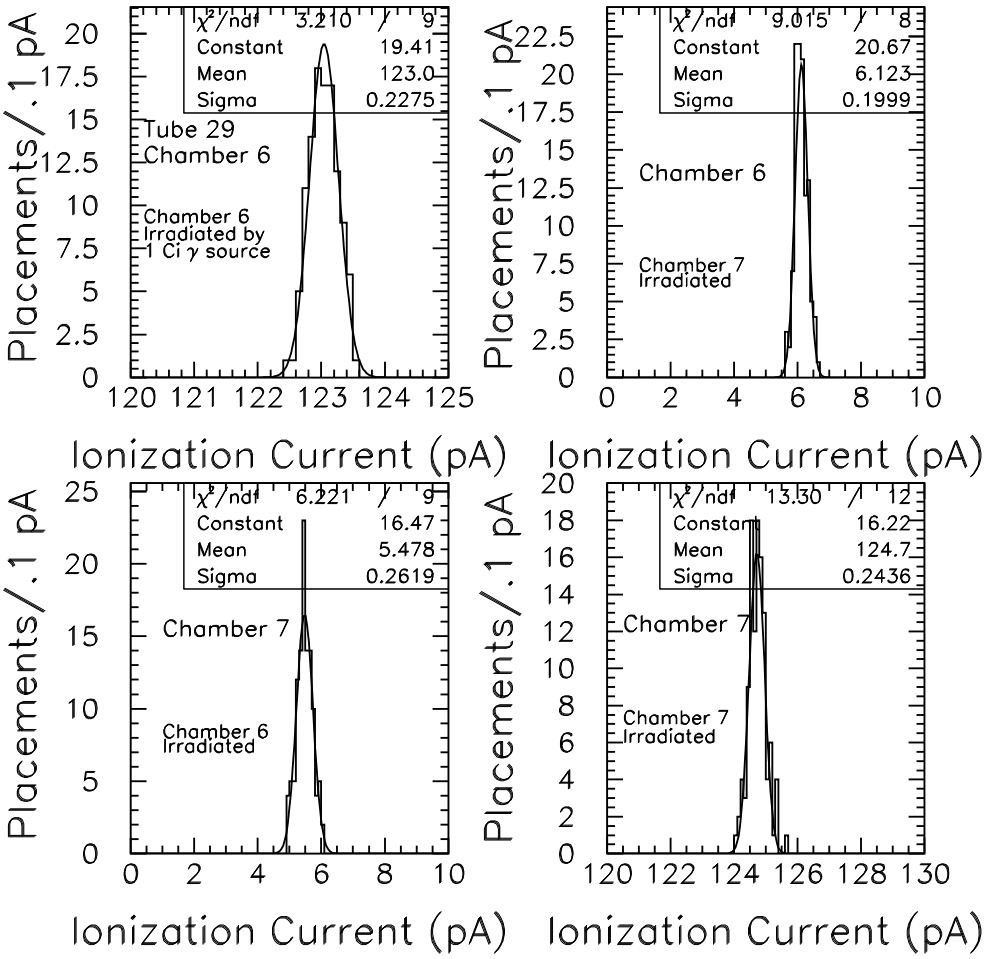

Figure 3.10: Histograms of the repeated plateau height measurements from chambers six and seven as the source placement is alternated.

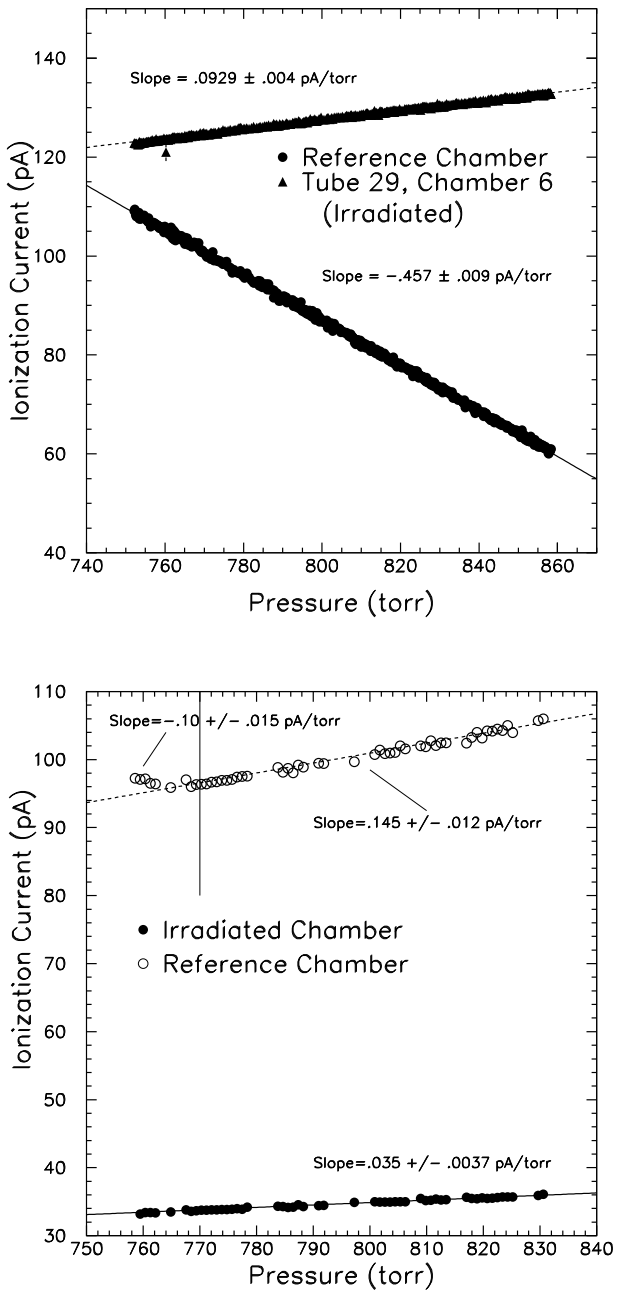

Figure 3.11: Change in response of the ionization current in variation with pressure in N_2 (top) and He (bottom) gas.

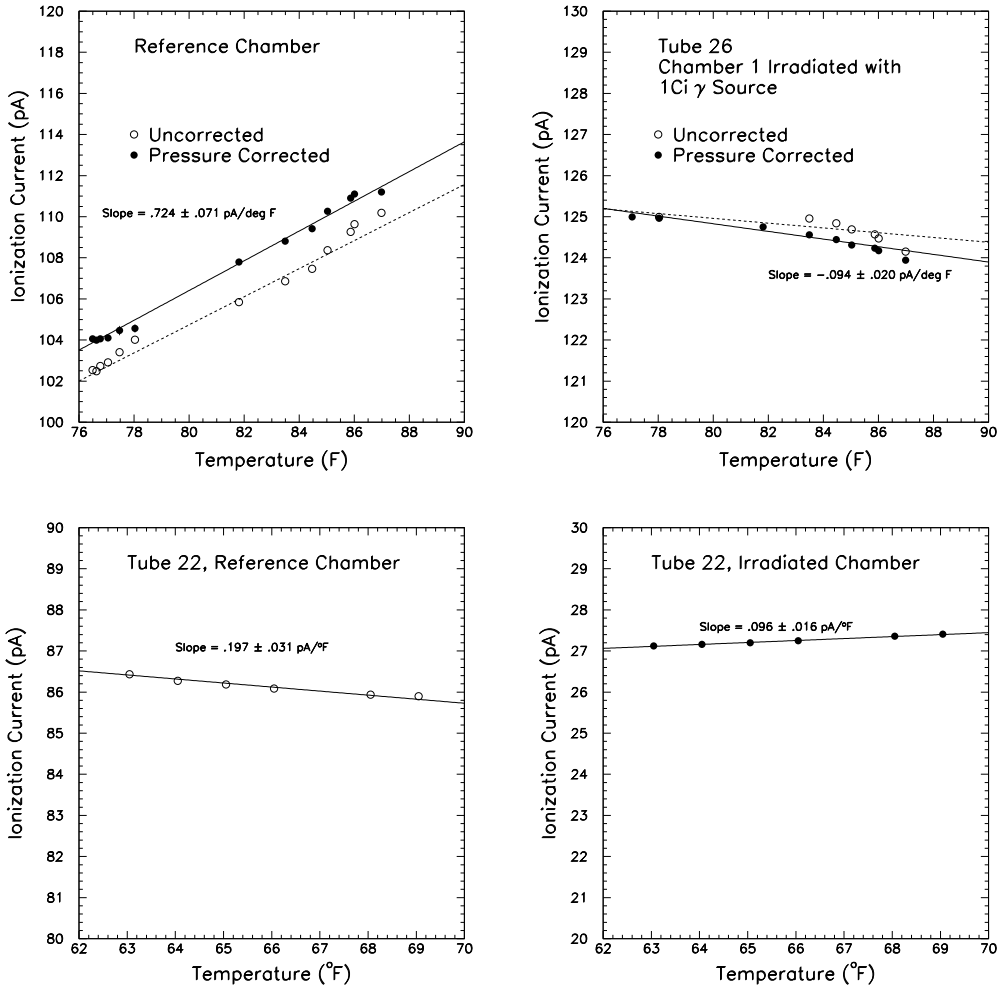

Figure 3.12: Temperature scans of muon chambers in N_2 (top row) and He (bottom row) gas Shown are the ionization currents in the reference chamber (left column) and a muon tube ion chamber illuminated by the 1 Ci source (right column).

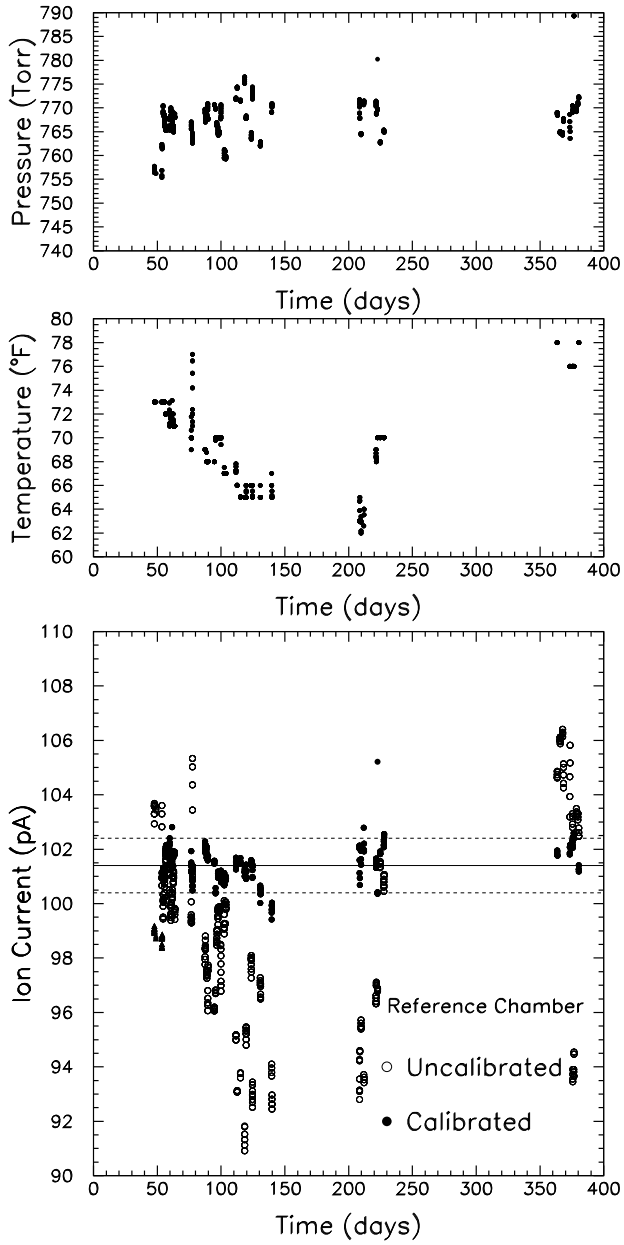

Figure 3.13: Graph of absolute pressure (top) and of temperature (middle) for the reference chamber over the 400 days of calibration operations. (bottom) The ionization current in the reference chamber without and with the corrections for pressure and temperature variations.

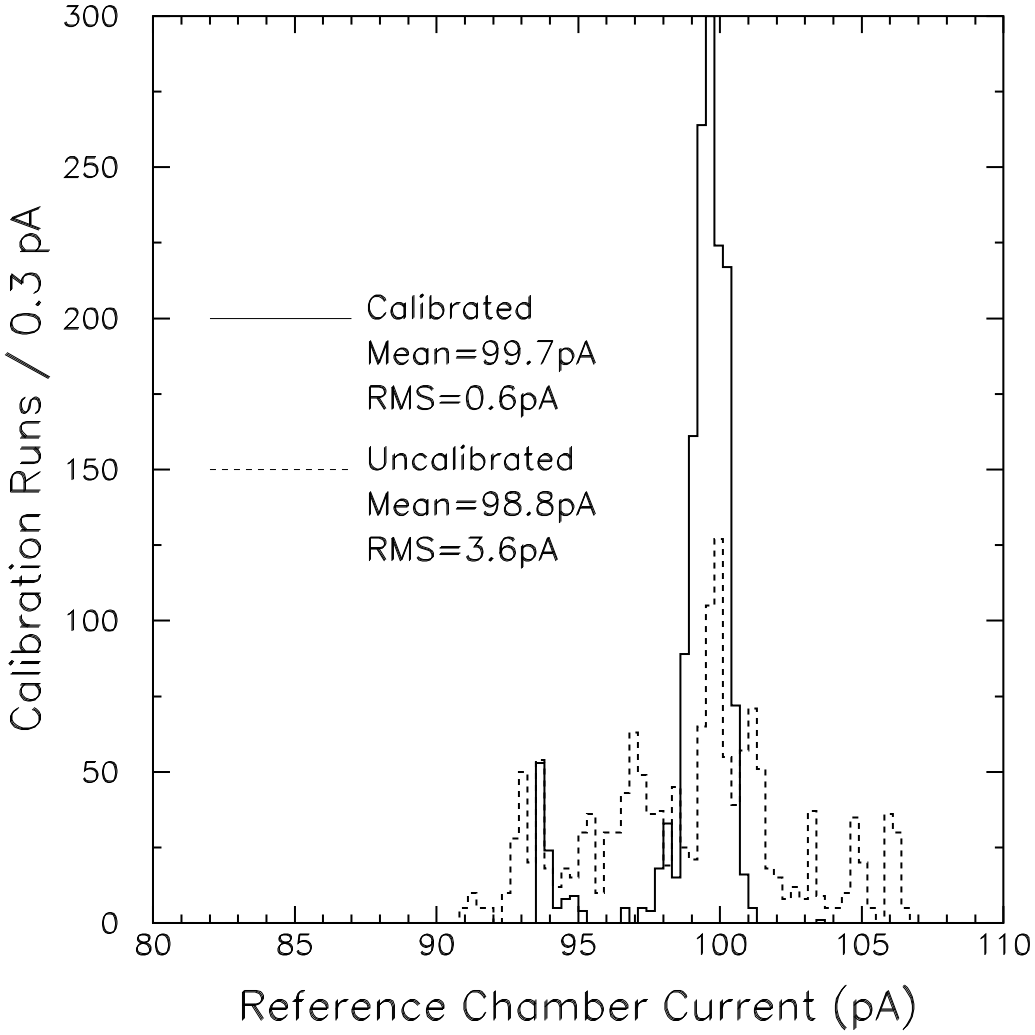

Figure 3.14: Histogram of reference chamber currents for every muon chamber calibration. The raw and calibrated distributions are shown.

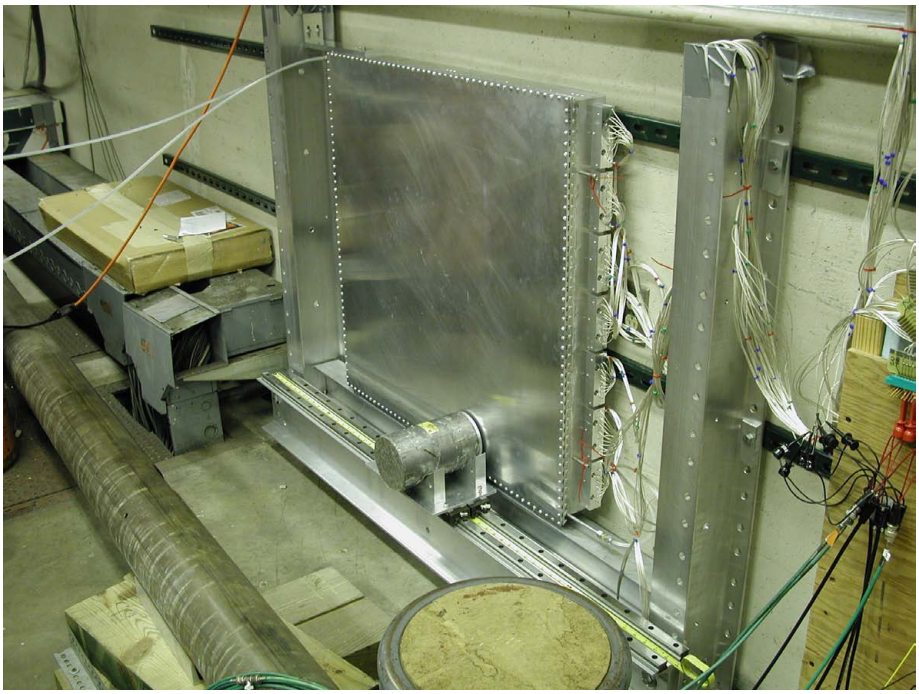

Figure 3.15: Hadron Monitor test stand.

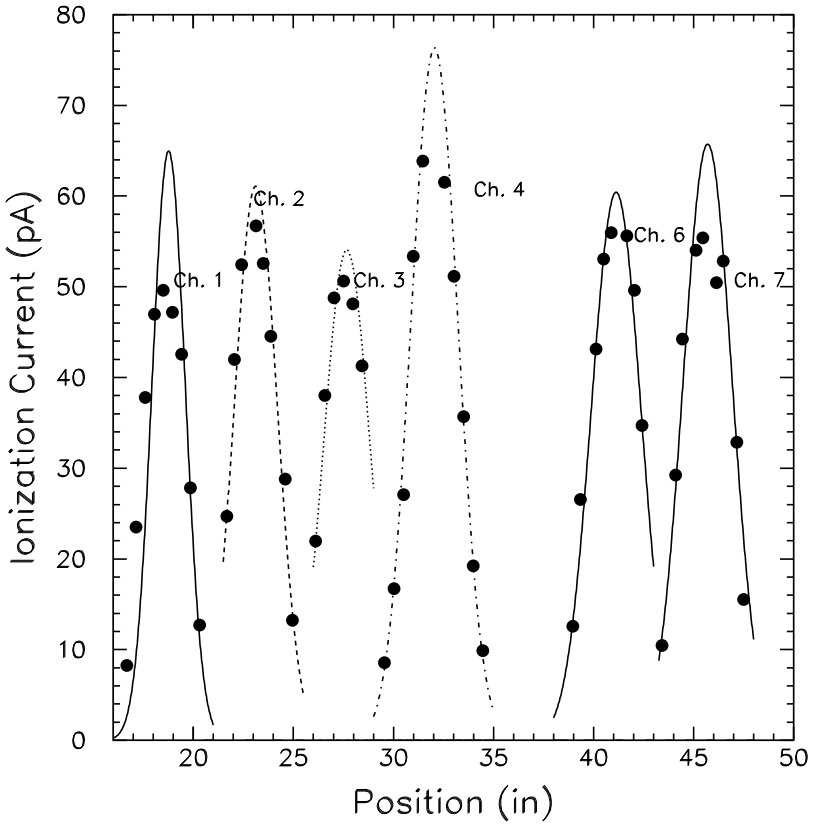

Figure 3.16: A coarse transverse scan of one row of the hadron monitor(chamber 5 not shown).

a coarse transverse scan across row 1. The fits indicate the chamber centers are evenly spaced by 4.5" as designed. It also indicates the beam half-width from the radiation source is about 1.5". Since the sense pad of a chamber plate is 3" $\times$ 3", we illuminate the entire sensitive region of the chamber gap. Figure 3.2 shows a finer horizontal scan of chamber 1 and chamber 49 in 1/8" increments.

3.3.2 Muon Monitor

Figure 3.17 shows the test stand constructed to perform the muon tube calibrations. The tube is fixed to two vertical struts bolted to the surface of a lab table. A rail is also bolted to the table in front of the tube to guide a movable cart that supports the radiation source. The cart is machined to provide accurate vertical positioning of the pig. Signal output and HV lines are accessible at the endplate.

As in the case of the hadron monitor, scans were conducted to confirm alignment and map out chamber centers. Figure 3.18 shows a coarse transverse scan of a muon tube. The centroids are shown to be spaced by 10" as expected by design. A finer scan of chamber 6 was shown in Figure 3.3.

3.4 Calibration Analysis

3.4.1 Hadron Monitor

The hadron was calibrated over a period of 7 days. Each chamber response to the 1 Ci ^{241}Am gamma source was measured according to the procedure described above, and the calibration was repeated several times to check for consistency. Since the Hadron Monitor is a small, single vessel, each calibration

run required approximately 5 hours.

A series of three full scans were performed in which all 49 chambers were tested. Additionally, two partial scans were performed to repeate measurements on one or two rows only. Table 3.2 summarizes the results of these calibration scans. Each of the 49 rows of the table is the data from one of the chambers. One full calibration run was performed in air, one in pure Helium, and one was taken while the chamber was being purged.

The ionization currents from every chamber have been divided by the current from chamber 25 (the middle pixel) within a given run. This scaling corrects for pressure or temperature changes that occurred in between calibration runs (again, assuming that the pressure change within a calibration run was small).

In the scan labeled HeCal2, it was noticed after the fact that the purity level dropped over 45 ppm during the test due to initial purging of the Hadron Monitor with He gas. This dropping impurity level changed the chambers response. In a separate test, the ionization current of chamber 49 was measured as a function of varying purity. The result is shown in Figure 3.19. A variation of 45 ppm is shown to correspond to an ionization current correction of up to .25 pA. We therefore use the trend of Figure 3.19 to correct the calibration run HeCal2. Table 3.2 shows both the uncorrected and corrected measurements for the HeCal2 scan.

The values within a given row of Table 4 should be identical if the calibration runs were perfect. Fluctuations within a row result from measurement uncertainties in the calibration (source placement, pressure variation, electronics noise). We plot the deviations of the normalized plateau height from nominal are shown in Figure 3.20. Nominal refers to the chamber values obtained from the scan labeled HeCal4. The halfwidth of Figure 3.20 is 1.2%,

Chamber	HeCal1 air/He mix >285ppm	HeCal2 215-170 ppm	HeCal2 Corrected	HeCal3 170 ppm	HeCal4 90-90.5 ppm	HeCal5 90-90.5 ppm	Scale Factors
1	0.88	0.93	0.92		0.89	0.89	1.13
2	0.93	0.97	0.96		0.95	0.94	1.05
3	0.88	0.90	0.90		0.89	0.89	1.13
4	1.03	1.03	1.03		1.02	1.02	0.98
5	0.92	0.94	0.94		0.94	0.94	1.06
6	0.88	0.89	0.89		0.90	0.91	1.11
7	0.95	0.96	0.95		0.96	0.97	1.04
8	1.02	1.01	1.01		0.99	1.00	1.01
9	0.97	1.07	1.07		1.05	1.06	0.95
10	0.97	0.99	0.99		0.99	0.99	1.01
11	0.95	0.96	0.96		0.96	0.96	1.04
12	0.94	0.95	0.95		0.96	0.96	1.04
13	0.85	0.85	0.85		0.86	0.86	1.17
14	0.98	0.98	0.98		0.99	1.00	1.01
15	0.96	0.98	0.98		0.99		1.01
16	0.89	0.91	0.91		0.91		1.10
17	0.84	0.86	0.86		0.86		1.16
18	0.93	0.93	0.93		0.93		1.07
19	1.04	1.00	1.00		1.05		0.96
20	0.90	0.89	0.89		0.86		1.16
21	0.90	0.91	0.91		0.93		1.07
22	0.95	0.96	0.96		0.96		1.04
23	0.92	0.92	0.92		0.92		1.08
24	0.94	0.94	0.94		0.94		1.07
25	1.00	1.00	1.00		1.00		1.00
26	0.94	0.93	0.93		0.93		1.08
27	0.91	0.91	0.91		0.91		1.09
28	0.98	0.99	0.99		0.99		1.01
29	0.91	0.91	0.91		0.92		1.08
30	0.93	0.93	0.93		0.94		1.06
31	1.03	1.03	1.03		1.03		0.97
32	0.98	0.98	0.98		0.98		1.02
33	0.95	0.98	0.98		0.97		1.03
34	0.93	0.95	0.95		0.96		1.04
35	0.91	0.91	0.91		0.91		1.09
36	0.98	0.97	0.97		0.98		1.02
37	0.96	0.95	0.95		0.97		1.04
38	0.93	0.91	0.91		0.94		1.07
39	0.93	0.94	0.94		0.95		1.05
40	1.01	1.00	1.00		1.02		0.98
41	1.07	1.07	1.07		1.08		0.92
42	0.93	0.98	0.98		0.94		1.07
43	1.06	1.04	1.04	1.06	1.07		0.94
44	0.95	0.94	0.94	0.94	0.95		1.06
45	0.92	0.90	0.90	0.92	0.93		1.08
46	1.03	1.02	1.02	1.02	1.02		0.98
47	0.91	0.91	0.91	0.92	0.93		1.07
48	0.84	0.85	0.85	0.85	0.86		1.16
49	0.96	0.96	0.96	0.97	0.98		1.03

Table 3.2: Table of normalized plateau signals in the Hadron monitor ion chambers for 5 sets of measurements and the scalefactors

with only 2 outliers ranging beyond 5%. The outliers are measurements from two different chambers and can be attributed to incorrect source placement for those particular plateau height measurements. Thus, we conclude that the individual chamber response of every pixel in the hadron monitor is understood relatively to better than 2%.

3.4.2 Muon Monitor

The muon monitor ion chambers were tested in N2 gas, which offers us larger signal and hence better calibration sensitivity relative to a He medium. We also tested a couple of muon chambers in He to confirm that the choice of gas introduces no bias in the relative calibration.

The muon monitor calibrations are somewhat more complicated because of the large number of muon monitor chambers in comparison to the hadron monitor, and because of the long duration of construction and calibration of the muon monitors which led to potential temporal systematics such as electronics drifts or pressure and temperature changes. As discussed in Section 3.2.3, correction factors were derived for gas pressure and temperature variation which should maintain a relative calibration of individual chambers within the array to within 1%. Table 3.3 summarizes our expectation for all the systematic uncertainties in the relative calibration factors.

These correction procedures were demonstrated to work well on the reference chamber, which is more sensitive to such variations than are the muon chambers being calibrated. Figures 3.13 and 3.14 showed that the reference chamber signal, which could vary by 20% over the course of the 400 days of muon chamber testing, could be brought to 0.6% consistency, in agreement with the expectation in Table 3.3.

It was impractical to repeat the muon chamber calibrations for multiple iterations, as was done for the hadron monitor. However, we did test tube 26 at five different conditions spread out in time over the duration of the 400 days. The data is tabulated in Table 3.4. Listed are the pressures and temperatures of each test, in addition to the measured currents of the chamber being irradiated by the 1 Ci source, currents from each chamber when it is not being irradiated by the 1 Ci source (ie: is exposed only to its internal 1 Ci Am241 source), and reference chamber currents. Pressures varied over 20 torr, and temperatures ranged from 72°F to 78°F. The bottom two rows of each table offer a measure of the percent correspondence between different chambers and different tests before and after pressure and temperature corrections. Two conclusions are drawn: 1) the multiple tests provide a 1% agreement for any given chamber, and 2) the chambers all scale the same way with pressure and temperature, so that the relative calibration maintains its integrity. The spread in the plateau current values for a given chamber include variations due to source placement and readout, so the 1% agreement is inclusive of all of our sources of error.

Tables 3.5- 3.11 show the irradiated plateau measurement and the non-irradiated plateau measurement for all muon chambers. The irradiated current of Tube 26, chamber 1, is scaled to one, and scale factors are derived for all chambers by the same normalization. The chambers are labeled by alcove and channel number, with channels corresponding to the conventions given in Section 1.4. Also given are the corresponding tube and chamber numbers.

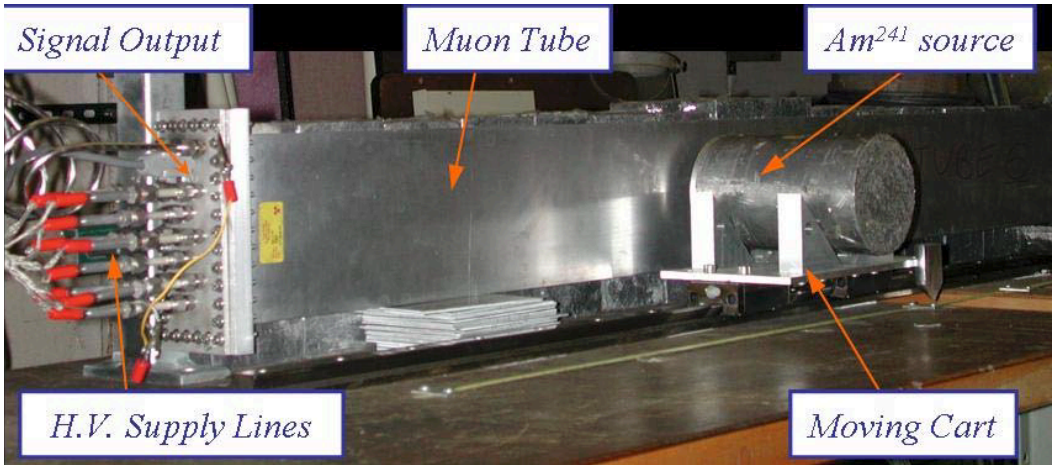

Figure 3.17: Muon monitor test stand.

Table of Errors	Muon Chamber N_2	Muon Chamber He	Reference Chamber N_2	Reference Chamber He
Electronics	.1%	.1%	.2%	.2%
Source Placement	.8%	.8%	–	–
Pressure Correction	.05%	.1%	.1%	.15%
Temperature Correction	.1%	.3%	.3%	.2%
Total Uncertainty	.9%	1.0%	.5%	.5%

Table 3.3: The contributions to the uncertainty of the plateau measurement for the Muon Monitor chambers being calibrated and for the Reference Chamber being measured in parallel.

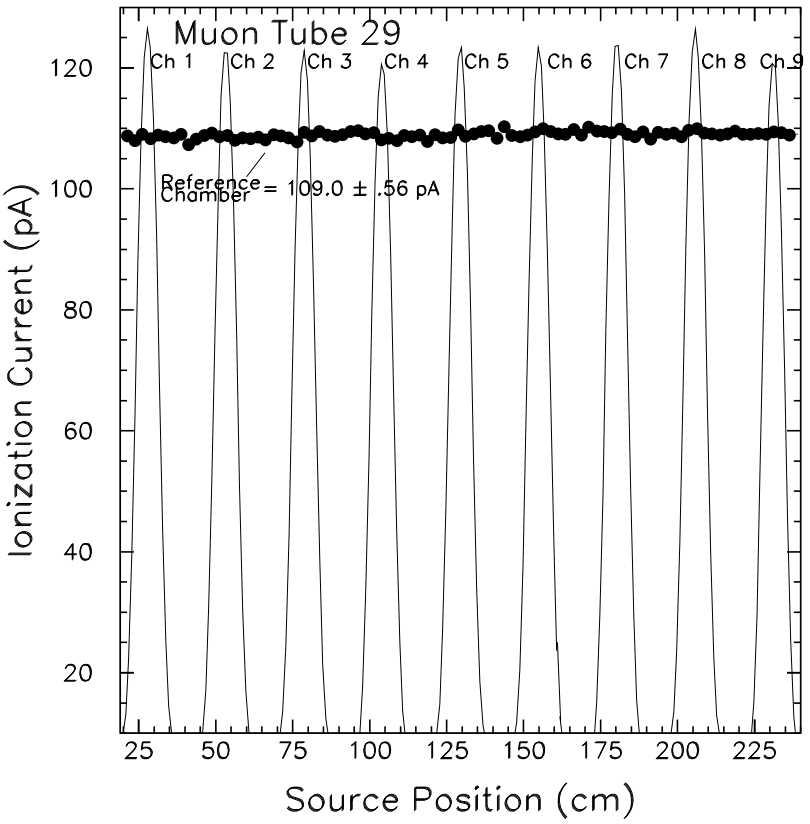

Figure 3.18: Coarse transverse scan of the muon monitor.

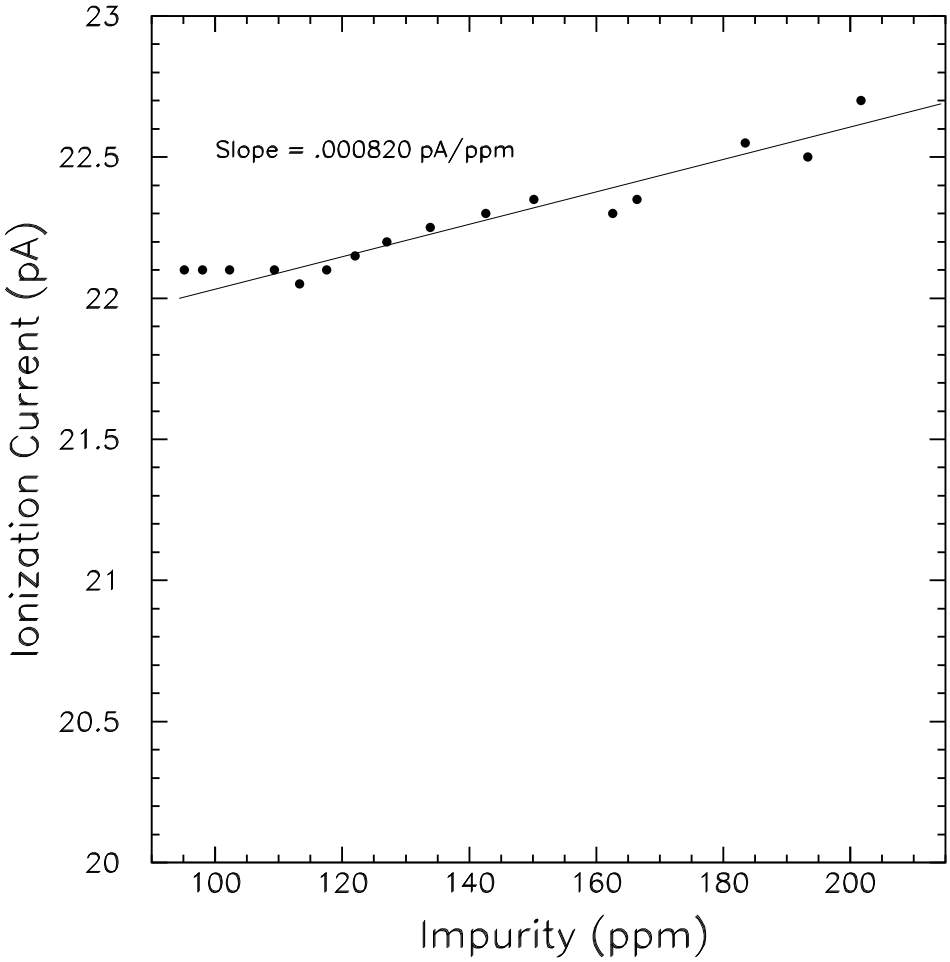

Figure 3.19: Ionization Current in the Hadron Monitor as a function of Impurity.

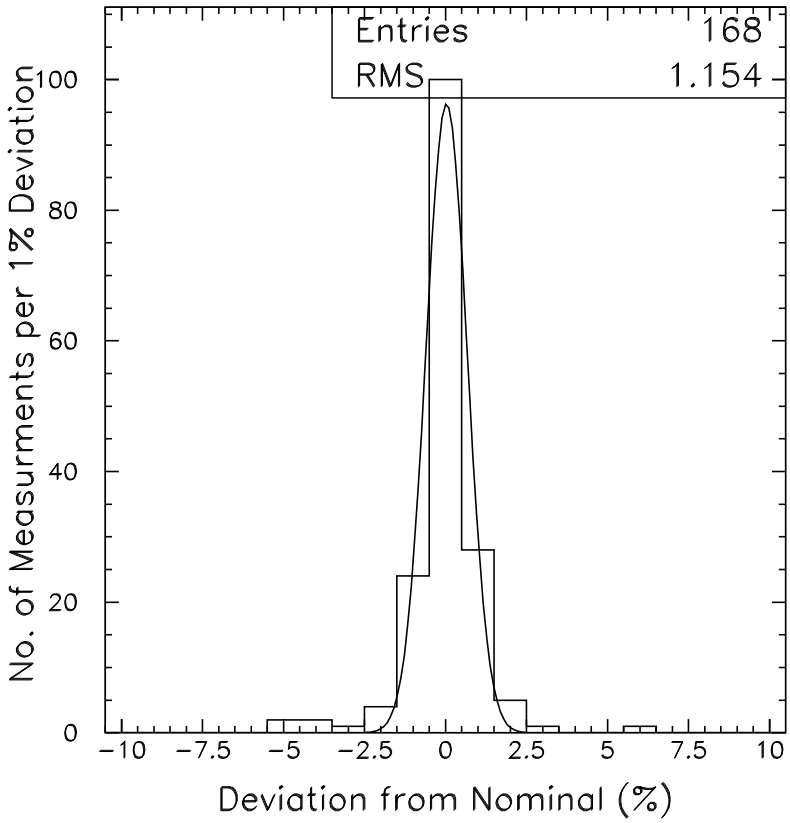

Figure 3.20: Histogram of the percent deviations of every ion chamber plateau height measurement from the corresponding 'nominal' measurement, where 'nominal' refers to the values of HeCal4 in Figure 3.2.

	Pres	Temp	Gas	Irrad	Non-irrad	Ref Ch.	Irrad corr to "Nominal"	Ref corr to "Nominal"	Raw Calib to Ch#1	Final Calib to Ch#1
Chamber 1	789.7	78	N2	125.5	6.45	105.05	126.09	100.56	1.000	1.000
	811.4	78	N2	128	6.45	93.7	126.58	99.13	1.000	1.000
	790.5	72	N2	126.6	7	100.6	126.55	100.83	1.000	1.000
	778.5	74	N2	124.5	6.45	106.5	125.76	99.79	1.000	1.000
	792.1	78	He	27.275	2.15	82.1	27.28	82.10	1.000	1.000
Chamber 2	788.1	78	N2	123	6	104.9	123.74	99.68	0.980	0.981
	811.7	78	N2	125.85	5.6	94.45	124.40	100.02	0.983	0.983
	788.2	72	N2	*	*	100.4	*	99.58	*	*
	778.5	74	N2	122.25	5.65	106.4	123.51	99.69	0.982	0.982
	791	77	He	26.85	2	82.05	26.85	82.05	0.984	0.984
Chamber 3	787	78	N2	124.5	6	104.7	125.34	98.98	0.992	0.994
	811.7	78	N2	127.5	6	94.45	126.05	100.02	0.996	0.996
	790	72	N2	126.25	6.5	100.25	126.25	100.25	0.997	0.998
	778.2	74	N2	124.1	6.2	106.3	125.38	99.46	0.997	0.997
	790.2	78	He	27.55	2.15	82.05	27.55	82.05	1.010	1.010
Chamber 4	786	78	N2	124.75	6.1	104.6	125.69	98.42	0.994	0.997
	811.4	78	N2	127.5	6.15	94	126.08	99.43	0.996	0.996
	790	72	N2	125.7	6.65	100.4	125.70	100.40	0.993	0.993
	779	74	N2	125.2	6.45	106.1	126.41	99.62	1.006	1.005
	790.2	78	He	27.35	1.85	82.05	27.35	82.05	1.003	1.003
Chamber 5	784.2	78	N2	128.25	7.3	104.35	129.35	97.35	1.022	1.026
	811.4	78	N2	131.25	7.25	93.9	129.83	99.33	1.025	1.026
	789.8	72	N2	129.7	8.1	100.45	129.72	100.36	1.024	1.025
	779.2	74	N2	128.3	7.3	106	129.49	99.61	1.031	1.030
	789	78	He	28.6	2.5	82.05	28.60	82.05	1.049	1.049
Chamber 6	791.6	78	N2	123.5	6.4	103.2	123.92	99.58	0.984	0.983
	811.4	78	N2	124.5	6.35	93.9	123.08	99.33	0.973	0.972
	789.3	72	N2	124.95	6.45	100.4	125.02	100.08	0.987	0.988
	779.3	74	N2	123.1	6.55	105.85	124.28	99.51	0.989	0.988
	788.7	78	He	27.55	2.4	82.1	27.55	82.10	1.010	1.010
Chamber 7	791.5	78	N2	123.25	2.6	103.2	123.67	99.54	0.982	0.981
	811.7	78	N2	124.5	2.6	93.75	123.05	99.32	0.973	0.972
	789.1	72	N2	124.75	3.25	100.4	124.83	99.99	0.985	0.986
	779.2	74	N2	121.75	2.75	105.8	122.94	99.41	0.978	0.978
	788.6	78	He	26.55	0.85	82.1	26.55	82.10	0.973	0.973
Chamber 8	790.6	78	N2	127.75	6.95	103.1	128.26	99.02	1.018	1.017
	811.4	78	N2	129.75	7	93.55	128.33	98.98	1.014	1.014
	789.8	72	N2	129.75	7.5	100.35	129.77	100.26	1.025	1.025
	779.2	74	N2	126.95	7.2	105.9	128.14	99.51	1.020	1.019
	788.5	78	He	28.3	0.9	82.15	28.30	82.15	1.038	1.038
Chamber 9	790.2	78	N2	122.75	4.1	103.1	123.30	98.84	0.978	0.978
	811.7	78	N2	124.8	4.2	93.45	123.35	99.02	0.975	0.974
	788.6	72	N2	125	4.9	100.3	125.13	99.66	0.987	0.989
	779.2	74	N2	121.35	4.3	105.9	122.54	99.51	0.975	0.974
	788.5	78	He	26.6	1.3	82.1	26.60	82.10	0.975	0.975

Table 3.4: Five sets of calibration data for all chambers of muon tube 26.
** Chamber did not read out for this test*

Alcove 1					
Channel	Tube	Chamber	Irrad Current(pA)	Non-Irad Current(pA)	Scale Factor
1	31	9	123.72	6.24	1.017
2	31	8	123.26	5.99	1.021
3	31	7	124.60	6.55	1.010
4	31	6	122.56	6.20	1.027
5	31	5	121.49	6.42	1.036
6	31	4	122.45	6.20	1.028
7	31	3	123.60	5.87	1.018
8	31	2	123.04	5.81	1.045
9	31	1	122.84	6.05	1.026
10	6	9	123.39	3.76	1.024
11	6	8	127.79	6.43	0.989
12	6	7	128.62	7.20	0.982
13	6	6	126.18	5.74	1.002
14	6	5	126.89	6.34	0.997
15	6	4	125.46	6.42	1.009
16	6	3	126.50	5.88	1.000
17	6	2	129.20	6.81	0.980
18	6	1	126.42	6.76	1.001
19	16	9	126.39	5.14	0.995
20	16	8	127.73	7.40	0.985
21	16	7	126.02	7.26	0.999
22	16	6	122.49	6.55	1.028
23	16	5	126.30	6.76	0.996
24	16	4	126.21	6.66	0.997
25	16	3	128.17	6.87	0.981
26	16	2	126.16	6.64	0.997
27	16	1	126.21	6.39	0.997
28	27	9	125.79	6.18	0.999
29	27	8	128.39	6.11	0.980
30	27	7	125.12	6.16	1.005
31	27	6	129.30	5.71	0.973
32	27	5	124.53	5.08	1.010
33	27	4	123.62	7.03	1.017
34	27	3	125.90	6.53	0.999
35	27	2	123.38	6.50	1.020
36	27	1	126.88	6.92	0.992
37	24	9	125.11	6.58	1.005
38	24	8	123.31	3.25	1.019
39	24	7	126.01	6.76	0.999
40	24	6	125.63	6.54	1.002

Table 3.5: Scale factors for channels 1-40 in Alcove 1. Channel number refers to the indexing scheme used by the readout electronics. Also given are the tube and chamber numbers for calibration referencing.

Alcove 1					
Channel	Tube	Chamber	Irrad Current(pA)	Non-Irad Current(pA)	Scale Factor
41	24	5	124.85	7.18	1.004
42	24	4	123.94	6.19	1.012
43	24	3	124.33	6.32	1.008
44	24	2	122.89	5.89	1.020
45	24	1	124.36	6.29	1.009
46	13	9	123.63	4.08	1.016
47	13	8	124.61	6.77	1.009
48	13	7	128.60	7.50	0.978
49	13	6	124.80	6.99	1.007
50	13	5	123.88	6.35	1.015
51	13	4	124.20	6.90	1.012
52	13	3	123.39	6.26	1.019
53	13	2	124.73	6.20	1.008
54	13	1	123.70	6.23	1.016
55	20	9	128.48	5.68	0.976
56	20	8	127.94	6.38	0.980
57	20	7	126.90	6.00	0.989
58	20	6	125.86	7.38	0.997
59	20	5	126.96	6.20	0.988
60	20	4	127.45	7.24	0.985
61	20	3	125.49	6.21	1.000
62	20	2	127.42	6.34	0.984
63	20	1	125.09	6.19	1.003
64	2	9	125.16	4.73	1.007
65	2	8	126.83	5.83	0.993
66	2	7	129.63	7.30	0.972
67	2	6	123.76	5.19	1.018
68	2	5	124.72	4.54	1.011
69	2	4	126.73	7.43	0.995
70	2	3	123.70	4.14	1.019
71	2	2	122.21	4.16	1.032
72	2	1	125.24	6.68	1.007
73	19	9	125.42	7.65	1.000
74	19	8	129.24	7.46	0.972
75	19	7	125.92	6.57	0.997
76	19	6	124.45	6.20	1.009
77	19	5	125.55	6.42	1.000
78	19	4	124.01	6.14	1.013
79	19	3	128.09	6.96	0.980
80	19	2	123.97	6.26	1.013
81	19	1	120.59	5.96	1.042

Table 3.6: Scale factors for channels 41-81 in Alcove 1. Channel number refers to the indexing scheme used by the readout electronics. Also given are the tube and chamber numbers for calibration referencing.

Alcove 2					
Channel	Tube	Chamber	Irrad Current(pA)	Non-Irad Current(pA)	Scale Factor
1	18	9	124.96	5.61	1.001
2	18	8	130.54	6.88	0.959
3	18	7	126.78	6.14	0.987
4	18	6	122.14	4.90	1.024
5	18	5	123.92	5.51	1.009
6	18	4	124.96	5.92	1.001
7	18	3	125.30	6.52	0.998
8	18	2	125.51	7.08	0.997
9	18	1	124.56	6.34	1.004
10	8	9	120.98	3.52	1.038
11	8	8	129.00	7.89	0.974
12	8	7	125.55	7.61	1.001
13	8	6	126.29	6.08	0.995
14	8	5	122.59	5.61	1.026
15	8	4	125.22	6.20	1.004
16	8	3	126.80	7.78	0.991
17	8	2	123.54	5.68	1.017
18	8	1	124.01	7.23	1.014
19	9	9	125.22	5.93	1.007
20	9	8	124.70	6.41	1.011
21	9	7	127.29	6.82	0.991
22	9	6	126.31	7.95	0.999
23	9	5	121.39	5.58	1.040
24	9	4	120.53	4.95	1.048
25	9	3	124.40	5.91	1.015
26	9	2	123.64	7.86	1.022
27	9	1	126.05	5.68	1.003
28	14	1	125.82	4.51	1.004
29	14	2	127.46	7.30	0.991
30	14	3	126.83	5.44	0.996
31	14	4	121.22	5.88	1.043
32	14	5	125.02	6.08	1.013
33	14	6	125.82	6.90	1.006
34	14	7	125.77	6.43	1.006
35	14	8	123.33	5.74	1.027
36	14	9	123.08	5.95	1.029
37	10	9	124.68	4.21	1.010
38	10	8	128.92	7.08	0.977
39	10	7	125.63	7.17	1.002
40	10	6	122.02	6.15	1.032

Table 3.7: Scale factors for channels 1-40 in Alcove 2. Channel number refers to the indexing scheme used by the readout electronics. Also given are the tube and chamber numbers for calibration referencing.

Alcove 2					
Channel	Tube	Chamber	Irrad Current(pA)	Non-Irad Current(pA)	Scale Factor
41	10	5	129.05	6.77	0.972
42	10	4	126.88	5.57	0.988
43	10	3	129.38	6.24	0.969
44	10	2	128.35	6.81	0.977
45	10	1	125.12	6.80	1.002
46	32	9	126.43	6.39	1.001
47	32	8	128.55	5.73	0.984
48	32	7	127.76	6.39	0.990
49	32	6	124.16	6.10	1.019
50	32	5	125.43	6.11	1.005
51	32	4	127.26	6.57	0.990
52	32	3	124.26	5.82	1.014
53	32	2	123.70	5.75	1.018
54	32	1	120.77	5.98	1.043
55	21	9	122.25	5.62	1.005
56	21	8	122.38	7.68	0.986
57	21	7	120.16	6.97	1.028
58	21	6	123.98	6.95	1.012
59	21	5	121.28	7.05	1.033
60	21	4	123.75	7.09	1.010
61	21	3	121.89	5.26	1.042
62	21	2	127.02	6.23	1.024
63	21	1	124.63	6.98	1.025
64	11	9	124.67	6.04	0.956
65	11	8	127.34	6.87	0.976
66	11	7	125.15	5.84	1.014
67	11	6	126.04	6.33	1.003
68	11	5	124.54	6.39	1.000
69	11	4	124.63	6.79	0.988
70	11	3	123.27	5.02	0.995
71	11	2	128.20	6.51	0.978
72	11	1	130.85	6.90	1.000
73	23	9	121.82	6.06	1.011
74	23	8	125.07	6.33	1.030
75	23	7	123.33	6.41	1.002
76	23	6	127.22	8.18	0.986
77	23	5	123.92	4.60	1.008
78	23	4	127.05	6.05	0.982
79	23	3	125.07	5.80	1.013
80	23	2	121.61	6.21	0.999
81	23	1	123.89	6.29	1.026

Table 3.8: Scale factors for channels 41-81 in Alcove 2. Channel number refers to the indexing scheme used by the readout electronics. Also given are the tube and chamber numbers for calibration referencing.

Alcove 3					
Channel	Tube	Chamber	Irrad Current(pA)	Non-Irad Current(pA)	Scale Factor
1	15	9	128.53	7.02	0.982
2	15	8	125.63	5.02	1.006
3	15	7	128.68	6.20	0.981
4	15	6	122.88	5.53	1.029
5	15	5	123.88	7.06	1.021
6	15	4	123.48	6.68	1.024
7	15	3	122.04	5.65	1.037
8	15	2	124.50	6.58	1.017
9	15	1	123.38	6.07	1.027
10	4	9	130.48	6.97	0.973
11	4	8	126.64	3.31	1.002
12	4	7	128.51	7.51	0.988
13	4	6	130.54	6.48	0.972
14	4	5	127.78	4.40	0.997
15	4	4	126.32	4.26	1.009
16	4	3	126.85	6.76	1.004
17	4	2	129.61	7.03	0.982
18	4	1	126.88	6.61	1.003
19	26	9	122.73	4.12	1.022
20	26	8	127.65	6.93	0.983
21	26	7	123.29	2.61	1.019
22	26	6	123.45	6.43	1.018
23	26	5	128.22	7.30	0.975
24	26	4	124.69	6.18	1.003
25	26	3	124.49	6.02	1.006
26	26	2	122.97	5.65	1.019
27	26	1	125.44	6.44	1.000
28	25	9	124.92	6.76	1.010
29	25	8	126.36	6.36	0.998
30	25	7	124.55	6.50	1.012
31	25	6	124.43	6.77	1.013
32	25	5	122.53	4.46	1.029
33	25	4	122.48	6.47	1.029
34	25	3	124.16	6.78	1.015
35	25	2	124.77	7.58	1.010
36	25	1	124.83	6.38	1.009
37	1	9	124.08	4.97	1.017
38	1	8	128.11	5.97	0.985
39	1	7	123.10	3.29	1.026
40	1	6	126.83	7.36	0.995

Table 3.9: Scale factors for channels 1-40 in Alcove 3. Channel number refers to the indexing scheme used by the readout electronics. Also given are the tube and chamber numbers for calibration referencing.

Alcove 3					
Channel	Tube	Chamber	Irrad Current(pA)	Non-Irad Current(pA)	Scale Factor
41	1	5	124.35	3.92	1.010
42	1	4	126.68	6.82	0.992
43	1	3	126.31	6.99	0.995
44	1	2	125.26	6.55	1.003
45	1	1	120.96	4.01	1.038
46	29	9	121.48	3.49	1.037
47	29	8	127.32	6.58	0.990
48	29	7	122.36	4.76	1.031
49	29	6	122.93	5.24	1.027
50	29	5	124.61	6.81	1.013
51	29	4	121.03	5.23	1.046
52	29	3	124.28	6.68	1.017
53	29	2	122.00	6.09	1.036
54	29	1	127.73	6.95	0.989
55	5	9	124.28	4.36	1.018
56	5	8	128.99	6.36	0.980
57	5	7	126.23	6.65	1.002
58	5	6	125.23	5.63	1.010
59	5	5	122.87	5.36	1.031
60	5	4	125.16	6.20	1.011
61	5	3	124.15	4.74	1.019
62	5	2	124.70	5.80	1.015
63	5	1	127.19	5.49	0.995
64	30	9	123.62	5.91	1.018
65	30	8	123.35	5.06	1.021
66	30	7	123.11	6.14	1.022
67	30	6	125.87	7.65	1.000
68	30	5	127.85	6.51	0.984
69	30	4	125.22	5.95	1.005
70	30	3	123.15	6.49	1.025
71	30	2	123.89	6.78	1.037
72	30	1	121.45	5.27	1.037
73	28	9	125.91	7.26	0.996
74	28	8	122.96	4.60	1.020
75	28	7	124.90	6.62	1.004
76	28	6	131.48	6.69	0.953
77	28	5	125.69	6.74	0.998
78	28	4	127.44	7.46	0.984
79	28	3	126.68	6.44	0.991
80	28	2	123.06	6.51	1.020
81	28	1	126.06	5.64	0.996

Table 3.10: Scale factors for channels 41-81 in Alcove 3. Channel number refers to the indexing scheme used by the readout electronics. Also given are the tube and chamber numbers for calibration referencing.

Spare Tubes				
Tube	Chamber	Irrad Current(pA)	Non-Irad Current(pA)	Scale Factor
3	1	125.03	6.88	0.984
3	2	125.66	5.92	0.994
3	3	126.74	7.42	1.022
3	4	125.10	5.73	0.992
3	5	126.26	6.57	1.000
3	6	127.55	6.94	1.009
3	7	123.86	4.50	0.996
3	8	127.43	4.71	1.005
3	9	128.67	6.53	1.010
7	1	124.39	7.11	0.997
7	2	126.41	7.32	1.000
7	3	125.20	6.83	0.989
7	4	124.99	6.64	0.993
7	5	126.14	7.03	0.993
7	6	126.08	6.75	1.002
7	7	126.72	6.53	1.000
7	8	125.34	6.09	0.990
7	9	125.70	6.04	1.006
12	1	124.55	6.14	0.987
12	2	122.83	4.94	0.993
12	3	121.54	6.31	0.995
12	4	123.23	7.30	1.006
12	5	124.49	5.92	1.003
12	6	124.37	6.37	1.013
12	7	125.81	6.25	1.028
12	8	126.05	4.91	1.016
12	9	126.79	7.11	1.003
17	1	120.24	5.64	0.997
17	2	123.96	7.67	0.955
17	3	126.02	7.50	0.993
17	4	125.15	6.02	0.970
17	5	128.40	6.88	0.978
17	6	129.40	8.38	1.003
17	7	126.51	8.33	0.996
17	8	125.29	6.12	1.013
17	9	126.76	7.68	1.045

Table 3.11: Scale factors for the spare tubes. Given are the tube and chamber numbers for calibration referencing.

Chapter 4

Neutron Studies

4.1 Introduction

The hadron monitor will see charged particle fluxes as high as 2×10^{9}/cm^2/spill, but will also be exposed to neutron fluxes as high as 13×10^9/cm^2/spill [19]. The detectors in the first muon alcove will see approximately 10^7 muons/cm^2/spill during low-energy beam running, but as much as 9 times as many neutrons [19]. Most of the neutrons will be low in energy, with a peak at 30 MeV. The response of the ion chambers to charged particle flux has been studied with electron and proton beams [30, 31]. In this Chapter, we study the response of ion chambers to neutrons, which can potentially comprise a significant background to the charged particle signal in the hadron monitor.

We have examined the response of four prototype, parallel plate ion chambers [32] to neutron fluxes at the University of Texas Nuclear Engineering Teaching Laboratory. The neutrons for this test were provided by PuBe radionuclide sources, which produce 2-10 MeV neutrons at a rate of about 1.5×10^8/sec. The primary objectives of this test were to determine the ion-

ization due to neutron flux and to study the shape of the voltage plateau due to neutron flux as compared to that due to charged particle flux.

Unlike charged particles, neutrons do not ionize the gas directly. Instead, fast neutrons interact with nuclei and create a recoil nucleus. This charged particle very quickly deposits its energy through ionization. The recoil particle can be produced either in the chamber gas or in the plates of the chamber electrodes.

This Chapter procedes as follows. The ion chambers and signal readout are described in Section 4.2. The characteristics of the PuBe neutron source are described in Section 4.3. The measurements performed and the estimated neutron flux delivered to the chambers are described in Section 4.4. Section 4.5 provides a naive estimate of the expected ionization using data from previous measurements. The results of the various measurements are described in Section 4.6. Section 4.7 concludes.

4.2 Experimental Setup

4.2.1 Ionization Chambers

In this test four ion chambers are used in two seperate gas vessels. One vessel contained two chambers with 2 mm gas gaps, the other had two chambers with 5 mm gas gaps. The two vessels are welded shut except for various signal and HV feedthroughs.

The interior of the gas vessel is shown in Figure 4.1. The vessel was milled out of Aluminum. The various feedthroughs are made with Aluminum compression fittings that are welded to the box. The cover to the vessel is welded shut after the interior assembly completed. In each vessel, two ion

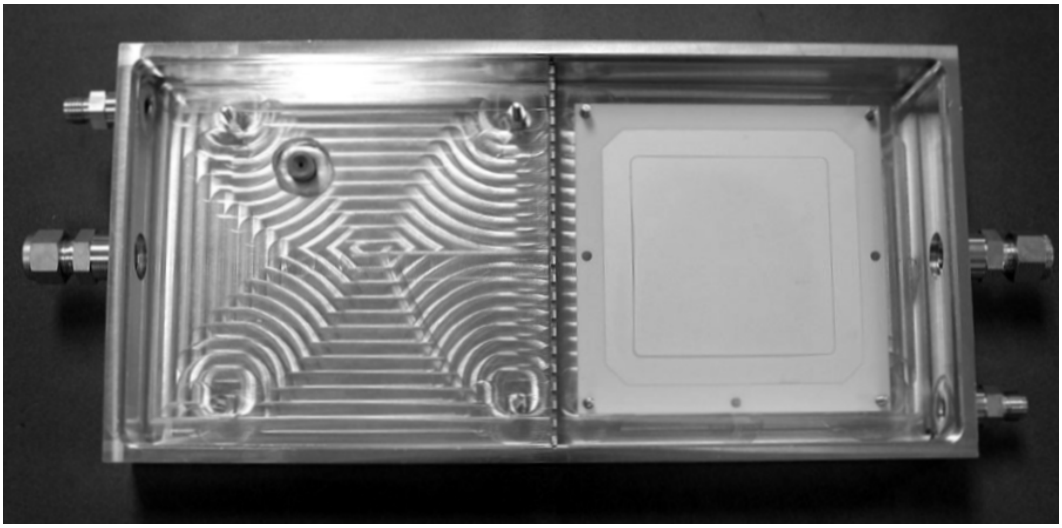

Figure 4.1: An interior view of one of the gas vessels used in this test. One sense pad has been installed on the right, and part of a signal feedthrough is visible on the left.

chambers are mounted side by side, separated by an Aluminum mesh which provides electrostatic screening.

Signal and high voltage feedthroughs through the vessel walls are made of Swagelock compression fittings and PEEK [1] dielectric. A PEEK feedthrough can be seen coming out of the Aluminum in Figure 4.1. A cross section of the chamber vessel as mounted in the test is in Figure 4.2.

The high radiation levels in this test motivated a chamber vessel construction largely of aluminum to avoid residual activation of the detectors. Stainless steel produces long-lived radionuclides with 1 year or more half-lives.

The two vessels are mounted on an Aluminum plate such that the chamber plates face each other as shown in Figure 4.2. The chambers were brought close together to maximize the solid angles acceptance of the neutron sources placed between the vessels.

[1] Poly (Ether - Ether - Ketone), a product of Victrex Corporation.

Two ion chambers have 1 μCi Americium-241 α source mounted aimed into their gas gap (one 2mm chamber and one 5mm chamber) through feedthroughs in the sides. The alpha sources are present on the two chambers throughout the tests below. These permit calibration of temporal effects such as barometric pressure variations. The other two chambers have no alpha sources.

Two dummy signal feedthroughs, one in each gas vessel (shown in the upper left and lower right of the diagram in Figure 4.2, are read out but not connected to any actual ion chamber.

The compression fittings making up the electrical feedthroughs are potted on the exterior with epoxy to electrically insulate them and also to prevent stray ionization from the exterior air volume from collecting on the signal electrodes. The potted exteriors of the feedthroughs are further wrapped in grounded aluminum foil to complete a coaxial shield. In initial tests, we discovered that significant ionization was produced outside the chamber volume and then collected on the signal lines because stray electric fields from the HV feedthroughs.

Kapton coaxial cables deliver the HV and carry the signals.

4.2.2 Gas System

The gas used in this test is Alphagaz I as provided by Air Liquide. Alphagaz I is rated as 99.998% pure Helium. The Helium, delivered from a cylinder, is regulated to 30 psi. From there it passed through a Oxygen getter. From the getter it passed through a flowmeter set to about 100 cu. in. / min., leading to a pressure in the gas vessels of less than 1" of water over atmosphere. Pressure in the vessels is calibrated vs. flow rate with a Dwyer Magnahelic, which was removed before neutrons were introduced. The ouput of the gas vessels

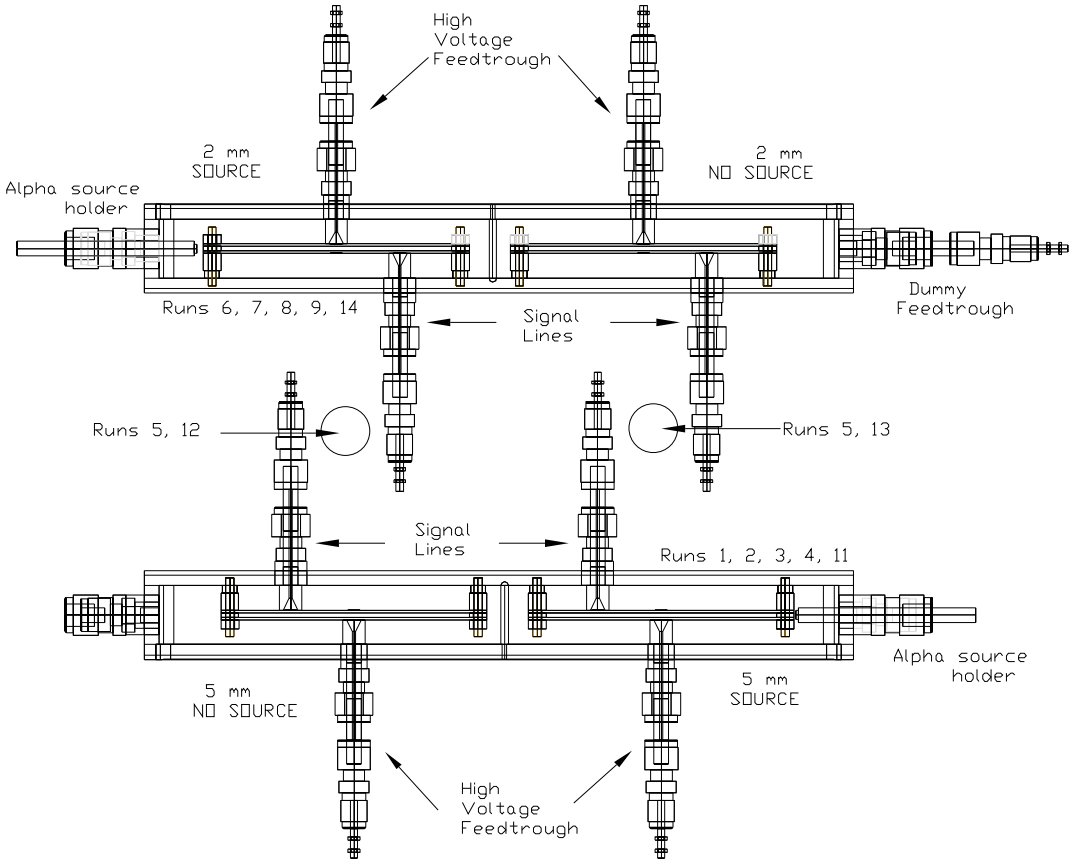

Figure 4.2: The apparatus used in this test. Two gas vessels each house two ion chambers, one with and one without an alpha source illuminating it. Each vessel has as well a dummy electrical feedthrough which is read out during the test, but has no ion chamber connected to it. The placements of the PuBe neutron sources during each of the runs of the test are noted in the figure.

passes through an Illinois Instruments gas analyzer to monitor O_2 impurities. Typicial operation showed 0.5-1.5 p.p.m. of O_2. After the analyzer, the gas flow passed through a coil of about 30' of tubing before returning to atmosphere.

All seals and welds were checked for leaks by overpressuring the system and using a Matheson leak hunter. All of the piping is stainless steel, except in the radiation area where it is Aluminum.

4.2.3 Electronics and Data Aquisition

The high voltage to the chambers is supplied by Ortec 480 dual bias supplies which have <1 mV ripple on 200 V. The 2mm chambers would each accept a maximum of about 500 Volts in Helium before breaking down. At this voltage the He gas amplification in the chamber is about 20. The 5 mm chambers accepted 550 Volts for one and 700 Volts for the other before breaking down. The breakdown for the 5 mm chambers was at the feedthrough.

The output current of each chamber was read by a Keithley 480 picoammeter. The nominal sensitivity of the digital display of a Keithley 480 picoammeter is 1 pA. However, we found that by using the voltage output of the current-to-voltage amplifier we could achieve a sensitivity of better than 0.1 pA for steady currents. The output voltage corresponded to -1 mV per 1 pA. The reason for the 1 pA sensitivity rating of the Keithley 480 appears to be drift in the internal amplifier circuit that was of the 0.5-1.5 pA level which occurred spontaneously every few hours. These drifts occurred over a period of several minutes. With frequent monitoring of the signals, we could discard data runs in which drifts were observed.

The high voltage and picoammeter voltage readings were recorded via

an ADC.[2]. The ADC is 12 bit, 0-5 Volts (1 count = 1.2 mV). To improve our signal sensitivity the signal lines from the picoammeters were routed through gain=-20 amplifiers. The net signal sensitivity is then 0.06 pA per ADC count. The high voltage channels were run through amplifiers of 1/200 gain giving a sensitiviy of 0.25 V per ADC count.

The ADC was read out via a serial line to a Windows computer. Control of the ADC and data recording was carried out through LabView. Measurements proceeded at a rate of several Hz, alowing many samples to be averaged for data points.

4.3 Neutron Source

The neutrons for this test are obtained from six individual PuBe sources. Four of the sources are ^{239}Pu totalling 8.99 Curies. The two others provide 46 Ci of ^{238}Pu. The neutron yield from the ^{239}Pu is measured to be 57 per 10^6 alpha decays, but calculations suggest 65 per 10^6 α decays [33]. Given that yields may vary for specific alloy samples [34], we take $(60 \pm 5) \times 10^{-6}$ neutrons/α. The theoretical neutron yield for ^{238}Pu is $(79 \pm 5) \times 10^{-6}$ n/α [35]. We estimate all sources combined to emit $(1.57 \pm 0.13) \times 10^8$ neutrons/sec.

The PuBe source also emits gamma rays, which form a background for the measurements of this paper. In approximately 57% of ^{9}Be$(\alpha, n)^{13}$C captures which lead to an emitted neutron from the PuBe source, the ^{13}C* excited state emits a 4.4 MeV gamma [36]. These γ's may Compton scatter in our chamber materials, yielding additional ionization from the Compton electron. This background is discussed further in Section 4.5.

[2]Produced by Mind-Tel Systems, Syracuse, NY.

4.4 Neutron Source Placement and Flux Estimation

Ten runs were taken over the course of this test while the chambers were flushed with Helium gas. Five runs were taken while the chambers were under Argon gas flow. Runs 0 and 10 had no PuBe sources present; these runs serve as the baseline which is subtracted from subsequent runs to deduce the effects of neutron interactions in the gas. Each run consists of placing the PuBe sources in a new location.

The neutron sources could only be placed by the Health Physicist, and no others were allowed near the apparatus while the sources were present. The location of the PuBe sources for each run during this test are noted in Figure 4.2. In Run 2, for example, the PuBe sources are placed closest to the 2 mm chamber which has the α source mounted to it. While all four chambers should see neutrons in this run, the 2 mm chamber with the alpha should see the largest flux. The source placements are noted as well in Tables 4.1 and 4.2.

In Table 4.1, 'base' means that the source canisters are placed on the table which corresponds to the low edge of the vertically-placed chambers, while 'Ctr' means that the source canisters were placed on a small pedestal to center them in height on a particular chamber. The placement 'middle' for Run 5 means that the sources where placed half-way between facing chambers. That is, for the 2mm chamber with an α and the 5mm chamber without an α, sources were placed half-way between them during Run 5. For the 2mm chamber without an α and the 5mm chamber with an α, sources were likewise midway between them (see Figure 4.2).

The neutron flux through each chamber in these runs is estimated by multiplying the source's neutron activity (see Appendix 4.3) by the fraction of solid angle about the sources subtended by the $8\times8\text{cm}^2$ active area of the ion chambers. Source locations with respect to the chambers were measured by analyzing photographs of the source configurations. Photographs of each source placement were taken from several angles by the laboratory staff and the position of the sources calibrated using the known dimensions of the chamber vessels. In performing the solid angle integral over the ion chamber faces, the PuBe sources are assumed to be point-like, which is reasonable given that the PuBe pellets are relatively small compared to the canisters in which they reside. Tables 4.1 and 4.2 give the neutron flux estimates for each run, where the neutron flux is quoted in pA (6.2×10^6 neutrons/sec).

In Tables 4.1 and 4.2 a cosine-weighted flux is calculated as well which additionally weights for the pathlength of the neutron passing through the ion chamber gas gap (a neutron traversing the chamber head-on at normal incidence receives a weight 1.0, while a neutron entering at 45° to the normal receives an extra weight of $\sqrt{2}$). This latter, cosine-weighted, flux is perhaps more useful when trying to study the probability of recoil event in the gas by a neutron, which grows with pathlength through the gas.

The flux calculation does not consider the effects of neutrons incident upon the feedthroughs or cables, which have very different positions than the chambers.

The error in the fluxes due to the estimation method is about 10% for the smaller fluxes and 20% for the largest, which are very sensitive to the source positions.

Run No.	PuBe Placement	PuBe Activity (Ci)	Barometric Pressure (in. Hg)	Neutron Fluxes (pA) at Chambers			
				2mm α	2mm no-α	5mm α	5mm no-α
0	No n's	0	30.1	0	0	0	0
1	5mmS base	46	29.9	0.10(0.21)	0.83(0.92)	2.23(2.84)	0.15(0.36)
2	5mmS base	55	29.9	0.28(0.41)	0.94(1.04)	2.53(3.04)	0.17(0.41)
3	5mmS Ctr.	55	30.0	–	–	3.12(4.00)	–
4	5mmS Ctr.	55	30.0	–	–	3.12(4.00)	–
5	Middle	46	30.0	1.26(1.46)	1.26(1.46)	1.26(1.46)	1.26(1.46)
6	2mmS base	46	29.8	2.23(2.84)	0.15(0.36)	0.10(0.21)	0.83(0.92)
7	2mmS base	55	30.1	2.53(3.04)	0.17(0.41)	0.28(0.41)	0.94(1.04)
8	2mmS ctr.	55	30.1	3.12(4.00)	–	–	–
9	2mmS ctr.	55	30.1	3.12(4.00)	–	–	–

Table 4.1: Runs taken during the study of neutron interactions in Helium gas. The placement and number of the PuBe sources are noted, as well as the expected neutron flux on each of the chambers during each run. The neutron fluxes are quoted in units of 'picoamperes', where 1 pA = 6.2×10^6 neutrons/sec. Both the unweighted and cosine-weighted fluxes (in parentheses) are listed.

Run No.	PuBe Placement	PuBe Activity (Ci)	Barometric Pressure (in. Hg)	Neutron Fluxes (pA) at Chambers			
				2mm α	2mm no-α	5mm α	5mm no-α
10	No n's	0	29.9	0	0	0	0
11	5mmS base	46	30.0	0.10(0.21)	0.83(0.92)	2.23(2.84)	0.15(0.36)
12	Middle1	46	29.0	0.28(0.66)	1.26(1.46)	1.26(1.46)	0.28(0.66)
13	Middle2	46	30.3	1.26(1.46)	0.28(0.66)	0.28(0.66)	1.26(1.46)
14	2mmS base	46	30.2	2.23(2.84)	0.15(0.36)	0.10(0.21)	0.83(0.92)

Table 4.2: Runs taken during the study of neutron interactions in Argon gas. The placement and number of the PuBe sources are noted, as well as the expected neutron flux on each of the chambers during each run. The neutron fluxes are quoted in units of 'picoamperes', where 1 pA = 6.2×10^6 neutrons/sec. Both the unweighted and cosine-weighted fluxes (in parentheses) are listed.

4.5 Expected Rates

The measured ionization due to the neutron sources comes from the scattering of neutrons in the chamber gas and electrodes followed by ionization deposited in the gas by the scattered recoil nuclei. Additionally, the accompanying 4.4 MeV γ's from the PuBe source may Compton scatter in the chamber walls, and the scattered electrons may deposit energy in the chamber gap. In this section we estimate the ionization rate induced by the PuBe source, accounting separately for (1) the ionization from recoil gas molecules scattered elastically by the PuBe neutrons; and (2) the ionization from Compton electrons ejected by the 4.4 MeV γ's. "Wall effects," whereby γ rays are produced by inelastic interactions of neutrons in the chamber wall materials [56], are not considered. Similar estimates of neutron scattering in gaseous chambers have been used to estimate rates in drift chambers downstream of a beam dump [57]. The results of the calculations are summarized in Table 4.9.

4.5.1 Neutron Interactions

Cross sections of neutrons in the 2-40 MeV energy range have been measured for many of the materials in our ionization chambers. Some published data is given in Table 4.3. At low energies (< 10 MeV) neutron scattering is largely elastic [34]. Although not many papers quote both inelastic and elastic cross sections, it may be inferred from the data in Table 4.3 that inelastic processes are present even for the present test at $E_n = 2 - 10$ MeV.

Because inelastic neutron-nucleus processes are not well-known, it is difficult to estimate the ionization from all recoiling particles (nuclei, gamma rays) produced in the neutron-nucleus scattering. We attempt to provide a crude estimate of the ionization expected per neutron in our chambers which

ignores the complexity of multiple recoil particles and assume the only recoil nucleus is produced via elastic scattering.

The interaction lengths deduced from σ_{tot} permit estimates of neutron loss which occurs before the chamber volume, as well as interaction probability in the gas gap itself. Fortunately, only 3% of the neutrons will be lost in the 3 mm thick wall of the aluminum vessel, and 1% of neutrons interact in the ceramic plates, which together comprise a reasonably small correction to the flux estimates given previously.

4.5.2 Properties of the Recoil

In the case of pure elastic scattering, the recoil energy can be defined as a function of the neutron energy, scattering angle (of the nucleus), and the atomic number [34]:

$$E_R = \frac{4A}{(1+A)^2}(\cos^2\theta)E_n \tag{4.1}$$

where E_R is the recoil nucleus energy, E_n the incident neutron energy, A the target nucleus mass, and θ the recoil angle. If the scattering is purely elastic, the recoil energy distribution is flat until the maximum recoil ($\theta = 0$), so the mean recoil energy is one half of the maximum transferred energy[34, 49]:

$$\overline{E_R} = \frac{2A}{(1+A)^2}E_n \tag{4.2}$$

The mean energy imparted to each material present in the chambers are tabulated in Table 4.8.

To determine ranges of recoil nuclei in helium or argon gas, values were extrapolated from range-energy curves for alpha particles. The range of a recoil nucleus in a given medium is related to the range of an alpha particle

Element	A	Z	σ_{tot} (b)	σ_{el} (b)	E_n (MeV)	$\lambda_{int}(cm)$	Ref.
Helium	4	2	4.1	–	2	9.3×10^3	[37, 38]
			2.5	–	4	1.5×10^4	[37, 38]
			2.1	–	6	1.8×10^4	[37, 38]
			1.7	–	8	2.2×10^4	[37]
			1.5	–	10	2.5×10^4	[37]
			1.0-1.2	–	14	3.5×10^4	[38, 39]
			0.78-1.0	–	20	4×10^4	[37, 38, 40]
			0.56	–	30	6.8×10^4	[37, 40]
			0.44	–	40	8.6×10^4	[37]
Oxygen	16	8	1.6	1.1	14		[41]
Aluminum	27	12	1.7	–	14-18	9.8	[42]
			2.3	1.5	4.5		[43]
			2.3	1.4	7.5		[43]
			–	1.1	14		[44]
Argon	40	18	3.3	–	2-6	1.2×10^4	[38]
			2.0	–	12-20	1.9×10^4	[38]
			2.0	1.0	14	2.1×10^4	[41]
			–	1.0	14		[44]
Silver	108	47	4.4	–	9-16	5.1	[46]
			4.33	2.11	6.7	5.2	[45]
Platinum	196	78	–	–	–	–	
Lead	207	82	∼4.8	–	9-12	4.7	[46]
			∼5.5	–	12-16	4.2	[46]
			–	2.6	14		[44]

Table 4.3: Neutron scattering cross sections (total and elastic) on various nuclei relevant to the NuMI ion chambers in the 2-40 MeV energy range. The total cross sections are deduced from extrapolation of elastic scattering to $q^2 = 0$. The interaction length $\lambda_{int} \equiv 1/(n\sigma_{tot})$, where n is the atomic number density (quoted at STP for gases). No data is available for Pt, but measurements have been made for Pb.

Element	A	Z	$\overline{E_R}/E_n$	Particle Range in Media		
				Helium (mm)	Argon (mm)	Platinum (μm)
Helium	4	2	0.320	47	–	–
Oxygen	16	8	0.111	17	2.8	0.56
Aluminum	27	12	0.069	12.3	1.9	0.27
Argon	40	18	0.048	–	1.2	–
Silver	108	47	0.018	2.6	0.27	0.04
Platinum	196	78	0.010	0.74	0.13	0.03

Table 4.4: Elastic scattering data for materials found in an ion. chamber. The average recoil energy is provided as a portion of the neutron's energy, as calculated from Equation 4.2. Range is calculated for the typical fully-ionized recoil nucleus of a 5 MeV neutron in gaseous Helium, gaseous Argon, and Platinum, using data from [47, 48] and the scaling law from [34].

in the same medium by the relation[34]

$$R_{nucleus} = R_\alpha \frac{m_{nucleus}\sqrt{z_\alpha}}{m_\alpha\sqrt{z_{nucleus}}} \tag{4.3}$$

where m is the mass, z the charge, and R_α is the range of the alpha in the given medium for an alpha *of the same velocity.* Thus, the range of various nuclei can be deduced from the well-measured range of alpha particles in various media.[47, 48] The data for alpha particle ranges are reproduced from [47, 48] in Figure 4.3.

Table 4.8 shows the ranges of recoil nuclei traversing the chamber gas (Helium or Argon) or passing through the Platinum electrodes, assuming the previously calculated nuclear recoil energy for completely ionized nuclei. The ranges of recoil Al, O, Pt, or Ag nuclei from the walls are insufficient to traverse the chamber wall materials and reach the chamber gas volume, with the exception of Pt ions liberated very near the electrode surface. Particle ranges in the Platinum electrodes are far less than the 10 μm thickness of the Ag-Pt electrodes, so it is unlikely that recoils created in the electrodes or in the ceramic can enter the chamber gas and contribute to the ionization. Even

the Pt ions will contribute insignificant ionization since the Pt ions' energies are quite low. In fact, the utility of Pt electrodes for reducing "wall-effects" in neutron interactions has been noted previously [50].

4.5.3 Ionization by Recoils

We estimate now the ionization deposited in the chamber gas by the nuclear recoils. Given the ranges of the recoil particles in Table 4.8, we assume that only recoils of the chamber gas elements (Ar or He) contribute to the observed ionization.

To calculate the ionization by the recoiling Helium in a Helium-filled chamber we use the known $dE/dx = 380$ keV/cm [48] for 1.6 MeV α particles and divide by the $w = 32$ eV to create an electron-ion pair in the gas [51] to obtain 11,900 ionizations/cm created by the Helium recoil. In Argon gas, we assume the number of ionizations produced is the recoil energy divided by the energy to create an electron-ion pair in the gas ($w = 27$ eV for Argon), which gives 8900 ionizations for the 240 keV recoil of a 5 MeV neutron.

To estimate the average ionization per neutron, we multiply the ionization per nuclear recoil by the probability for a neutron to interact in the chamber gas, obtained from the interaction length in Table 4.3. The results are given in Table 4.9.

4.5.4 Gamma Rate

To estimate the ionization caused by γ rays emanating from the PuBe source, we performed a parametric Monte Carlo calculation of γ's Compton scattering in the chamber wall materials, followed by energy loss and multiple scattering by the Compton-scattered electrons. The ionization induced in the chamber

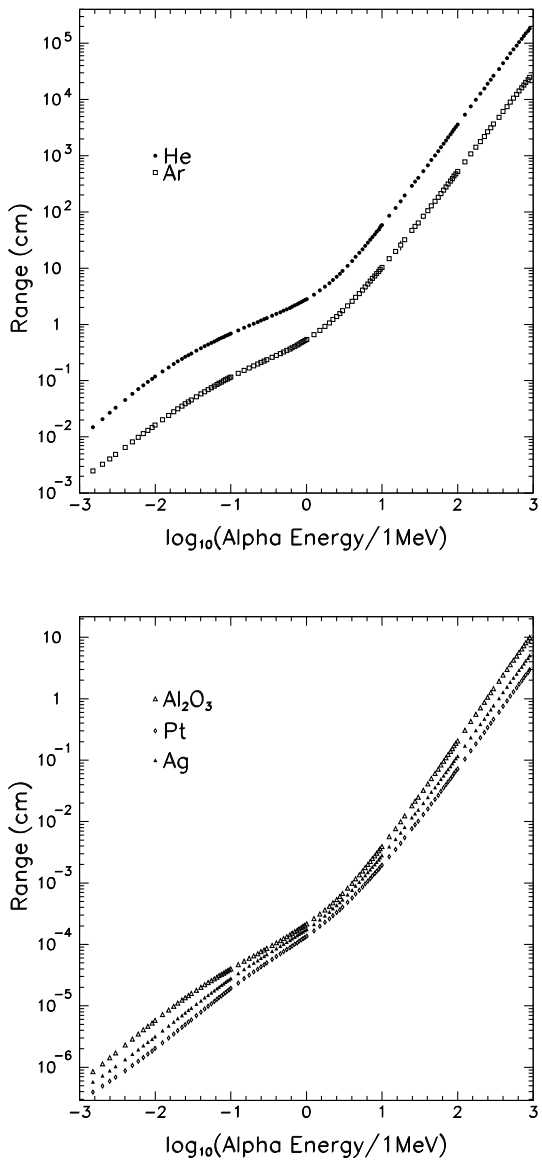

Figure 4.3: Range of alpha particles in either (top) the chamber gases or (bottom) materials in the ion chamber electrode plates, as taken from [47, 48].

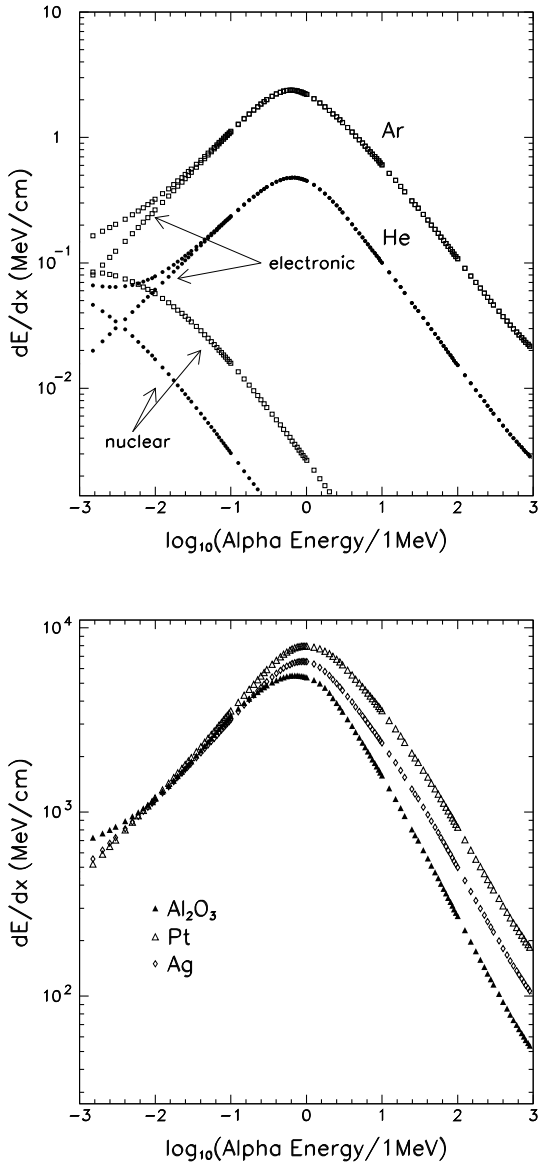

Figure 4.4: Total stopping power (dE/dx) of alpha particles in either (top) the chamber gases or (bottom) materials in the ion chamber electrode plates, as taken from [47, 48]. Included in the graphs for the chamber gases are the contributions from electronic stopping power (energy loss resulting in ionizations or atomic excitations) and nuclear energy loss (caused when a slow-moving ion undergoes nuclear collisions), and the sum of the two (the total stopping power).

gas volume is calculated for those electrons which arrive there.

Compton scattering of the 4.4 MeV γ's occurs with approximately 1 barn cross section [52]. This yields a probability of scattering in the Aluminum chamber walls of 25% and a probability of scattering in the ceramic plates of 11%. Including the fact that only 57% of neutrons are accompanied by a 4.4 MeV γ, this yields 19% of neutron events producing a Compton scatter in the chamber walls.

After the Compton scatter, the electron energy is calculated. Its energy loss is calculated using tabulated stopping power dE/dx data [58]. Multiple scattering of the electron in the Aluminum wall and in the ceramic is estimated as in [52]. If the path through each material (aluminum or ceramic) is greater than the electron's range, the electron does not reach the chamber gas volume. Approximately 74% of the Compton electrons are either ranged out in the chamber walls or are multiple scattered away from the gas volume, so that only 26% of the Compton e^- created in the walls reach the chamber volume.

The dE/dx of the electrons arriving in the chamber gas volume is multiplied by the path length of the electrons through the gas volume. The electron pathlength through the gas can be larger than the electrode separation due to their large multiple scattering. The range of the electrons is $10^3 - 10^4$ cm in He [58], so no electrons range out in the gas. For the He gas, we find a mean of 3.7 (8.8) ion pairs created in the 2 mm (5 mm) chamber. The results after multiplying by the probability 0.19×0.26 to have a Compton electron, are shown in Table 4.9.

4.6 Plateau Measurements

In each of the runs, the bias voltage for each chamber was ramped from zero volts until gas amplification was observed. Runs 0 and 10, which have no neutron sources present, are used as a baseline which is subtracted from subsequent runs to determine the neutron induced ionization in the gas. As expected, only the chambers with an alpha source show an appreciable signal during Runs 0 and 10. All chambers show an additional signal when significant neutron fluxes are present.

'Zero signal' was determined by measuring the chamber plateau curve with both positive and negative bias voltages and assuming the plateau values to be symmetrical about zero signal. In this way, stray contact potentials on the chamber which could initiate ionization current even with zero applied bias voltage could be accounted for. An example of a plateau curve of two of the ionization chambers is shown in Figure 4.5. In this figure, the plateau curve is shown for the 2mm gap and 5mm gap chambers which have an α source mounted to them during Runs 0 and 4. As can be seen, the 5mm chamber is somewhat asymmetric about our *ab initio* estimate of zero ionization current, indicating a contact potential is present, while the 2mm chamber is relatively symmetric.

The data are summarized in Tables 4.5 and 4.6 for the Helium and Tables 4.10 and 4.11. The quantities displayed in the tables are: 1) Run #, corresponding to the runs listed in Tables 4.1 and 4.2; 2) $I^+(I^-)$, the ionization current observed on voltage plateau with positive (negative) voltage bias on the chamber; 3) $\langle I \rangle$: the average of I^+ and I^-; 4) I due to neutrons, which is the difference of $\langle I \rangle$ for a given run and $\langle I \rangle$ recorded with no neutrons present (subtracts off the signals from alpha sources); 5) n flux, taken from Tables 4.1

and 4.2.

4.6.1 Helium Results

Figure 4.6 shows the plateau curves for all the runs taken with Helium gas after correcting for contact potential effects; *i.e.:* adding an offset to the zero ionization current to make the plateaus symmetric for positive and negative chamber bias potentials. Tables 4.5 and 4.6 summarize the Helium runs. For several runs the plateau curves span only positive bias voltages. These were scaled by the same fraction as for other runs of the same chamber.

A slight slope with voltage is visible for some of the plateau curves. This effect is caused by stray ionization outside of the primary gas volume is being collected due to stray fields from the HV feedthrough to the signal feedthrough [14]. The plateau slope was reduced greatly by shielding around these feedthroughs.

Figure 4.7, shows the neutron-induced ionization current in Helium *vs.* the neutron flux incident on the chamber. The neutron flux plotted along the horizontal axis is the pathlength cosine-weighted calculation of the neutron flux.

We have fit the data in Figure 4.7 to find the average neutron-induced ionization in Helium. The fit constrained to go through the origin gives slope values:

$$0.49 \pm 0.06 \text{ ionizations / neutron (5 mm chambers)}$$
$$0.26 \pm 0.07 \text{ ionizations / neutron (2 mm chambers)}$$

Allowing the vertical intercept to float in the fit changes the slope by only 0.03 ionizations/neutron, and the fitted vertical intercepts are consistent with zero (0.04±0.05 and 0.05±0.05 ionizations for the 5 mm and 2 mm chambers,

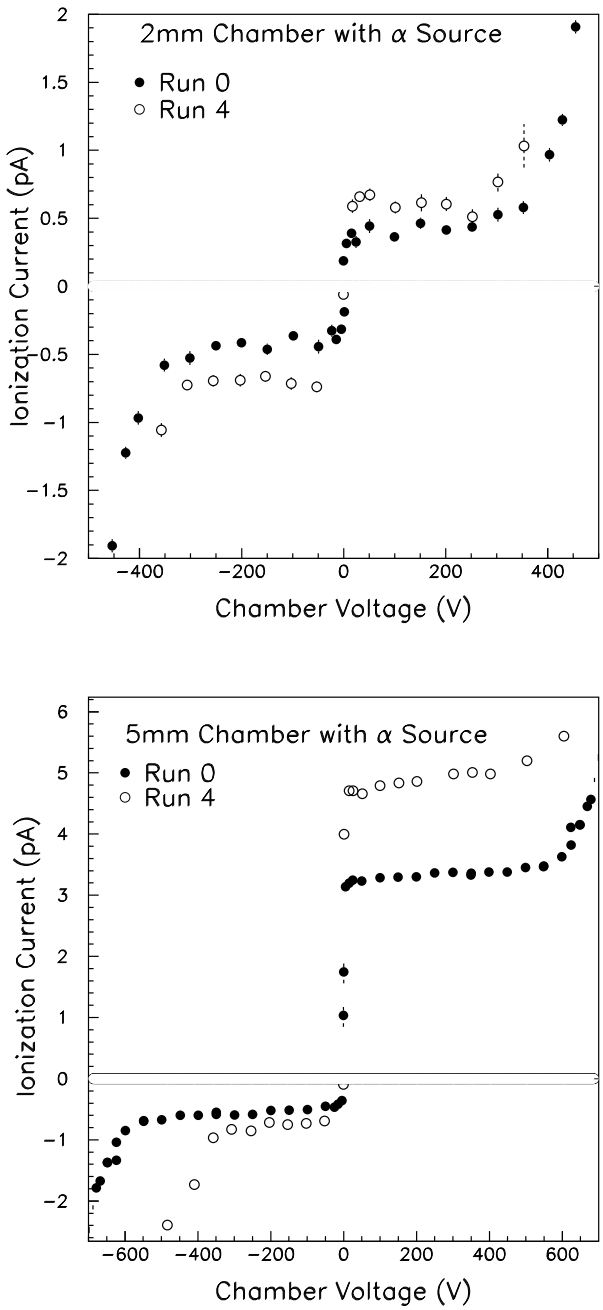

Figure 4.5: +/- plateau curves for the 2mm and 5mm chambers with an α source. While the 2mm chamber is fairly symmetric, the 5mm chamber demonstrates a clear contact voltage offset.

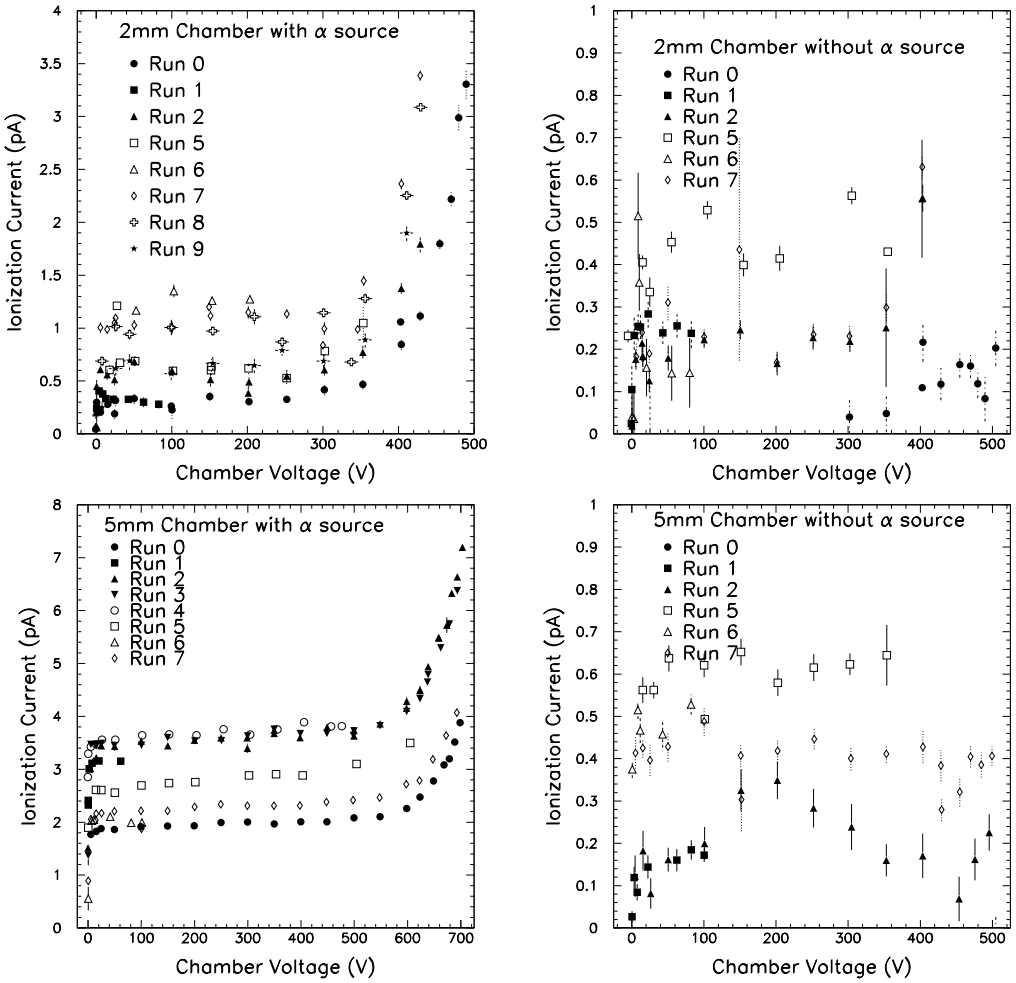

Figure 4.6: Plateau curves for 2mm and 5mm chambers flushed with Helium gas for 7 different neutron source placements. Ionization current due to neutrons is the plateau value minus the ionization current due to α's for chambers with an α source. For a given chamber, each run corresponds to a neutron flux as indicated in Table 4.1.

respectively). Thus, we infer the ionization per neutron pathlength through the chamber Helium gas:

$$1.08 \pm 0.15 \text{ ionizations / cm / neutron.}$$

This may be compared with the ionization per centimeter pathlength of fast charged particles through Helium gas. Given $dE/dx \sim 500$ eV/cm for 100 GeV protons[52], and $w = 32$ eV per ion pair in chamber Helium,[3] charged particles are expected to deposit of order 16 ionizations/cm in He gas.

4.6.2 Argon Results

Figure 4.8 shows the plateau curves for all the runs taken with Argon gas. In these runs, the voltage was always varied from negative to positive polarity, so the full voltage scan is shown. Tables 4.10 and 4.11 summarize the plateau values for four chambers during all the Argon runs.

The neutron-induced ionization current is plotted *vs.* neutron flux in Figure 4.9. The uncertainties in the neutron-induced ionization current are smaller than in Figure 4.7 because the voltage has been scanned from negative to positive polarity in every run of the Argon data, allowing a more accurate determination of "zero" ionization current.

We have fit the data in Figure 4.9 to find the average neutron-induced ionization in Argon. The fit constrained to go through the origin gives slope values:

$$3.7 \pm 0.4 \text{ ionizations / neutron (5 mm chambers)}$$
$$2.4 \pm 0.3 \text{ ionizations / neutron (2 mm chambers)}$$

[3] The accepted value of 42 eV for pure Helium [51] is drastically reduced for gas in which as much as 10^{-4} impurity levels exist [53].

Thus, we infer the ionization per neutron pathlength through the chamber Argon gas:

$$9.6 \pm 2.4 \text{ ionizations / cm / neutron.}$$

If Argon is used to fill the muon monitors, then the above ionizations/cm/neutron background may be compared with the expected ionization/cm expected for charged particles, *viz* 5 GeV muons, which produce approximately 120 ionizations/cm in pure Argon. As with the results in Helium gas, the background is less than 10%.

2mm Chamber with α source					
Run No.	I^+ (pA)	I^- (pA)	$\langle I \rangle$ (pA)	I Due to n (pA)	n Flux (pA)
0	.31	–	.32 ± 0.15	0	0(0)
1	.29	-.29	.29 ± 0.04	-0.03 ± 0.16	0.10(0.21)
2	.55	–	.55 ± 0.20	0.23 ± 0.25	0.28(0.41)
5	.64	-.67	.66 ± 0.07	0.34 ± 0.17	1.26(1.46)
6	1.19	-1.33	1.25 ± 0.15	0.93 ± 0.21	2.23(2.84)
7	1.05	–	1.09 ± 0.15	0.77 ± 0.21	2.53(3.04)
8	0.99		1.03 ± 0.30	0.71 ± 0.34	3.12(4.00)
9		-0.75	-.72 ± 0.30	0.40 ± 0.34	3.12(4.00)
2mm Chamber without α source					
Run No.	I^+ (pA)	I^- (pA)	$\langle I \rangle$ (pA)	I Due to n (pA)	n Flux (pA)
0	0	0	0	0	0(0)
1	0.33	-0.15	0.24 ± 0.05	0.24 ± 0.05	0.83(0.92)
2	0.33	–	0.24 ± 0.15	0.24 ± 0.15	0.94(1.04)
5	0.19	-.67	0.43 ± 0.10	0.43 ± 0.10	1.25(1.46)
6	0.13	-.16	0.14 ± 0.05	0.14 ± 0.05	0.15(.36)
7	0.18	–	0.20 ± 0.10	0.20 ± 0.10	0.17(0.41)

Table 4.5: Observed ionization currents due to neutrons and expected neutron fluxes in the 2 mm gap chambers flushed with Helium gas. The seven runs refer to different neutron source placements. The tabulated quantities are explained in the text.

5mm Chamber with α source					
Run No.	I^+ (pA)	I^- (pA)	$\langle I \rangle$ (pA)	I Due to n (pA)	n Flux (pA)
0	3.27	-0.61	1.93 ± 0.10	0	0(0)
1	5.41	-0.80	3.10 ± 0.05	1.18 ± 0.11	2.23(2.84)
2	6.40	–	3.67 ± 0.10	1.74 ± 0.14	2.53(3.04)
3	6.22		3.57 ± 0.30	1.64 ± 0.32	3.12(4.00)
4		-.99	3.84 ± 0.30	1.91 ± 0.32	3.12(4.00)
5	4.90	-0.74	2.82 ± 0.10	0.89 ± 0.16	1.26(1.46)
6	3.63	-0.46	2.04 ± 0.15	0.12 ± 0.18	0.10(0.21)
7	4.15	–	2.34 ± .07	0.41 ± 0.12	0.28(0.41)
5mm Chamber without α source					
Run No.	I^+ (pA)	I^- (pA)	$\langle I \rangle$ (pA)	I Due to n (pA)	n Flux (pA)
0	0	0	0	0	0(0)
1	0.31	-0.10	.20 ± .05	.20 ± .05	0.15(0.36)
2	0.25	–	0.17 ± 0.15	0.17 ± 0.15	0.17(0.41)
5	0.86	-0.35	.61 ± 0.20	0.61 ± 0.20	1.26(1.46)
6	0.61	-0.40	0.50 ± 0.07	0.50 ± 0.07	0.83(0.92)
7	0.50	–	0.41 ± 0.07	0.41 ± 0.07	0.94(1.04)

Table 4.6: Observed ionization currents due to neutrons and expected neutron fluxes in the 5 mm gap chambers flushed with Helium gas. The seven runs refer to different neutron source placements. The tabulated quantities are explained in the text.

Chamber Gap	Observed Ion Pairs per Neutron	
	He Gas	Ar Gas
2 mm	0.26 ± 0.07	2.4 ± 0.3
5 mm	0.49 ± 0.06	3.7 ± 0.4
1 cm[a]	1.08 ± 0.15	9.6 ± 2.4

[a]Inferred from 2, 5 mm gap chambers.

Table 4.7: Ionization current per neutron obtained from fits of the data in Figures 4.9 and 4.7. The fitted slopes are equivalent to ion pairs per neutron.

Element	A	Z	σ_{tot} (b)[54] $E_n = 2, 5, 10$ MeV	$\overline{E_R}/E_n$	Particle Range in Media He (mm)	Ar (mm)	Pt (μm)
He	4	2	4.1, 2.3, 1.5	0.320	47	–	–
Al	27	12	3.2, 2.3, 1.7	0.069	12.3	1.9	0.3
Ar	40	18	4.3, 3.4, 2.2	0.048	–	1.2	–
Ag	108	47	6.5, 4.1, 4.4	0.018	2.6	0.27	0.1
Pt	196	78	5.8, 6.6, 5.2	0.010	0.74	0.13	0.1

Table 4.8: Elastic scattering data for materials found in our ionization chambers, The total cross sections are given for the range 2-10 MeV. The average recoil energy is provided as a portion of the neutron's energy. Range is calculated for the typical fully-ionized recoil nucleus of a 5 MeV neutron in both gaseous Helium and Argon and in Platinum using data from [47] and scaling laws from [55].

Chamber Gap	Expected Ion Pairs per Neutron					
	He Gas			Ar Gas		
	n's	γ's	Total	n's	γ's	Total
2 mm	0.07	0.18	0.25	0.15	1.8	2.0
5 mm	0.18	0.44	0.62	0.37	4.4	4.8
1 cm	0.35	0.84	1.19	0.75	8.4	9.2

Table 4.9: Expected ionization current per neutron decay from the PuBe source, as described in Section 4.5. The estimates include the ion pairs produced by elastic scatters of neutrons in the chamber gas (n's), as well as those arising from Compton scatters of subsequent cascade γ's from the PuBe source (γ's). The total expected signals may be compared to the observed values listed in Table 4.7.

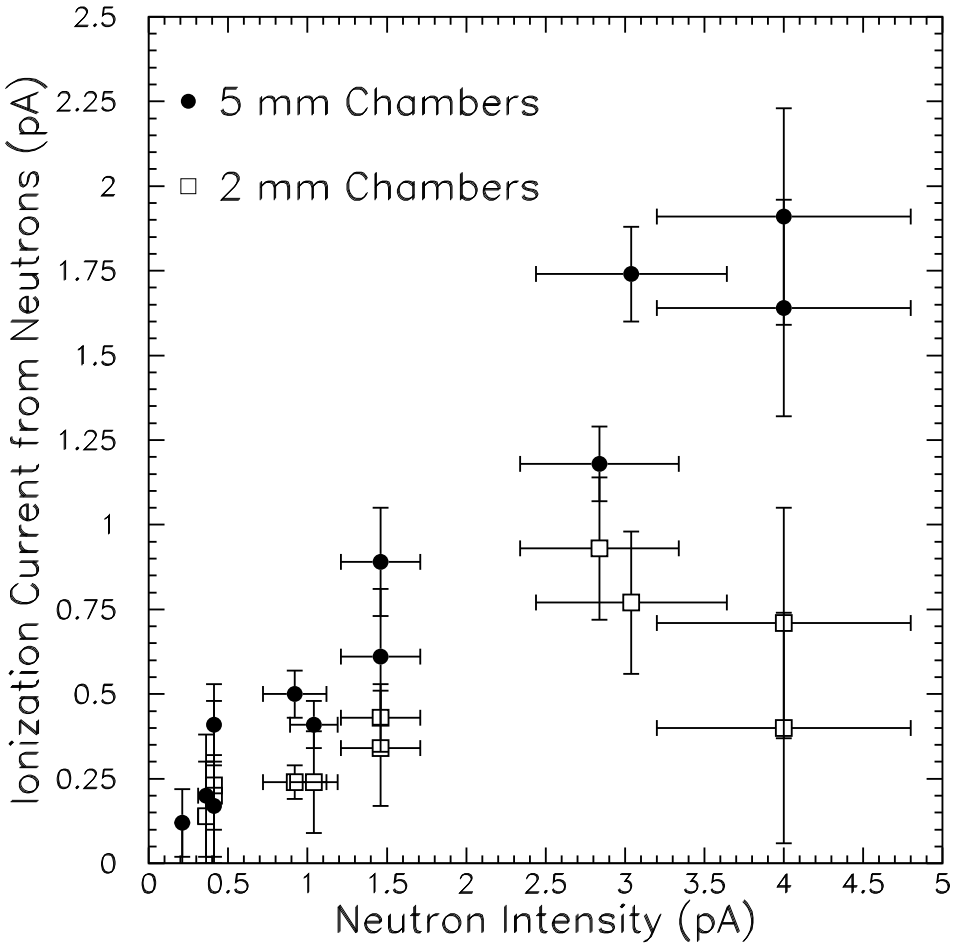

Figure 4.7: Graph of the ionization current induced in Helium gas by neutrons as a function of neutron intensity. The neutron intensity is in units of 'pA', where 1 pA = 6.2×10^6 neutrons / sec. The data are taken from Tables 4.5 and 4.6. The neutron fluxes have been weighted by an additional cosine factor to account for the differing pathlengths of the neutrons through the ion chamber gas.

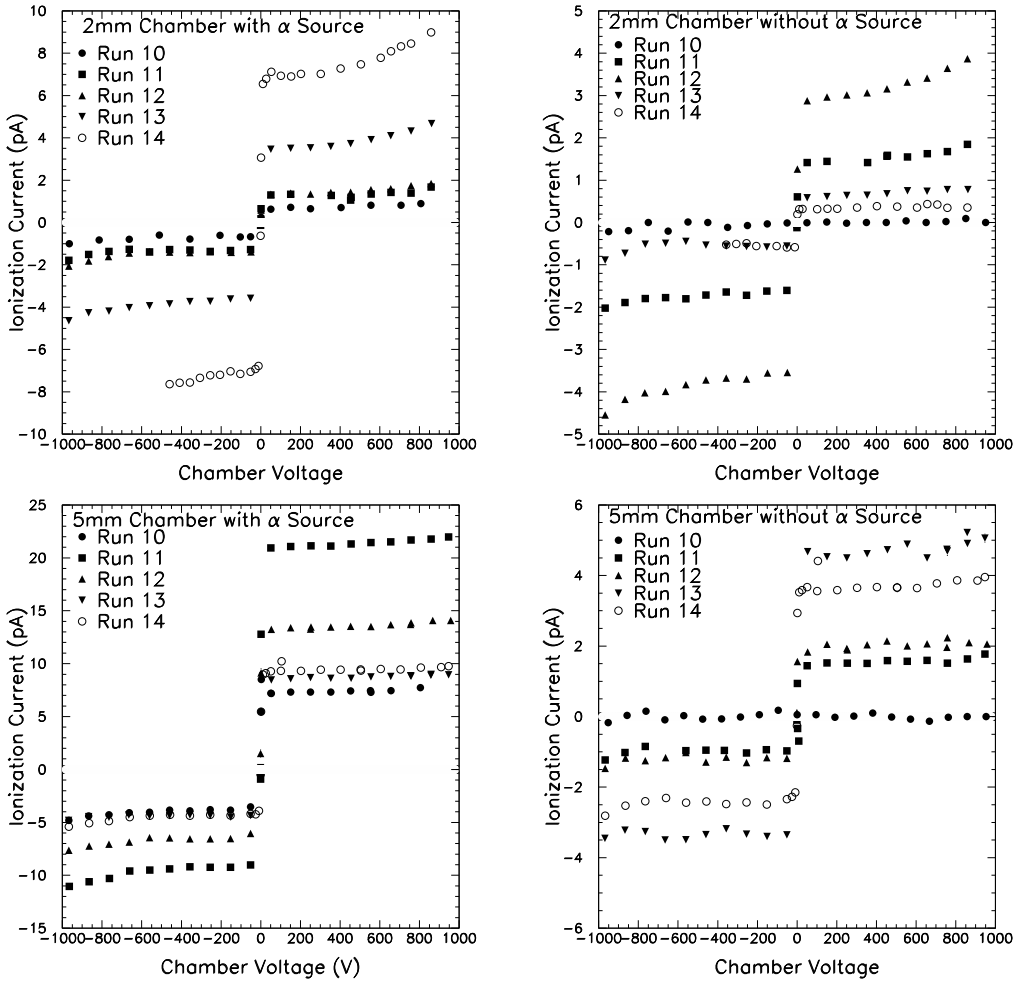

Figure 4.8: Plateau curves for 2mm and 5mm chambers flushed with Argon gas for 4 different neutron source placements. Ionization current due to neutrons is the plateau value minus the ionization current due to α's for chambers with an α source. For a given chamber, each run corresponds to a neutron flux as indicated in Tables 4.10 and 4.11.

2mm Chamber with α source					
Run No.	I^+ (pA)	I^- (pA)	$\langle I \rangle$ (pA)	I Due to n (pA)	n Flux (pA)
10	0.63	0.68	0.66 ± 0.10	0	0(0)
11	1.28	-1.36	1.32 ± 0.03	0.67 ± 0.10	0.10(0.21)
12	1.39	-1.39	1.39 ± 0.05	0.74 ± 0.11	0.28(0.66)
13	3.40	-3.78	3.59 ± 0.10	2.94 ± 0.14	1.26(1.46)
14	6.70	-7.23	6.97 ± 0.05	6.31 ± 0.11	2.23(2.84)
2mm Chamber without α source					
Run No.	I^+ (pA)	I^- (pA)	$\langle I \rangle$ (pA)	I Due to n (pA)	n Flux (pA)
10	0	0	0	0	0(0)
11	1.47	-1.67	1.57 ± 0.03	1.57 ± 0.03	0.83(0.92)
12	3.00	-3.67	3.33 ± 0.06	3.33 ± 0.06	1.25(1.46)
13	0.63	-.56	0.60 ± 0.10	0.60 ± 0.10	0.28(0.66)
14	0.50	-.60	0.55 ± 0.02	0.55 ± 0.02	0.15(.36)

Table 4.10: Observed ionization currents due to neutrons and expected neutron fluxes in the 2 mm gap chambers flushed with Argon gas.

5mm Chamber with α source					
Run No.	I^+ (pA)	I^- (pA)	$\langle I \rangle$ (pA)	I Due to n (pA)	n Flux (pA)
10	7.25	-3.82	5.54 ± 0.07	0	0(0)
11	21.11	-9.65	15.38 ± 0.07	9.84 ± 0.10	2.23(2.84)
12	13.41	-6.27	9.84 ± 0.07	4.30 ± 0.10	1.26(1.46)
13	8.60	-4.39	6.50 ± 0.10	0.96 ± 0.13	0.28(0.66)
14	9.30	-4.30	6.80 ± 0.05	1.27 ± 0.10	0.10(0.21)
5mm Chamber without α source					
Run No.	I^+ (pA)	I^- (pA)	$\langle I \rangle$ (pA)	I Due to n (pA)	n Flux (pA)
10	0	0	0	0	0(0)
11	1.58	-1.01	1.30 ± 0.10	1.30 ± 0.10	0.15(0.36)
12	2.04	-1.18	1.61 ± 0.07	1.61 ± 0.07	0.28(0.66)
13	4.34	-3.30	3.82 ± 0.05	3.82 ± 0.05	1.26(1.46)
14	3.60	-2.42	3.01 ± 0.05	3.01 ± 0.05	0.83(0.92)

Table 4.11: Observed ionization currents due to neutrons and expected neutron fluxes in the 5 mm gap chambers flushed with Argon gas.

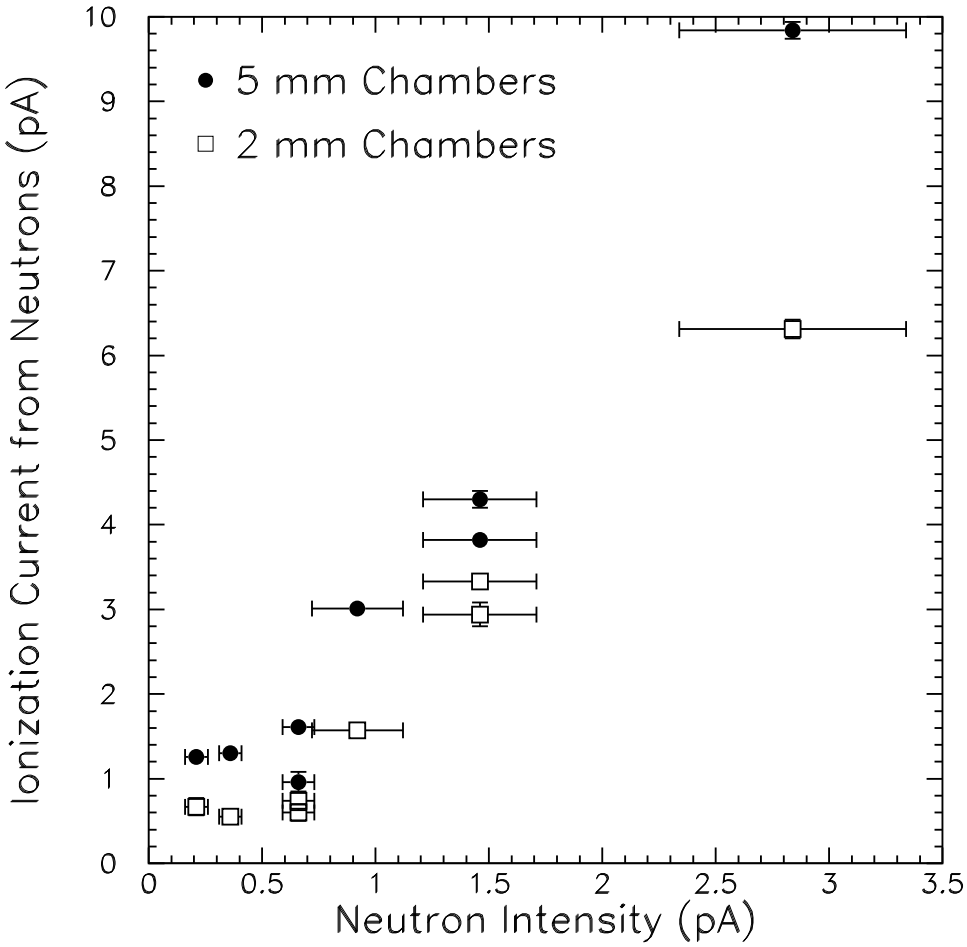

Figure 4.9: Graph of the ionization current induced in Argon gas by neutrons as a function of neutron intensity. The neutron intensity is in units of 'pA', where 1 pA = 6.2×10^6 neutrons / sec. The data are taken from Tables 4.10 and 4.11. The neutron fluxes have been weighted by an additional cosine factor to account for the differing pathlengths of the neutrons through the ion chamber gas.

4.7 Conclusions

We have studied the signals induced in ionization chambers exposed to low energy (1-10 MeV) neutrons in the form of a PuBe source. An ionization current from the source is observed whose magnitude is (1.1±0.2±0.1) ionizations/neutron/cm in the Helium gas, and (9.6±2.4±1.0) ionizations/neutron/cm in the Argon gas, based on our observations at several neutron fluences and two chamber gas gaps. The first uncertainty is that due to the estimate of the neutron fluxes, while the last uncertainty is due to the PuBe source activity into neutrons.

Our measurements of the PuBe source-induced ionization are limited in precision because of the large number of γ rays from the PuBe sources. However, the neutron-specific signal inferred is consistent with that expected from pure elastic scattering of the neutrons in the chamber gas: 0.35 ion pairs per neutron per centimeter in He, and 0.75 ion pairs per neutron per centimeter in Argon.

Our measurements indicate the NuMI beam monitors will have a background signal of order 20-30% from neutron interactions in the chambers. While the yield of ion pairs per neutron is only 2-3% for that of charged particles (assuming elastic scattering), `GEANT`[59]-based Monte Carlo estimates indicate that the hadron monitor and the first muon monitor will be exposed to the order of 10 times as many neutrons as signal particles (protons in the case of the Hadron monitor and muons in the case of the muon monitors). The neutron background signal will be much less correllated spatially with beam misalignments than the signal, so its effect will be important to model.

Chapter 5

In-Beam Performance

5.1 Introduction

The NuMI beamline began regular operation in March of 2005 and proceeded until February of 2006. Over that period of time, 1.4×10^{20} protons were delivered to the NuMI target. The Hadron Monitor saw charged particle fluxes of up to $10^9/\text{cm}^2/\text{spill}$, and Alcove 1 saw fluxes of up to $10^7/\text{cm}^2/\text{spill}$. The effects of high intensity charged particle fluxes on prototype chambers have been studied in [30]. The characteristic responses of the hadron and muon monitors were studied in relation to horn performance, target integrity, component alignment, and beam stability. The hadron and muon monitors were also useful in diagnosing target problems and monitoring the NuMI beam. This chapter details the results of the hadron and muon monitor studies, and demonstrates their utility during NuMI operation.

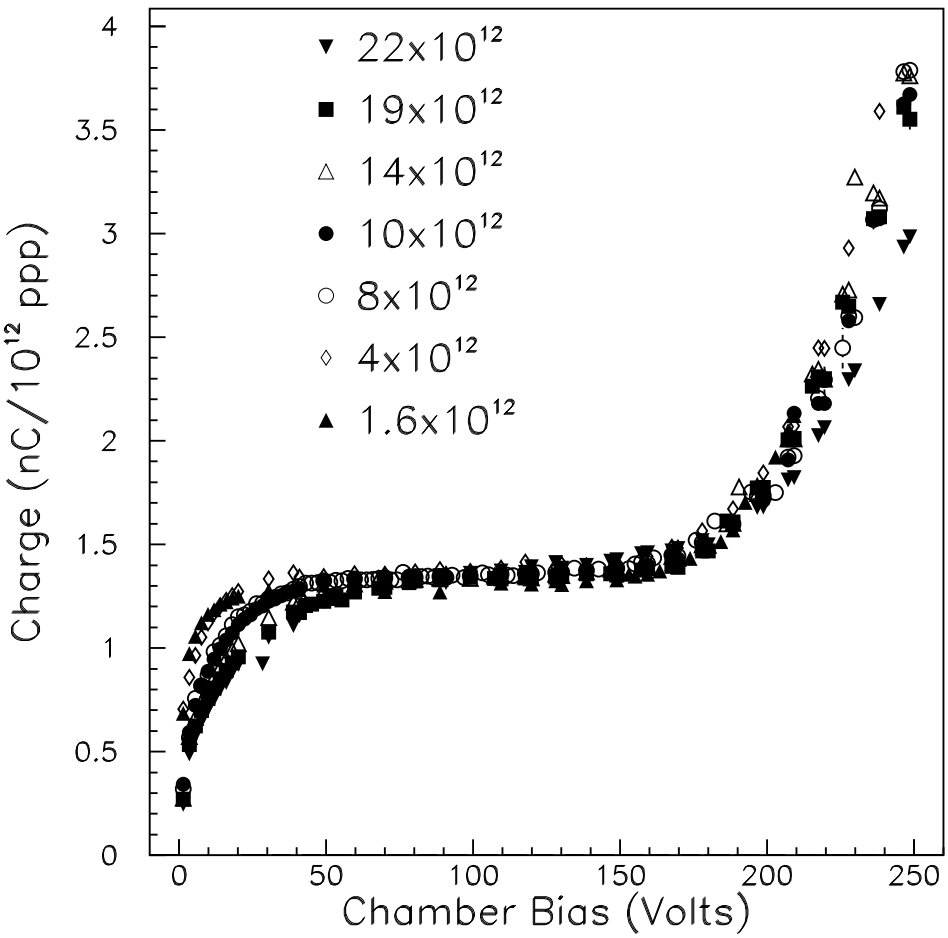

Figure 5.1: Plateau curves of the Hadron monitor center pixel signal divided by beam current as the applied bias is ramped increased from 0 to 250 V. The different curves correspond to beam intensities ranging from 1.6E12 ppp to 19E12 ppp.

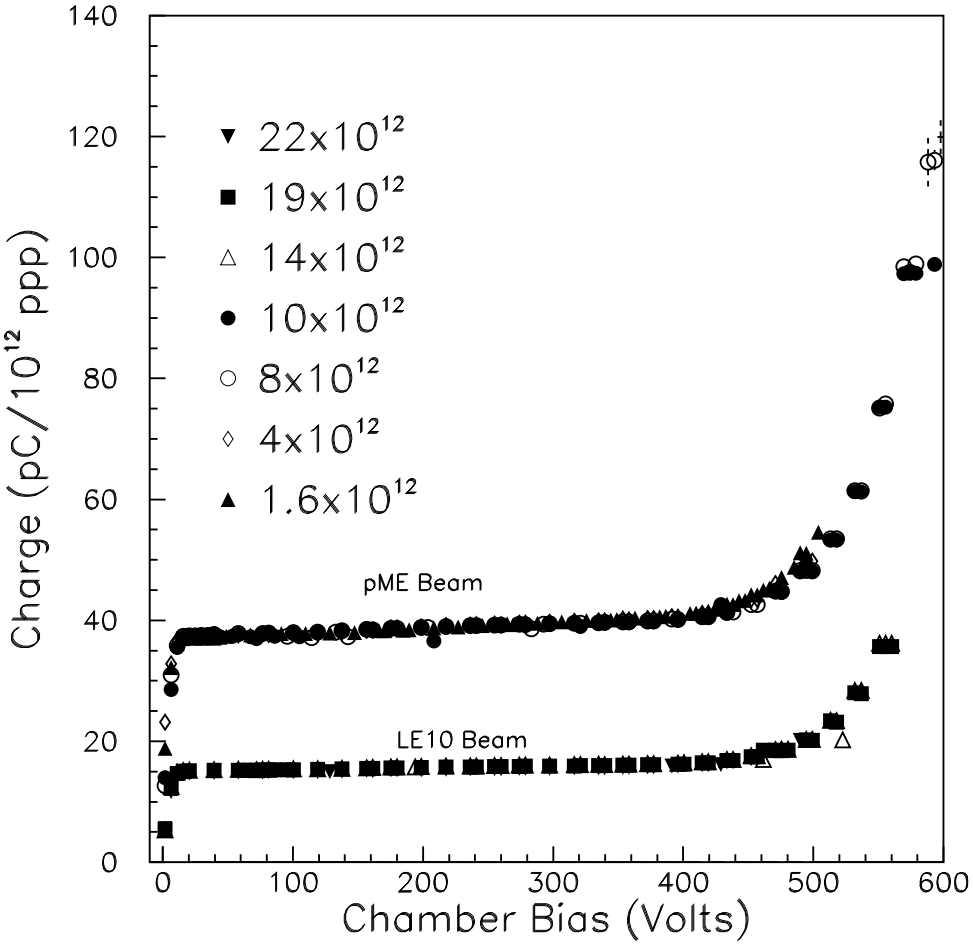

Figure 5.2: Plateau curves of the Muon monitor center pixel signal divided by beam current as the applied bias is ramped increased from 0 to 500-600 V. The different curves correspond to beam intensities ranging from 1.6E12 ppp to 19E12 ppp.

5.2 Chamber Performance

It is important to choose an applied bias voltage that collects all of the ionized charge without amplification. Operating the chambers with gain>1 could defeat the calibration from Chapter 3. Also, high charged particle fluxes can cause space charge build-up that screens the applied fields. When operating at a point of gain, furthermore, signals are sensitive to the applied bias voltage as well as pressure and temperature. If the bias voltage is too low, ionized charge will recombine.

Studies have been conducted to characterize the ion-chamber response of the hadron and muon monitors to in-beam running conditions. Figure 5.1 shows several plateau curves of the hadron monitor center pixel obtained at different proton intensities on target. The shapes of both the turn-on and the gain vary with proton intensity. At 4×10^{12}ppp, the plateau begins at about 30 volts as the applied bias is sufficient to collect all of the ionized charge in the chamber gap. However, at 22×10^{12}ppp, total charge collection is obtained at 90V because screening effectively lowers the applied fields seen by the ionized charge. Space-charge buildup also reduces the gain of the chamber as charges see effectively lower applied fields. An operating voltage of 130V is chosen.

Figure 5.2 shows plateau curves for the Muon Monitor in Alcove 1. The two sets of curves correspond to two different modes of running, one in the ME configuration and the other in the LE-10 configuration. For all beam intensities, plateau is reached at an applied bias of about 15V, which indicates that the muon monitor is not susceptible to space-charge effects. An operating voltage of 300V is chosen for all three muon monitors.

There is a slope on the plateau of curves of up to 5% over 300V in the muon monitors and 1.5% over 100V in the hadron monitor. The slope is

independent of proton intensity. This is probably an effect of stray ionization collecting on the signal lines.[14]

Linearity studies have been performed to assess the effects of space charge at the applied bias of 130V (300V) for the Hadron (Muon) monitor. Figures 5.3 and 5.4 show the results of the these studies. Also shown is data from a period of running during which the applied bias for the Hadron Monitor was 190V. During this time, the chambers actually operate near the edge of the amplification region. In all cases, the monitors are shown to be linear up to 25×10^{12}. The data is corrected for variations in pressure, as described in the next section.

The corresponding residuals for the linearity studies are shown in Figures 5.5 and 5.6. The hadron monitor center pixel shows no indication of charge collection inefficiency as a function of protons on target. Alcove 1 shows a drop in total charge collected per 10^{12} protons of approximately 4.5%. The slope in the plateau curves of the Alcove 1 pixels contributes to this non-linear response to proton intensity since screening by ionized charge reduces the effective bias "'seen"' in the gap.

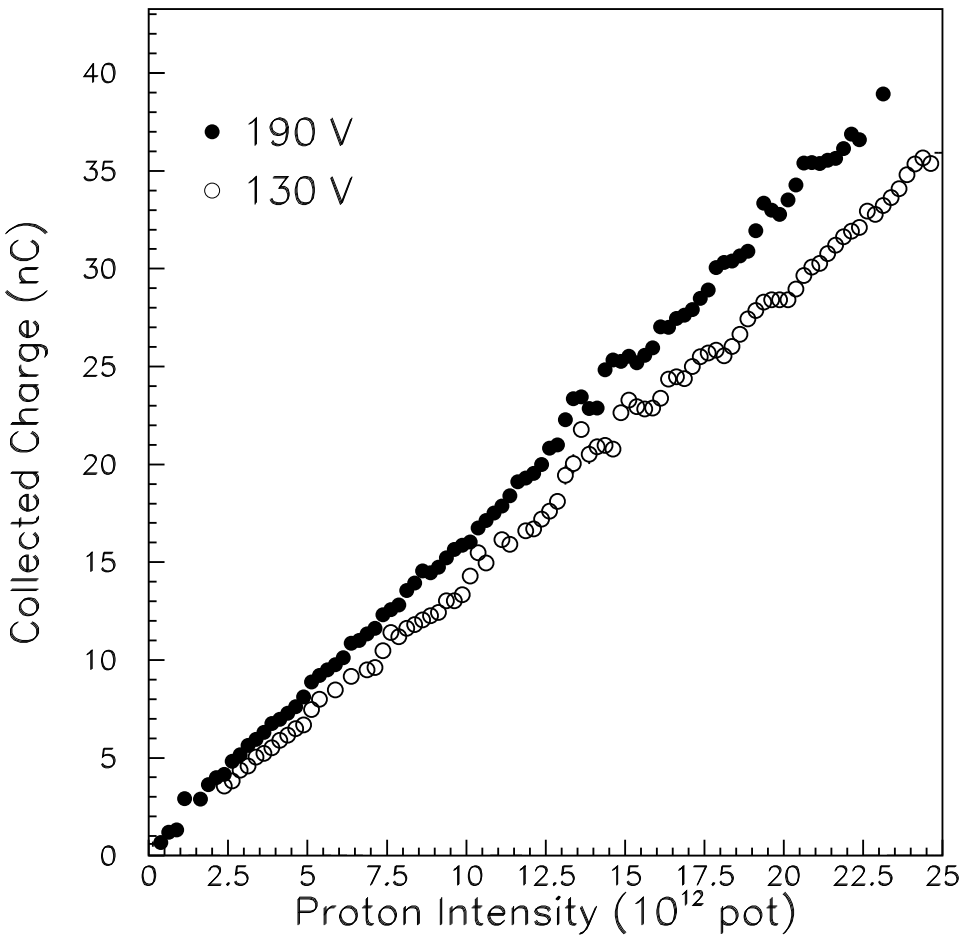

Figure 5.3: Shown is the center pixel charge in the hadron monitor as a function of proton intensity on target.

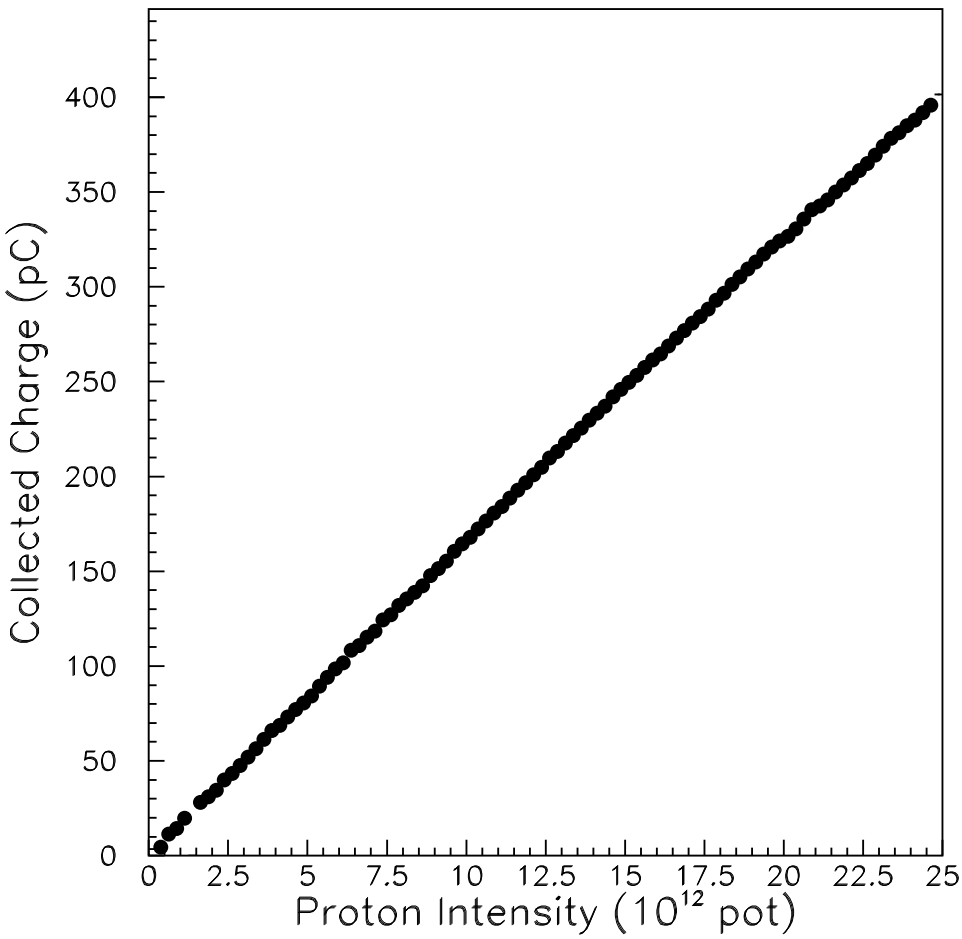

Figure 5.4: Shown is the center pixel charge in alcove 1 as a function of proton intensity on target.

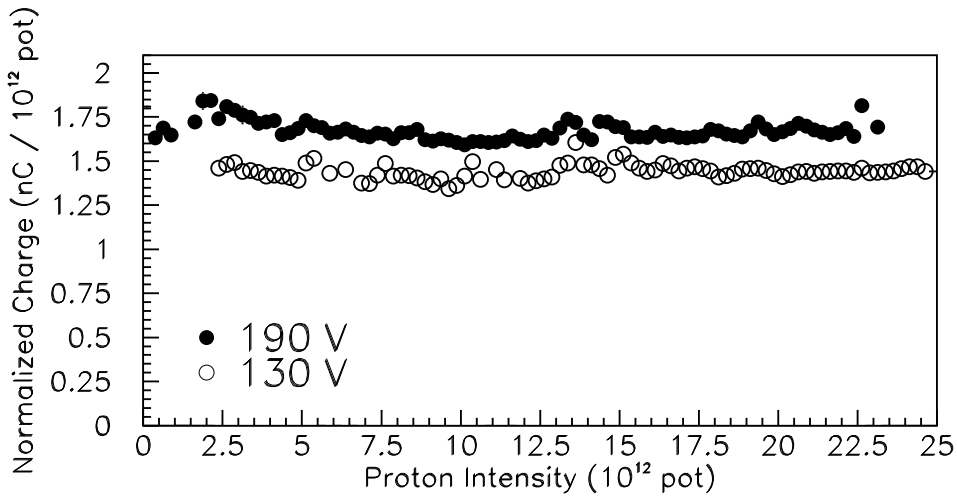

Figure 5.5: Shown are the residuals of the data plotted in Fig 5.3.

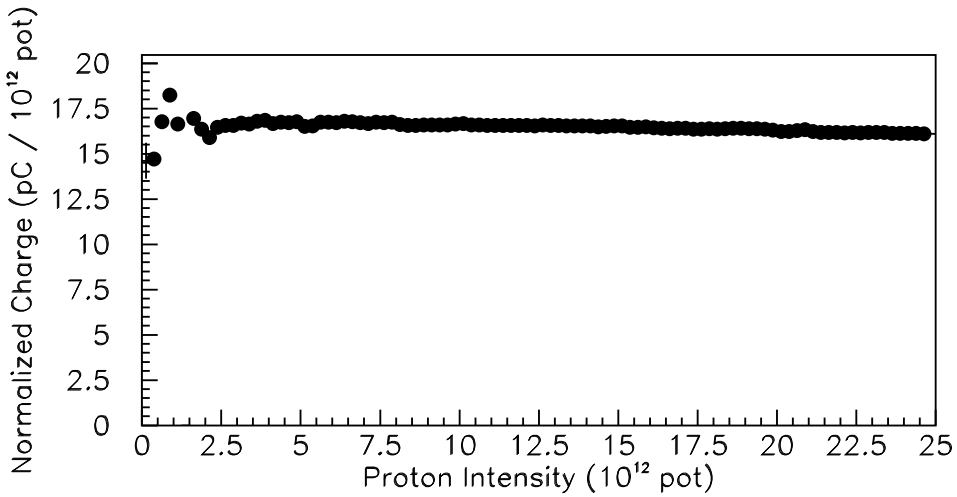

Figure 5.6: Shown are the residuals of the data plotted in Fig 5.4.

5.3 Signal Response to Environmental changes

The signal response of an ion chamber depends on the density of the gas medium. This in turn depends on the the pressure of the enclosed gas volume. The gas system in place for the hadron and muon monitors exhausts into the air, and so the pressure of the gas in the instrumentation varies with the ambient pressure. The pressure in the gas line is measured by a pressure transducer installed at the gas distribution rack [**?**].

Pressure swings of up to 20 torr over a few days have been observed in the gas lines. Figures 5.7 and 5.8 show the intensities of the hadron monitor and the muon monitors as a function of pressure in the gas line. All the monitors evidence a linear variation with pressure as expected. At 780 torr, one expects a fractional change in signal response of .13%/torr, which suggests a slope of .83 pC/10^{12}ppp/torr for alcove 1, and .137 pC/10^{12}ppp/torr for alcove 2. The variation observed is within 10% of the calculated value.

The hadron monitor also shows a minor variation with pressure on the order of .05%/torr. With an applied bias of 190V, where the hadron monitor operates in a region of modest gain, the signal actually decreases with pressure. This suggests that at greater densities, the gain of the chamber is supressed. Even though more ionization is created in the gap, a smaller fraction reionizes the gas, or alternatively, more reionized particles recombine. The results are summarized in table 5.1.

5.4 Long Term Beam Stability

Intensity, centroid, and RMS determinations by the beam monitors provide several measures to diagnose beam quality. Shown in Figures 5.9-5.12 are

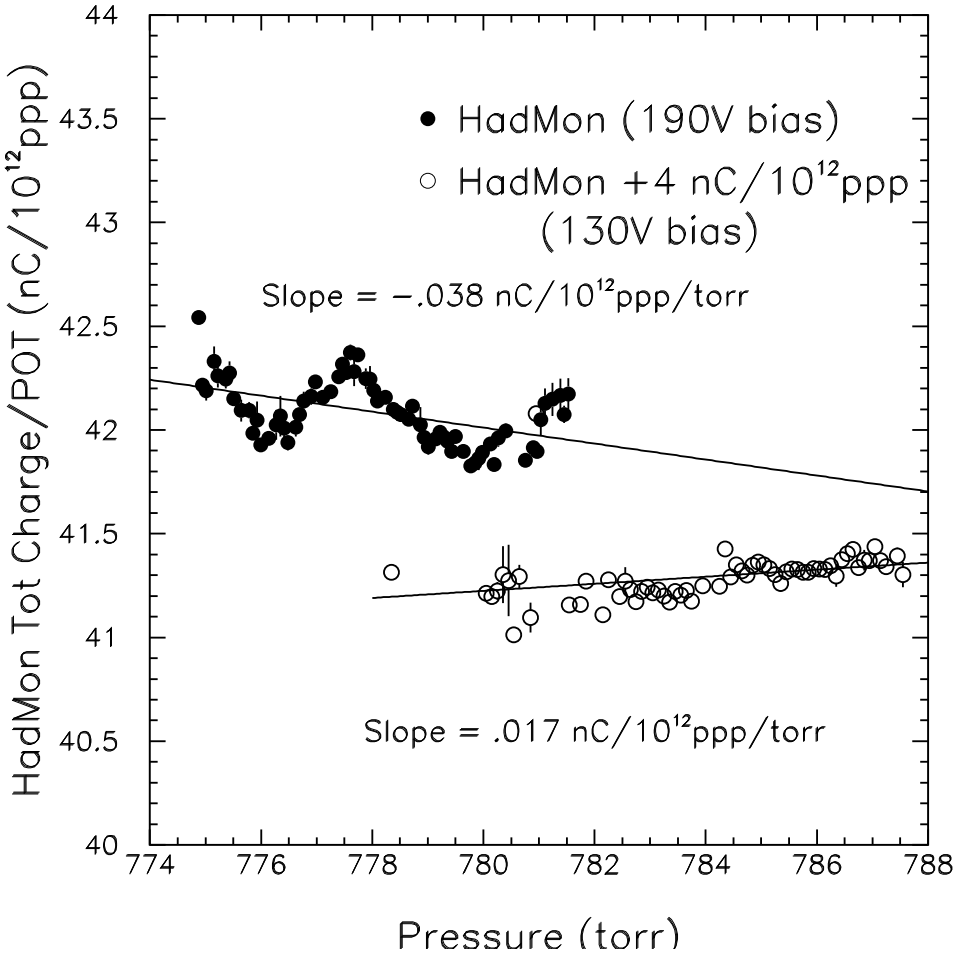

Figure 5.7: Hadron Monitor signal as a function of gas pressure.

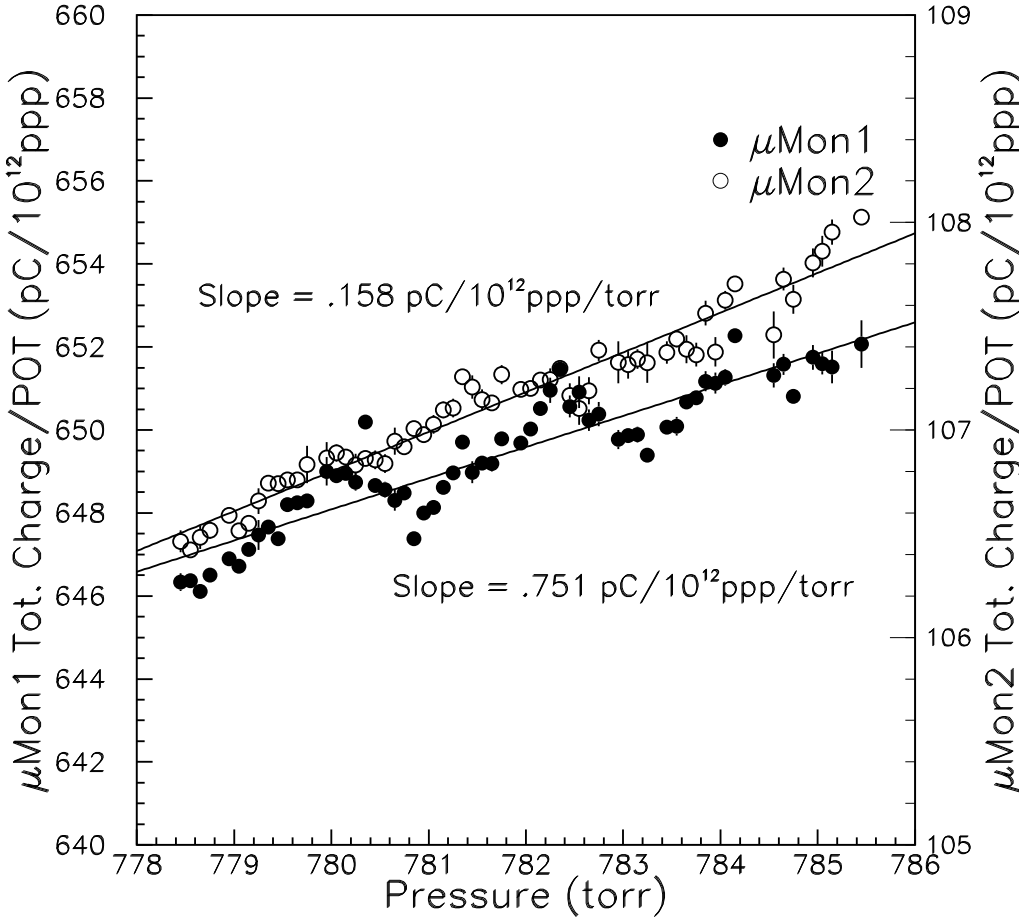

Figure 5.8: Muon Monitor 1 signal as a function of gas pressure.

1D projections of hadron and muon monitor signals for a typical spill and an errant spill in which the beam struck the baffle. The neutrino spectrum of the errant spill differs significantly from a nominal spill, as indicated by the differences in the Muon Monitor profiles. The baffle is located upstream of the target, and so beam on baffle produces pions further from the horns. This yields a higher energy secondary beam.

The hadron monitor can quickly diagnose an errant spill. The aberrant spill produces only 10% of the nominal beam signal. The measured centroid is 9"' high and 4"' beam right with respect to nominal. Also, the beam sigma at the hadron monitor increases by a factor 2.

The total charge in the hadron monitor and the alcoves is shown in Figures 5.13-5.16 over a period of a few hundred days. Also shown is the data after corrections are applied for pressure variations in the gas supplying the monitor. In the absence of the corrections, variations on the order of 3-4% can be seen in the hadron monitor and the muon monitors.

In the Hadron Monitor, the signal variation $\sim$2% after pressure corrections. The period between 320 and 330 days is improved once corrections are applied, but it still stands out as a period of unstable beam.

In figures 5.14 to 5.16 the signal in the alcoves shows a 90 day period of stable operation. Evident in the raw data are swings in signal on the 3-4% level over the course of 2-3. The data in red corresponds to pressure-corrected data, and reduces the variations to long term 1-2% changes. The pressure correction is on the order of .13%/torr, which corresponds to .05pA/torr in Alcove 3. Therefore, much of Alcove 3's response to pressure is lost in the noise.

The horizontal and vertical centroid positions as measured by the hadron monitor and muon monitors are given in Figures 5.17-5.20. In Figure 5.17, the

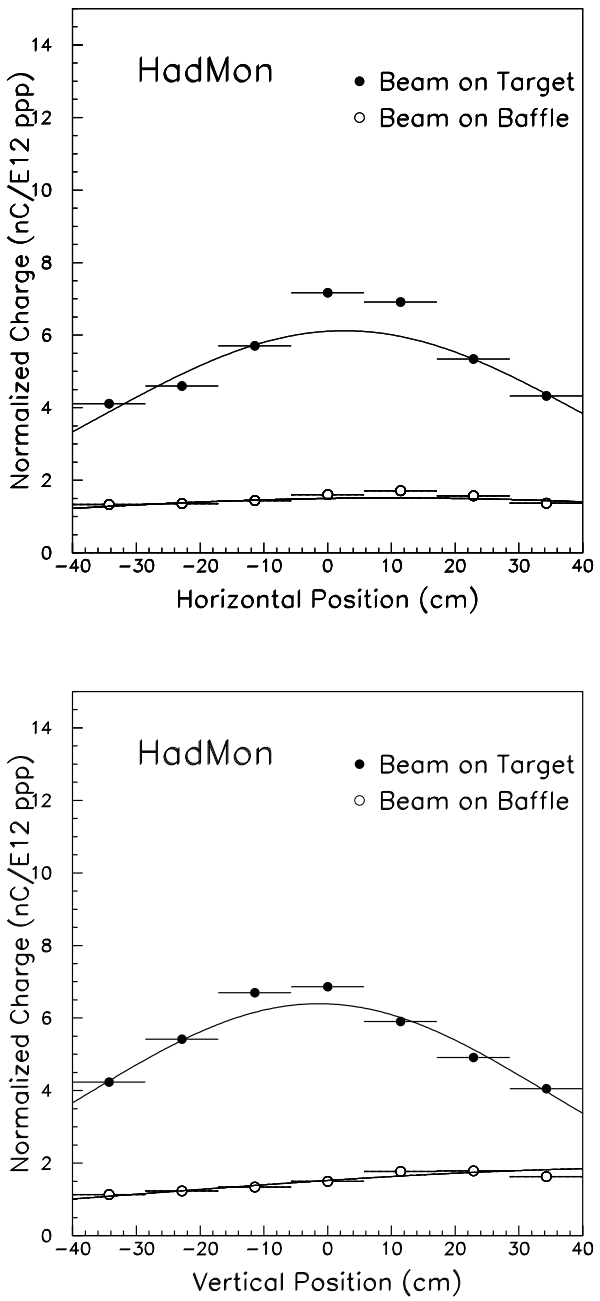

Figure 5.9: Shown are the 1-D projections of signals in the Hadron monitor for an average spill in which beam hits the center of the target and for a spill in which the beam struck the baffle.

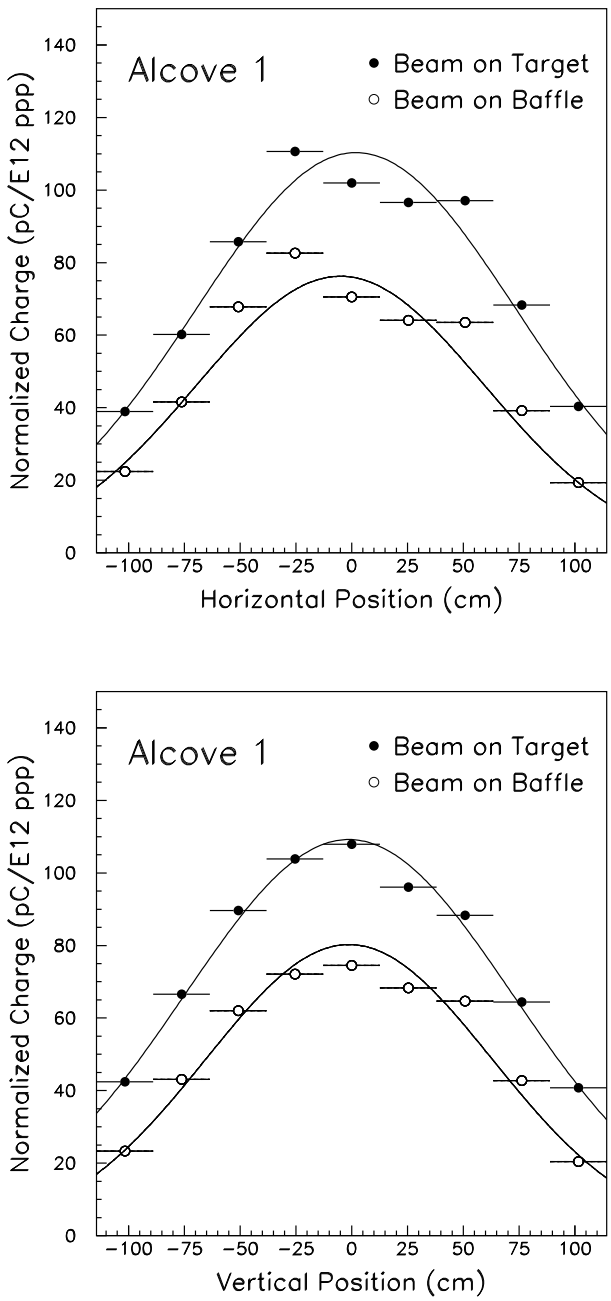

Figure 5.10: Shown are the horizontal 1-D projections of signals in Alcove 1 for an average spill in which beam hits the center of the target and for a spill in which the beam struck the baffle.

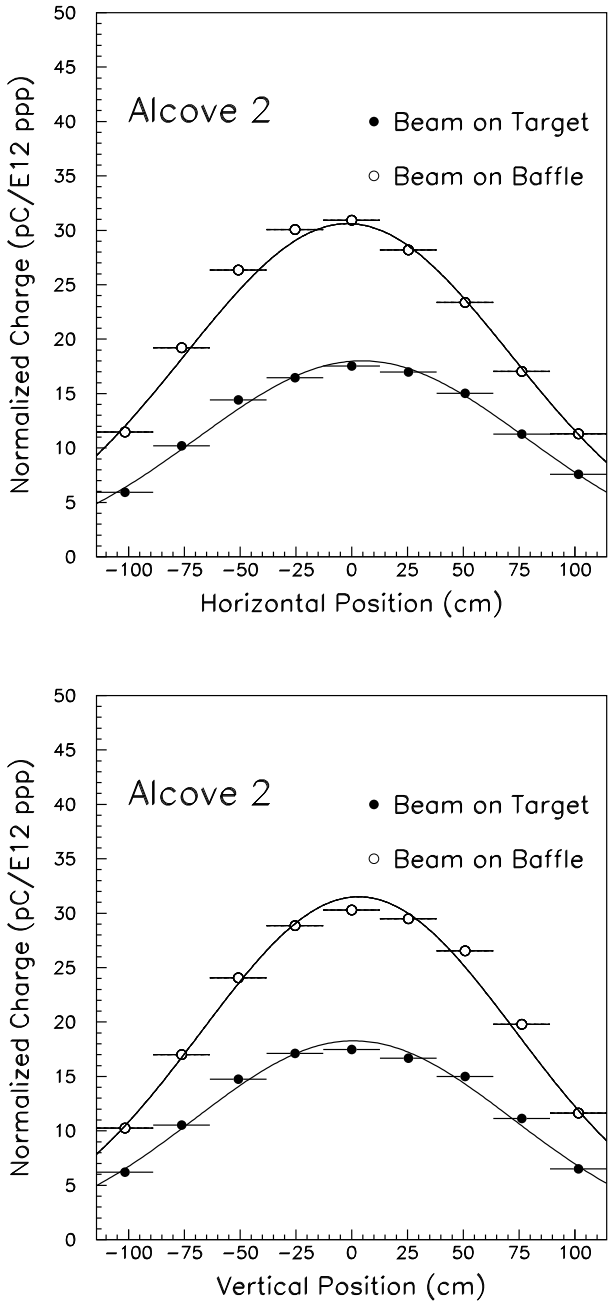

Figure 5.11: Shown are the horizontal 1-D projections of signals in Alcove 2 for an average spill in which beam hits the center of the target and for a spill in which the beam struck the baffle.

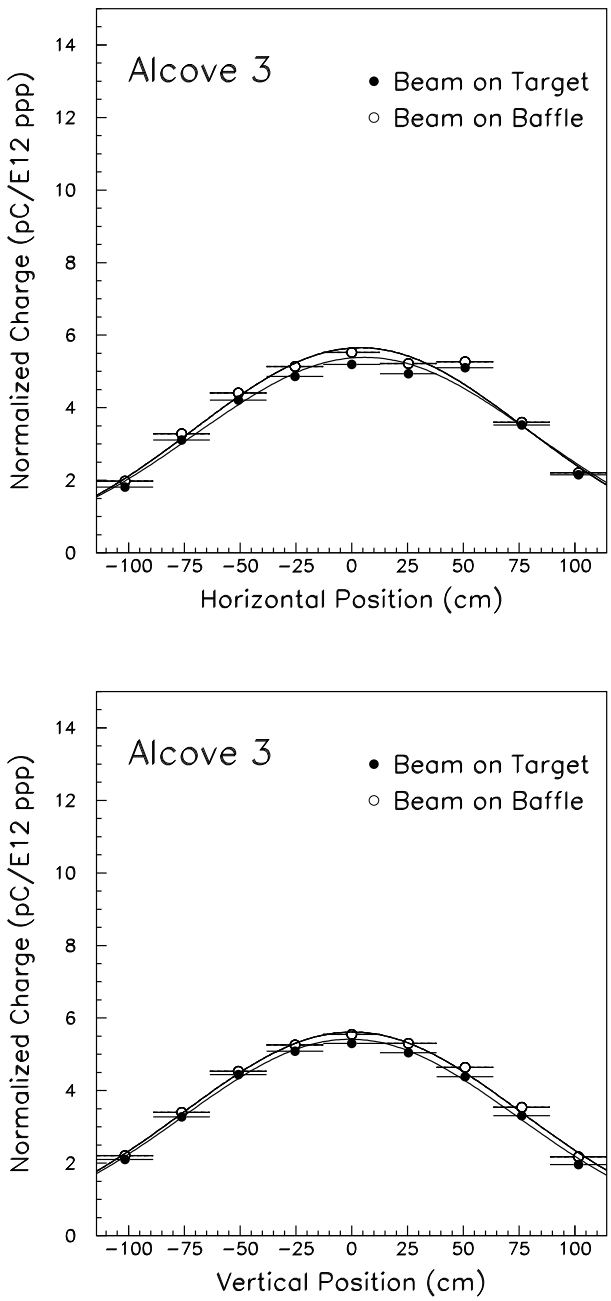

Figure 5.12: Shown are the horizontal 1-D projections of signals in Alcove 3 for an average spill in which beam hits the center of the target and for a spill in which the beam struck the baffle.

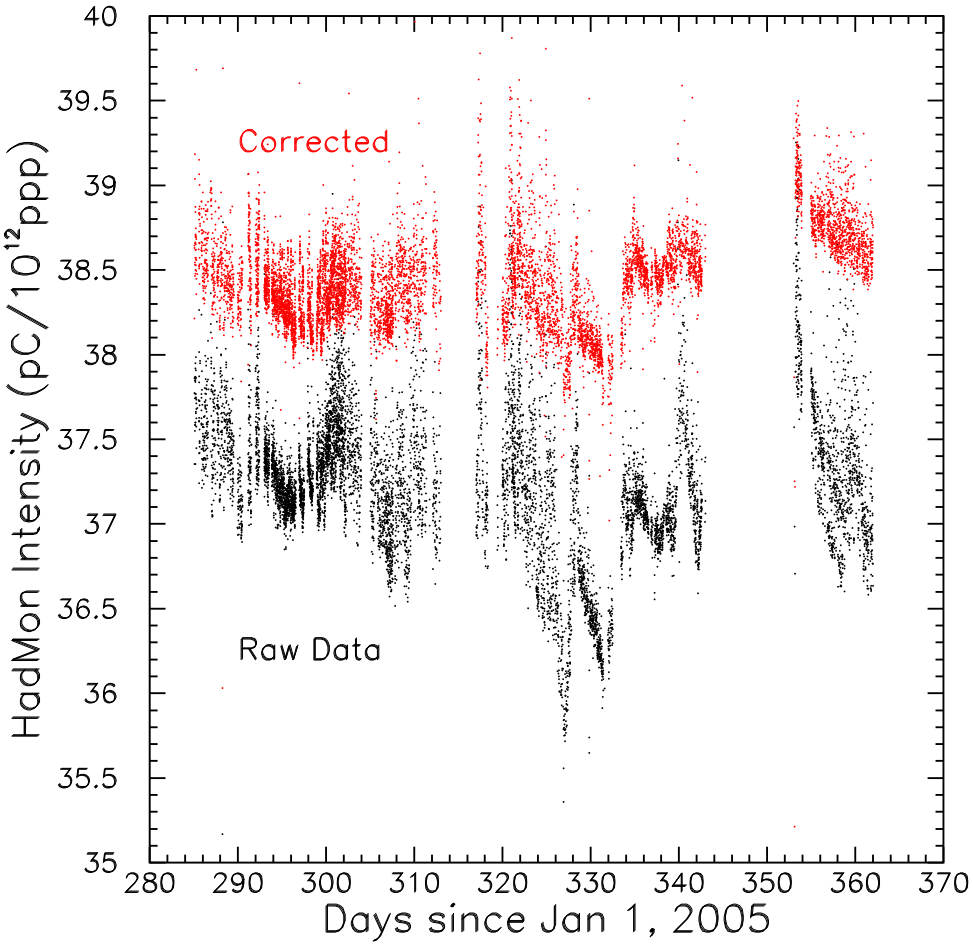

Figure 5.13: Measured total intensity in the Hadron monitor over the period from July 29 to Feb 25, 2006.

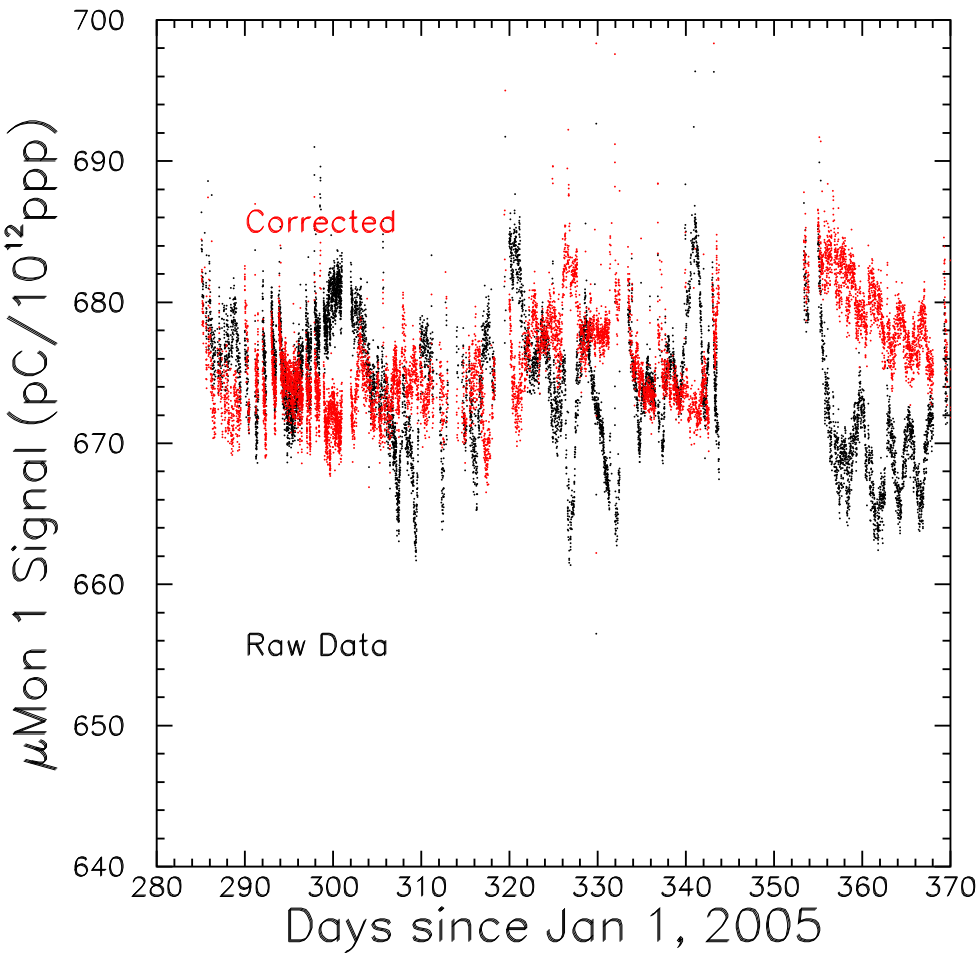

Figure 5.14: Measured total intensity in Alcove 1 over the period from October 11, 2005 to Jan 5, 2006.

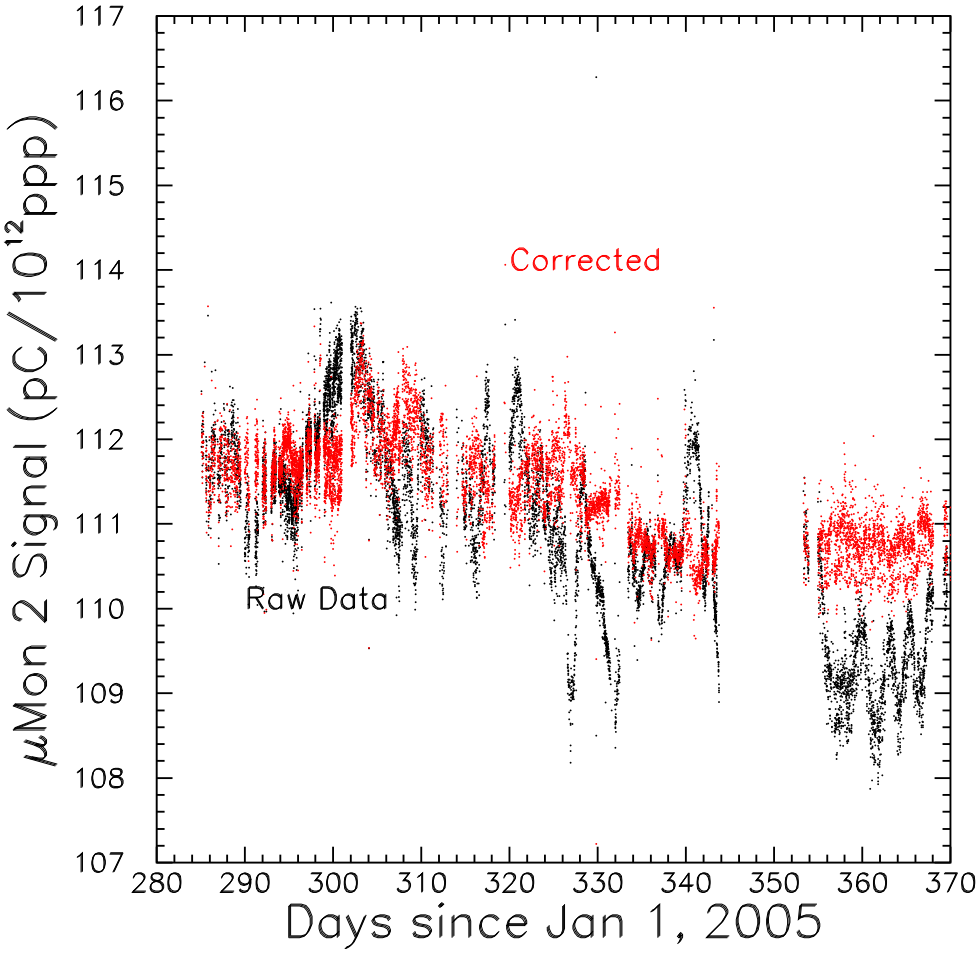

Figure 5.15: Measured total intensity in Alcove 2 over the period from October 11, 2005 to Jan 5, 2006.

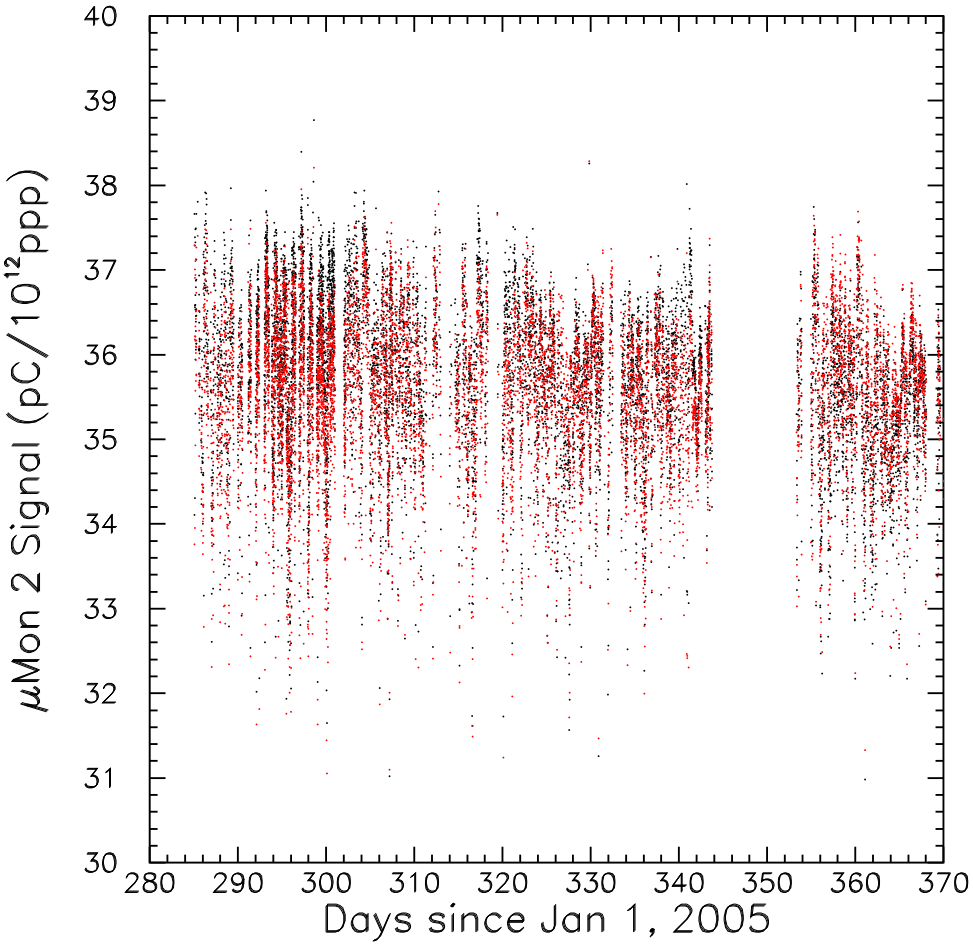

Figure 5.16: Measured total intensity in Alcove 3 over the period from October 11, 2005 to Jan 5, 2006.

hadron monitor demonstrates that the hadron beam remains stable to within 10μrads.

During the period from 120 to 150 days, beam operation included three target-horn configurations. From 120 to 132 days, the configuration was ME. From 132 to 140 days, the configuration was HE, and from 140 days onward, beam operated in the LE-10 configuration. Alcoves 1 & 2 show a pronounced vertical dependence on the horn position, which indicates that the axis of the target and horns are not colinear. Alcove 3 which sees the stiffest component of the tertiary beam is predictably least sensitive to the beam energy configuration.

Also, there are 2 periods of pronounced excursions in the measured centroid positions, around 220 days and 260 days. These periods correspond to times when the gas supply was contaminated. There is also evidence of non-uniform contamination of the monitors horizontally, despite the fact that the gas delivery is constructed symmetrically.

Overall, the measured centroid position stays well within $\pm$10cm of monitor center. A 10cm excursion in beam center corresponds to 100um angle off the target. The beam is shown to operate safely within the 1mrad design limit at all times.

5.5 Target Failure And Recovery

The target is enclosed in an evacuated vessel, with cooling lines running along its contours as described in Section 1.1.2. On March 23, 2005, during a scheduled shutdown, water was discovered in the pump oil of the target. Beam scans across the target evidenced the presence of water in the target canister.

Figure 5.21 shows a set of three target scans, one performed on 3/9/2005,

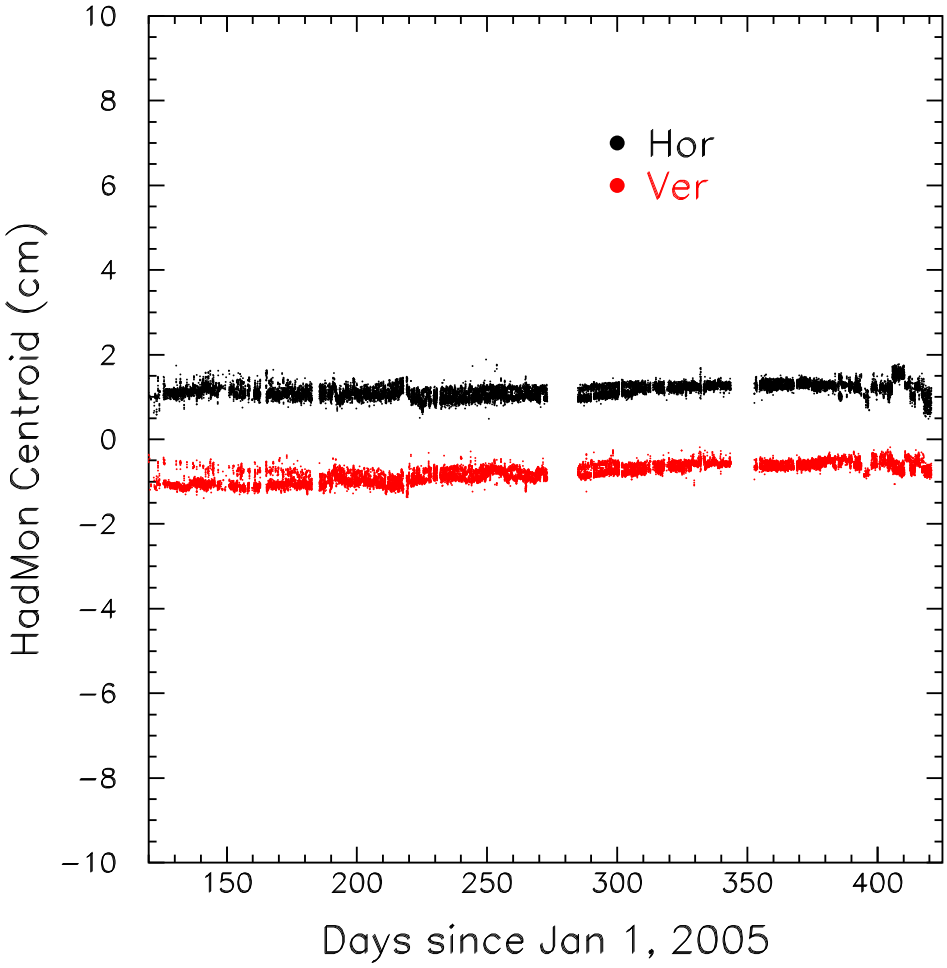

Figure 5.17: Measured Centroid position in the Hadron Monitor from July 29 to Feb 25, 2006.

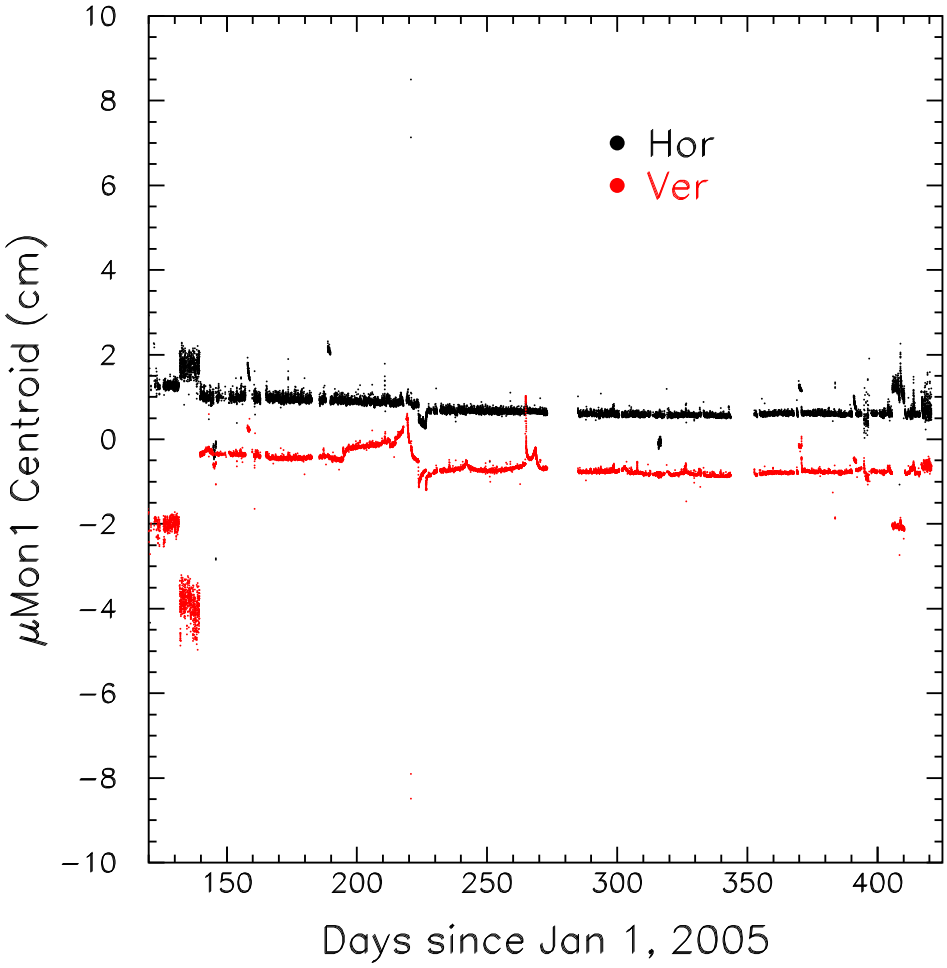

Figure 5.18: Measured Centroid position in the Alcove 1 from July 29 to Feb 25, 2006.

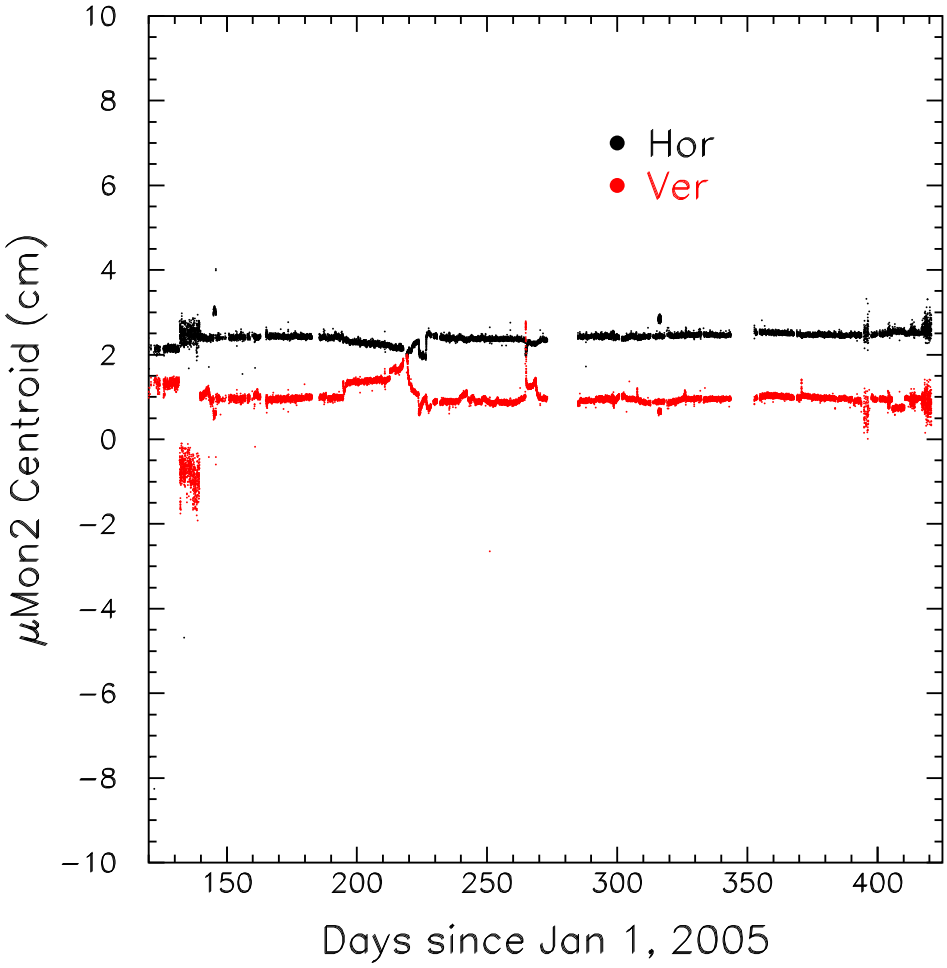

Figure 5.19: Measured Centroid position in the Alcove 2 from July 29 to Feb 25, 2006.

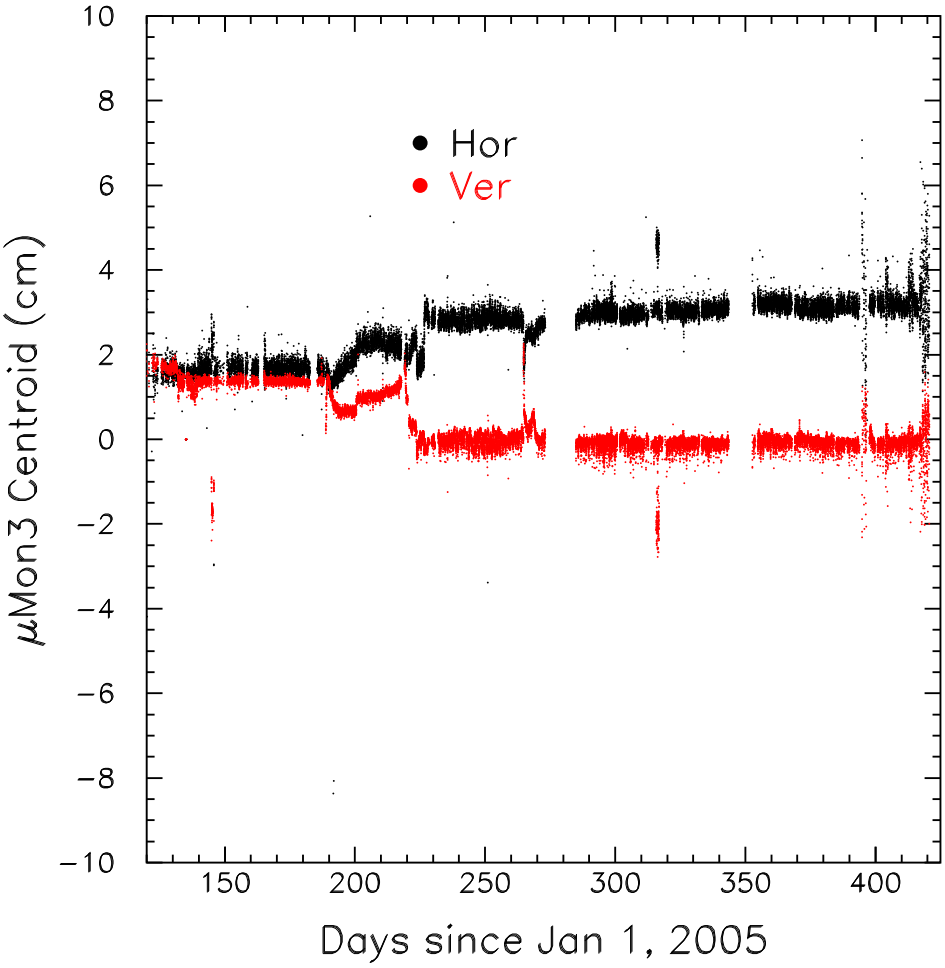

Figure 5.20: Measured Centroid position in the Alcove 3 from July 29 to Feb 25, 2006.

one immediately after the water was discovered in the pump oil on 3/23/2005, and one two days later on 3/25/05. In the earliest scan, the hadron monitor signal shows a nominally constant value of about 40nC/$10^1$2ppp as the beam is scanned across the center of the target. As the beam approaches the left and right edges of the target, the hadron monitor signal increases since more of the proton beam misses the target. The HM signal peaks as the beam moves into the gap between the target and baffle, and subsequently decreases as the beam hits the baffle.

On the 3/23 scan, the hadron monitor showed suppressed signal by a factor of two when scanned through the gap, evidencing attenuation through water. As shown in Figure 5.21, the ratio of the signal in beam-left gap to nominal is about .35. Since the HM signal is proportional to $e^{-\lambda_{int}}$, the effective $\lambda_{int-graphite}$ is given by

$$\lambda_{int-graphite} = ln\,(HM_{leak}/(PH)_{nom}) = 1.04m$$

This corresponds to a $\lambda_{int-water}$ = .87m. The signal at the center of the target did not change, indicating that the target snout was clear.

The signal was further suppressed two days later even when the beam was centered, indicating the presence of water in the target snout. The ratio of the HM signal at target center to nominal is .61. This suggests a $\lambda_{int-graphite}$ of 2.54. The graphite target is 2.05, and the surplus .49 interaction lengths corresponds to .41m of water. In the beam-left gap, a signal ratio of .2 suggests the presence of 1.34m of water. It was concluded that water had filled the target cannister.

The hadron monitor beam sigma is another measure of target integrity. Measurements of the beam width in the hadron monitor during the horizontal target scans are given in Fig 5.22. The expected spot size at the hadron

monitor is determined by the multiple scattering in the target. This gives

$$\sigma_{HadMon} = 725m \times \frac{13.6mrad}{120GeV}\sqrt{t/\chi_0}$$

where t is the length of the target seen by the beam and χ_0 is the radiation length of the target. More material leads to an adjustment in the radiation length in the calculation of the beam width in the form

$$\frac{t}{\chi_0} \rightarrow \frac{t}{\chi_0} + \frac{t'}{\chi_0'}.$$

The water measurements from the beam monitor data is summarized in Table 5.2.

Four sets of vertical target scans are shown in the Figure 5.23 and 5.24. During these scans, the beam is centered on target and then translated vertically ± 10 mm by adjusting trim magnets near the target. The scan taken on 3/9 occurred prior to the target leak. It shows a maximum signal when the beam is on target, and a suppressed signal as the beam hits the baffle beyond +5mm and -3mm. The width of the beam at the Hadron monitor is narrowest when the beam is on target. Interestingly, the beam is about 1% narrower at -2mm than at +1mm, because there are fewer reinteracted pions at the target edge. One of the target fins is rotated 90° and shifted upward vertically. Its presence marginally suppresses the signal as the beam moves vertically higher.

In the vertical scans taken after the leak, the water level can be determined from the absolute signal and the slope of the profile, as well as the change in the measured beam size. On 3/30, when the target was most filled, a pronounced notch can be seen at +3mm which indicates a water level almost filling the can and completely permeating the target snout. Also, the beam width shows a marked increase from more multiple scattering in the target.

Efforts were made to pump out the water from the target without exuming it from beneath the target shielding. The target was pressurized with the presumption that the water would push back through the leak into the water lines. Progress was made with this technique, as shown in the vertical scans taken on 4/1 and 4/3. The signal on target increased, and the notch was less defined. However, pumping after 4/1 showed little or no improvement, and it was determined that the target had to be removed. This is confirmed by the beam width measurements.

The target was exhumed from the beamline and the water was pumped out. The leak was never discovered. The target was reinserted into the beam, and normal running eventually resumed with two differences: a drain was installed in the target, and the target was backpressured with helium instead of evacuating it as before. Horizontal scans were taken once the target repairs were completed and on a regular basis since this time to ensure no water in the canister.

Monitor	% Change in Signal /Torr (Expected)	% Change in Signal /Torr (Measured)
Hadron Monitor	.13%	.05%
Alcove 1	.13%	.14%
Alcove 2	.13%	.12%

Table 5.1: Measure of the signal variations in the Hadron and Muon Monitors with pressure.

	Wed 3/9	Mon 3/28
HadMon Intentsity @ TGT CTR (pC/$10^1$2ppp)	3900	2400
Effective λ_{Int} @ TGT Ctr = -ln($\frac{PH}{PH_{3/9}}$)	2.05 →2m Graphite	2.05 + .49 →2m Graphite + .41m H_20
HadMon @ TGT Left Gap (pC/$10^1$2ppp)	20000	4200
Effective λ_int @ TGT Gap = -ln($\frac{PH}{PH_{3/9}}$)	0	1.6 → 1.34m H_20
Had(Max/Tot) @ Targ Ctr	.038	.030
Measured HadMon RMS @ TGT Ctr (mm)	212	217
Effective X_0 @ TGT Ctr	6.7	7.02 → .32X_0, 12cm H_20

Table 5.2:

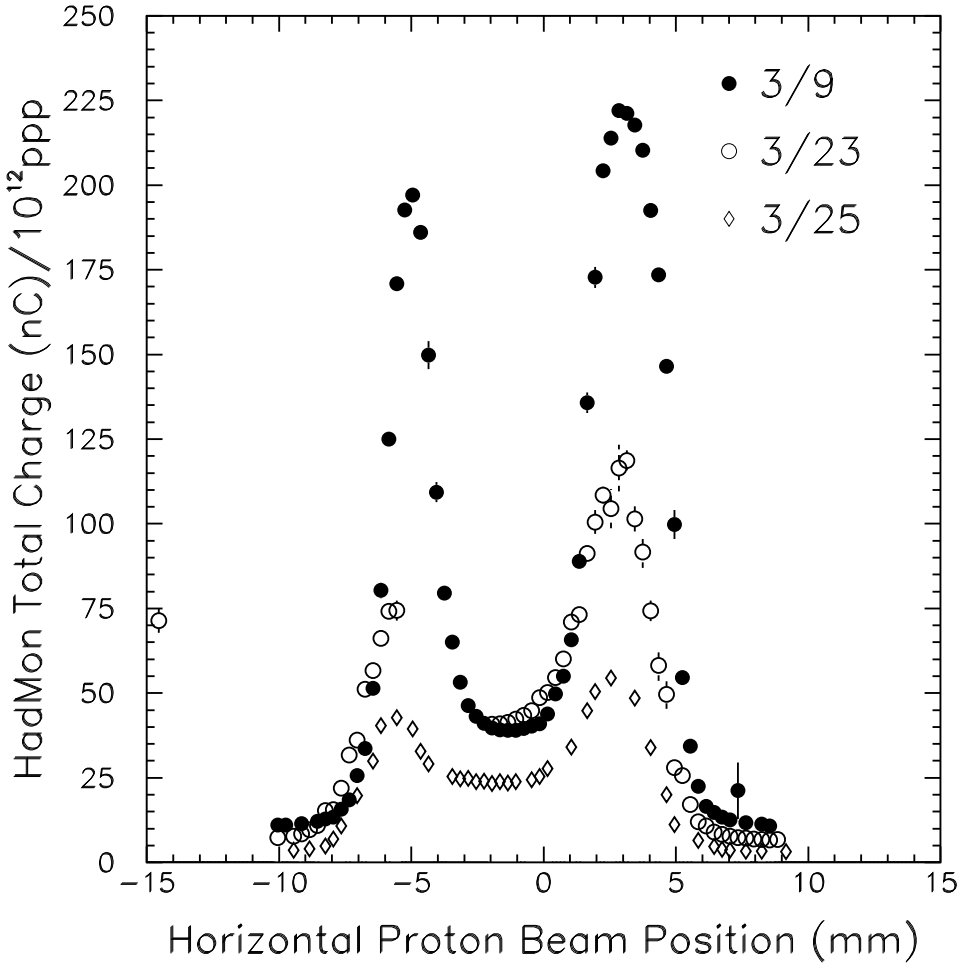

Figure 5.21: The horizontal rms as measured by the Hadron monitor as a function of horizontal beam position shows valleys corresponding to the gap between the target and baffle. The beam width is wider in the presence of water.

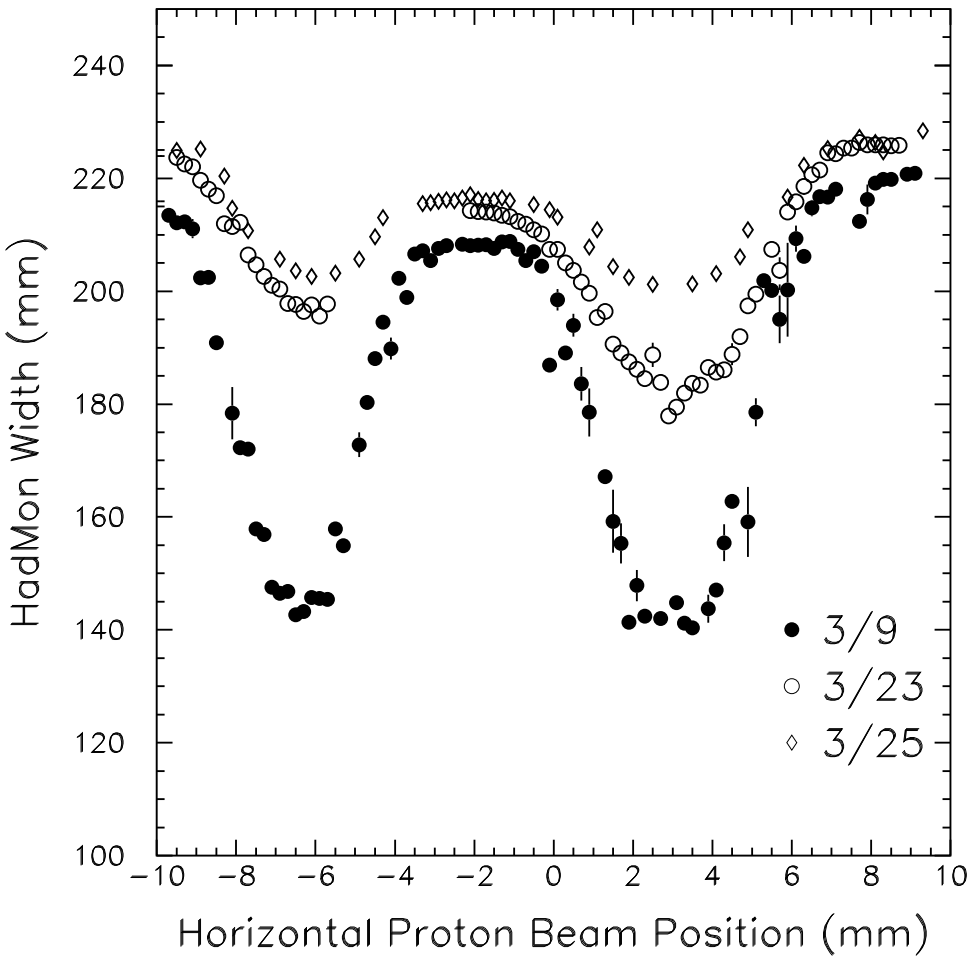

Figure 5.22: Hadron Monitor normalized intensity as a function of horizontal beam position on target.

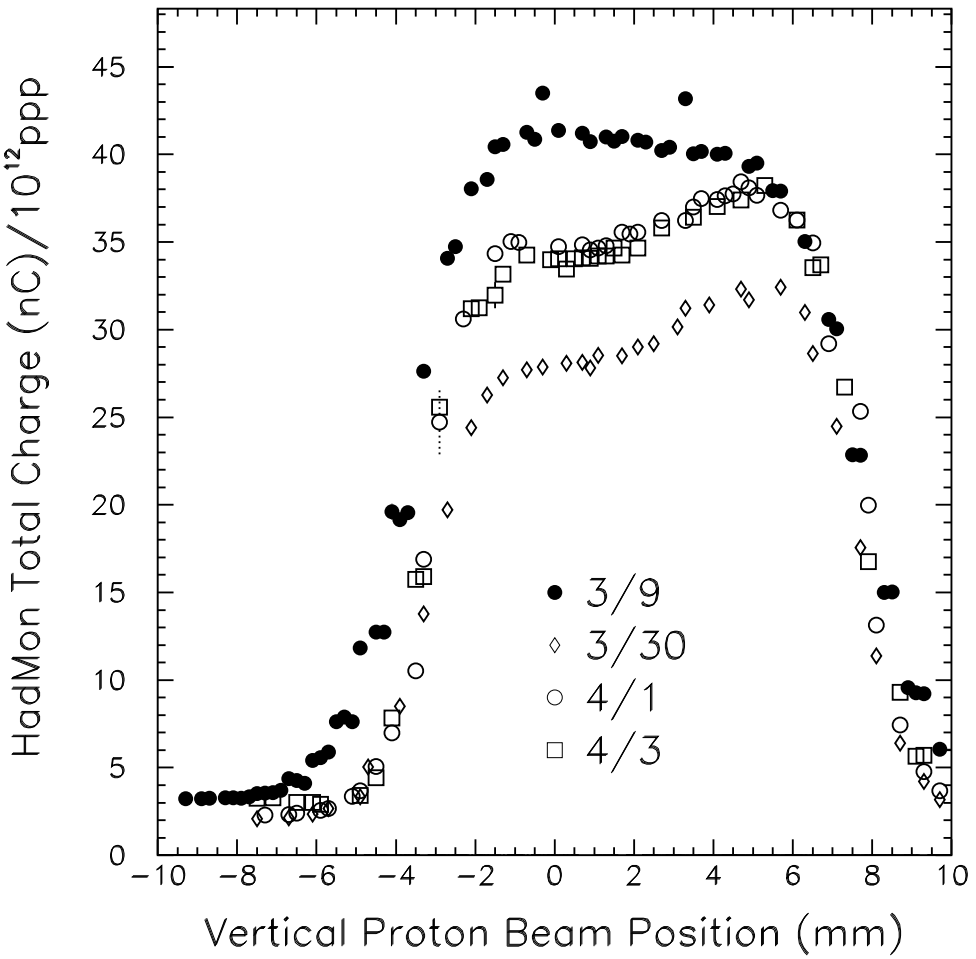

Figure 5.23: Shown are vertical scans of the target pre-leak, a few days after the leak was discovered (3/30), and after repairs were implemented (4/26). The intensity in the hadron monitor changes with the vertical position on target corresponding to the amount of water in the path of the beam.

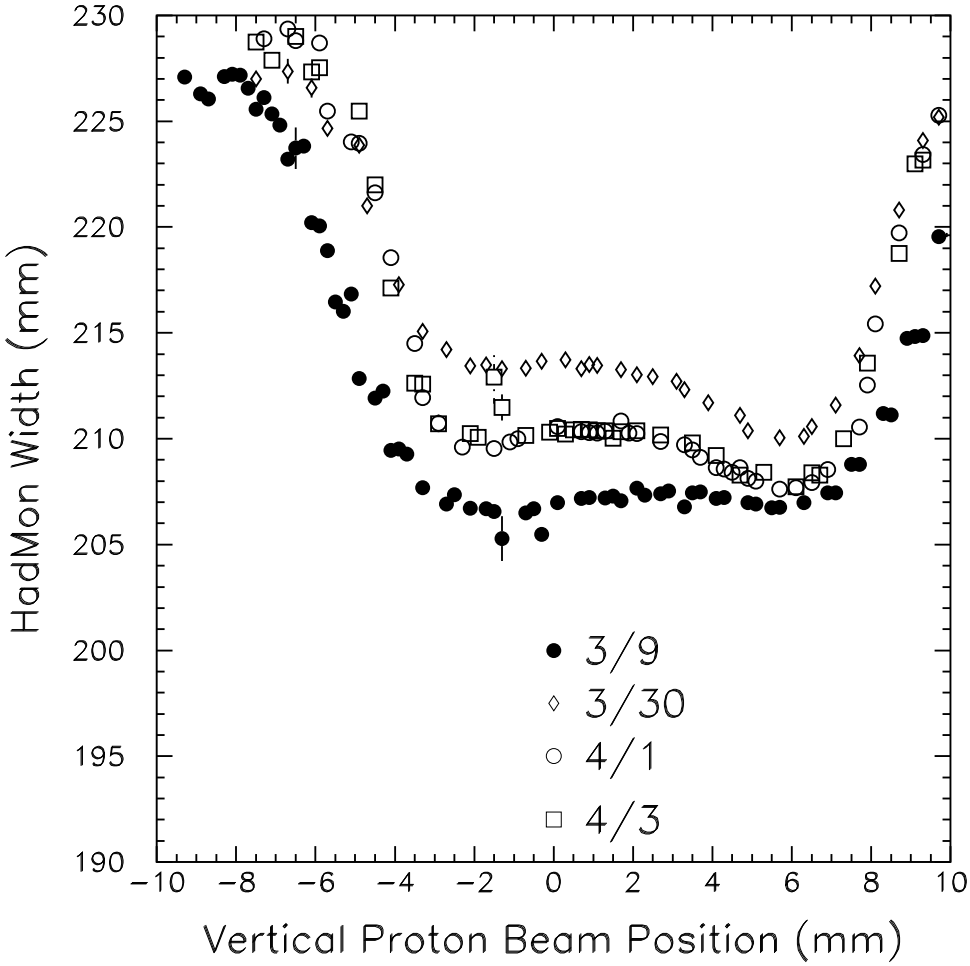

Figure 5.24: Shown is the Hadron Monitor measured RMS as a function of the vertical beam position at the target during a vertical target scan. The days pre-leak showed a symmetric profile about target center, but beam width increases in the presence of water after the leak is discovered. Efforts to pump out the water show some improvement.

Bibliography

[1] Hylen, J., *et al.*, "Conceptual design for the technical components of the neutrino beam for the main injector (NuMI)," Fermilab-TM-2018 (1997).

[2] The MINOS Collaboration, Fermilab NuMI-L-337, Oct. 1998, S. Wojcicki, spokesperson.

[3] NOvA Collaboration, Fermilab P929, `arXiv:hep-ex/0210005`, G. Feldman and M.Messier, spokespeople.

[4] MINERvA Collaboration, Fermilab proposal P938, `arXiv:hep-ex/0405002` (2004), J. Morfin and K. McFarland, spokespeople.

[5] D.G. Michael *et al*, "Observation of Disappearance of Muon Neutrinos with an Accelerator Neutrino Beam," submitted to Phys. Rev. Lett.

[6] Kostin, M., Kopp, S., Messier, M., Harris, D., Hylen, J., Para, A., "Proposal for Continuously Variable Neutrino Beam Energy for the NuMI Facility," Fermilab-TM-2353-AD(2001).

[7] P. Prieto, "NuMI BPM Electrical Offset, BPM Polarity measurement and Intensity Scaling Calculation", Fermilab Beams Document 1534, 2005.

[8] D. Indurthy, S. Kopp, M. Proga, and Z. Pavlovich, "Profile monitor SEM's for the NuMI beam at Fermilab",

[9] A. G. Abramov *et al.*, "Beam Optics and Target Conceptual Designs for the NuMI Project", *Nucl. Instrumen. Meth.* **A485** (2002) pp. 209–227.

[10] R. M. Zwaska, "Accelerator systems and instrumentation for the NuMI neutrino beam," FERMILAB-THESIS-2005-73

[11] Fermilab, *NuMI Technical Design Handbook,* 2002-4

[12] D. Harris, Downstream Hadron Monitor Requirements for the NuMI Beamline, MINOS Internal Note 785, 2001.

[13] D. Harris, "Muon Monitoring Requirements for the NuMI Beamline", MINOS Internal Note 756, 2001.

[14] E. Fuller *et al.*, "Studies of Cross Talk Between Ion Chambers", MINOS Internal Note 823, 2002.

[15] CerTek, Inc. of El Paso, TX

[16] Model 8510, Branson Ultrasonics Corporation of Danbury, CT

[17] Product # 8007, Global Diversified Products of St Petersburg, FL

[18] Citrus Degreaser, Finish Line Technologies, Inc, of BayShore, NY.

[19] D. Harris and N. Grossman, Radiation Dose Calculations for Monitoring System, MINOS Internal Note 845, 2002.

[20] Insulator Seal of Sarasota, Fl.

[21] A. Erwin *et al.*, "Support structures for the Muon Monitors", MINOS Internal Note 848, 2002.

[22] Model 332, Concoa North America of Virginia Beach, VA.

[23] 820 Series, Sierra Instruments of Monterey, CA.

[24] Model 810, MKS Instruments, Inc. of Wilmington, Massachusetts.

[25]

[26] Y. Wang, CRC Handbook of Radioactive Nuclides (Cleveland: Chemical Rubber Co), 1969.

[27] Keithley Instruments, Inc., Cleveland, OH.

[28] Mindtel, Inc.

[29] Applied Data Sciences, Inc., Dallas, TX.

[30] R. M. Zwaska *et al.*, "Beam tests of ionization chambers for the NuMI neutrino beam," IEEE Trans. Nucl. Sci. **50**, 1129 (2003) [arXiv:hep-ex/0212011].

[31] J. McDonald *et al.*, NuMI-B-803, "PIC ATF Beam Test Results," (December 2001).

[32] D. Naples *et al.*, NuMI-B-769, "Pad Ionization Chamber Design," (August 2001).

[33] K. W. Geiger and L. Van der Zwan, *Nuclear Instruments and Methods*, **131**, 315 (1975).

[34] G. F. Knoll, *Radiation Detection and Measurement*, Third Edition, John Wiley & Sons, Inc., New York (2000).

[35] M. E. Anderson and R. A. Neff, *Nuclear Instruments and Methods*, **99**, 231 (1972).

[36] S. Croft, *Nucl. Instr. Meth.*, **A281**, 103 (1989).

[37] B. Haesner *et al.*, *Phys. Rev.* **C28**, 995 (1983)

[38] F. J. Vaughn *et al.*, *Phys. Rev.* **118**, 683 (1960)

[39] J. R. Smith, *Phys. Rev.* **95**, 730 (1954)

[40] R. E. Shamu and J. G. Jenkin, *Phys. Rev.* **135**, B99 (1964)

[41] P. L. Beach *et al.*, *Phys. Rev.* **156**, 1201 (1967)

[42] C. F. Cook and T. W. Bonner, *Phys. Rev.* **94**, 651 (1954)

[43] D. C. Grahame and G. T. Seaborg, *Phys. Rev.* **53**, 795 (1938)

[44] D. D. Phillips *et al.*, *Phys. Rev.* **88**, 600 (1952)

[45] P. R. Malmberg and S. C. Snowdon, *Phys. Rev.* **128**, 351 (1962)

[46] T. W. Bonner *et al.*, *Phys. Rev.* **97**, 985 (1955)

[47] ICRU Report 49, "Stopping Powers and Ranges for Protons and Alpha Particles," International Commission on Radiation Units and Measurements (1993)

[48] National Institutes on Standards and Technology, "Stopping Powers of Electrons, Protons, and Helium Nuclei," 'www.nist.gov/srd/physics.htm'.

[49] D. H. Wilkinson, *Ionization Chambers and Counters*, Cambridge University Press, Cambridge (1950).

[50] J. H. Coon and R. A. Nobles, *Rev. Sci. Instr.* **18**, 44 (1947).

[51] ICRU Report 31 "Average Energy Required to Produce An Ion Pair" (International Commission on Radiation Units and Measurements, 1 May, 1979).

[52] K. Hagiwara *et al*, *Phys. Rev.* **D66**, 010001 (2002)

[53] I. Christophorou, "Atomic and Radiation Physics," (New York: John Wiley & Sons) 1973.

[54] V. McLane, C. Dunford, and P.F. Rose, eds., *Neutron Cross Sections, Vol.2: Neutron Cross Section Curves*, National Nuclear Data Center, (Boston: Academic Press, Inc.) 1988.

[55] R. D. Evans, *The Atomic Nucleus*, (New York: McGraw-Hill) 1955.

[56] H. Schraube and H. Bichsel, *Radiation Protection Dosimetry* **13**, 373 (1985).

[57] J. Belz *et al.*, *Nucl. Instr. Meth.* **A428**, 239 (1999); S. D. Worm, PhD Thesis, University of Texas, Austin (1995).

[58] ICRU Report 37, "Stopping Powers and Ranges for Electrons and Positrons," International Commission on Radiation Units and Measurements, 1989.

[59] *GEANT Detector Description and Simulation Tool*, CERN Program Library, W5013 (1994).

Vita

Dharmaraj Indurthy was born in Lawrence, Kansas on March 14, 1980 to the parents of Rathnam and Nirmala Indurthy. He grew up primarily in Lake Charles, Louisiana and graduated from A. M. Barbe High School in 1998. He earned a Bachelor of Science in Physics from Texas A&M University in the Spring of 2002, and began working for Professor Sacha Kopp immediately at the University of Texas at Austin. As a graduate student, he earned travel grants to the United States Particle Accelerator School in the summer of 2003, the winter of 2004, and the summer of 2005, and to the 2005 Particle Accelerator Conference. He was also awarded 1st place in the Fermilab Graduate Students Association poster contest at the New Perspectives Conference in June of 2005.

Permanent Address: 612 E. Lagrange St.
Lake Charles, LA 70607

This thesis was typeset with LaTeX 2_ε[1] by the author.

[1] LaTeX 2_ε is an extension of LaTeX. LaTeX is a collection of macros for TeX. TeX is a trademark of the American Mathematical Society. The macros used in formatting this thesis were written by Dinesh Das, Department of Computer Sciences, The University of Texas at Austin, and extended by Bert Kay and James A. Bednar.